Magnetic Cleanliness, Sensing, and Calibration for CubeSats

by

Nicholas Belsten

B.E., Vanderbilt University (2019)

Submitted to the Department of Aeronautics and Astronautics
in partial fulfillment of the requirements for the degree of

Master of Science in Aeronautics and Astronautics

at the

MASSACHUSETTS INSTITUTE OF TECHNOLOGY

February 2022

Author .....
Department of Aeronautics and Astronautics
Jan 20, 2022

Certified by .....
Kerri Cahoy
Associate Professor
Thesis Supervisor

Accepted by .....
Jonathan P. How
R.C. Maclaurin Professor of Aeronautics and Astronautics
Chair, Graduate Program Committee

This page is intentionally left blank.

Magnetic Cleanliness, Sensing, and Calibration for CubeSats

by

Nicholas Belsten

Submitted to the Department of Aeronautics and Astronautics
on Jan 20, 2022, in partial fulfillment of the
requirements for the degree of
Master of Science in Aeronautics and Astronautics

Abstract

Magnetometers are widely used on satellites for both attitude sensing and scientific observations. Spaceborne magnetometers have enabled the creation of accurate maps of Earth's magnetic fields. However, these models have limited spatial and temporal resolution, and therefore are much less accurate in locations with fast or localized magnetic perturbations. Such perturbations can be particularly problematic near Earth's poles where field aligned currents come close to the surface of the Earth and are concentrated near satellites in LEO. Science missions which need to know the local magnetic field in the polar regions need to bring their own high-fidelity magnetic sensors.

The AERO-VISTA mission comprises a pair of 6U CubeSats which will determine the propagation modes and directions of high frequency (400 kHz–5 MHz) waves in Earth's ionosphere in the presence of Earth's aurorae. This mission science requires accurate in-situ magnetic sensing of auroral currents for RF measurement context.

This thesis details the design, integration, and testing of the magnetic sensors in the AERO-VISTA Auxiliary Sensor Package (ASP). We discuss the estimation of spacecraft self-interference and implement an informal magnetic interference control process. We present some simple ground testing strategies for magnetic screening of components and measurement of spacecraft self-interference. We evaluate the performance and non-ideal effects of our selected anistropic magnetoresistive (AMR) 3-axis magnetometer. We create a measurement equation, which together with regression techniques, allows for calibration to better than 100 nT repeatability despite non-ideal effects, meeting AERO-VISTA's requirements. This calibration strategy is extended to include current path and material interference effects. We describe the detailed design of the magnetic sensing system, including the electronics, mechanical design, and software of the ASP. Without self-interference effects, this design has a noise floor better than 10 nTrms.

Thesis Supervisor: Kerri Cahoy
Title: Associate Professor

This page is intentionally left blank.

Acknowledgments

I first thank my advisor Dr. Kerri Cahoy for giving me the opportunity to work on the AERO-VISTA mission, guiding me in my time at MIT, and tirelessly providing feedback on this thesis.

I'd like to thank all my friends and family who kept me going even under less than ideal working conditions. My partner, Jiayu Liang, has supported me in all ways, even taking on the duties of office mate while working from home. I'd like to thank my parents for always being a call away and knowing when to lend an ear and when to tell me to get back to work.

I thank the entire AERO-VISTA team for working with me on this amazing project and for providing more learning opportunities than I can even realize. I thank my AERO-VISTA ASP teammates Cadence Payne and Kristen Ammons both for their technical perspectives and for helping me navigate graduate study. My mentors on the AERO-VISTA team have guided this work and my professional development more generally. Frank Lind, Becky Masterson, Mary Knapp, and Alvar Saenz-Otero have all practically served as secondary thesis advisors.

I'd like to thank the Paleomagnetism Laboratory, particularly Ben Weiss and Jay Shah, for their input and for providing access to their magnetic measurement facilities. This project was supported by NASA's Heliophysics Technology and Instrument Development for Science (H-TIDeS).

This page is intentionally left blank.

Contents

List of Figures

This page is intentionally left blank.

List of Tables

Acronyms

ACE Advanced Composition Explorer (spacecraft).

ADC Analog to Digital Converter.

ADCS Attitude Determination and Control System.

AERO Auroral Emissions Radio Observer.

AMR Anisotropic Magnetoresistive Magnetometer.

ASP Auxiliary Sensor Package.

ASPIT Auxiliary Sensor Package Interface Tester.

CAN Controller Area Network.

CGS Centimeter-gram-second (system of units).

CMRR Common Mode Rejection Ratio.

DAC Digital to Analog Converter.

DC Direct Current.

EAPS Earth, Atmospheric, and Planetary Sciences (MIT Department).

ECEF Earth-Centered, Earth-Fixed (coordinate system).

ECI Earth-Centered, Inertial (coordinate system).

EM Engineering Model.

EMI ElectroMagnetic Interference.

EPS Electrical Power System.

FF Radio Frequency.

FM Flight Model.

GPIO General Purpose Input/Output (of Raspberry Pi).

GPS Global Positioning System.

GSE Ground Support Equipment.

HF High Frequency.

IGRF International Geomagnetic Reference Field.

LDO Low-Dropout (voltage regulator).

LEO Low Earth Orbit.

LNA Low Noise Amplifier.

LSB Least Significant Bit.

LVDS Low Voltage Differential Signal.

MCRB Magnetic Control Review Board.

MDM Multi-Dipole Model.

MIT Massachusetts Institute of Technology.

P2P Peak-to-Peak.

PCB Printed Circuit Board.

ppm parts per million.

PSRR Power Supply Rejection Ratio.

rms root-mean-square.

SI International System of Units.

SMPS Switch Mode Power Supply.

SPI Serial Peripheral Interface.

SPS Samples per Second.

SSL Space Systems Lab (MIT lab).

STARLab Space Telecommunications, Astronomy and Radiation Laboratory (MIT lab).

VISTA Vector Interferometry Space Technology using AERO.

VLBI Very Long Baseline Interferometry.

VS Vector Sensor.

WMM World Magnetic Map.

This page is intentionally left blank.

Chapter 1

Introduction

This thesis covers the magnetic sensing instrument design for the AERO-VISTA CubeSat mission. While some design features are a product of unique design constraints particular to the AERO-VISTA mission (introduced in Section 1.1.3), most lessons learned are broadly applicable to any CubeSat magnetic sensing effort. The instrument we have developed is capable of measurement precision and repeatability to between 20 nT and 100 nT depending on instrument settings and self-interference.

1.1 Motivation

The magnetic system for AERO-VISTA has a unique confluence of requirements. On one hand, we want to design a magnetic sensing system to meet our scientific goals (see Section 4.2). On the other hand, we need to develop the instrument (and integrate it into the satellite) on an extremely limited budget and timeline. In this section we introduce the mission science goals and programmatic constraints.

1.1.1 CubeSats

CubeSats are small satellites which follow a set of common specifications [7] so that each satellite can use a common set of technology building blocks and launch infrastructure. The CubeSat specification aims to "reduce cost and development time, increase accessibility to space, and sustain frequent launches" [7]. CubeSats' small

size keeps launch costs down, and a risk tolerant posture assumed by most CubeSat developers reduces development cost. CubeSats initially were simple, and often developed as an educational tool, but there has been a trend towards larger, more capable, and more reliable CubeSats. CubeSats are specified by "unit" (U), where one U is a cube with 10 cm on a side weighing not more than 1.33 kg. While the original[1] specifications allow for satellites up to 3U, larger nanosatellites are now in use. CubeSats are now not only used for education, but also by universities or government labs for scientific research, or by private companies for commercial service. Cal Poly released an official 6U CubeSat specification in 2018, and the new CDS Rev 14 will contain specifications for satellites up to 12 U [7].

The 6U AERO-VISTA satellites will perform completely new science observations, and have some complexity (hundreds of MB per second of data are generated during acquisition, and there are several meter-scale deployables). Yet, CubeSat missions like AERO-VISTA have limited time for development and need to stay within a modest budget. Following the long tradition of CubeSats as an educational tool, the AERO-VISTA Auxiliary Sensor Package (ASP) described in this thesis (see Chapter 8) is primarily developed by students. Initial design of the ASP started in 2019.

1.1.2 Satellite Magnetic Sensing

Magnetic sensing can be used on satellites for orientation determination and/or for scientific observations. In Low Earth Orbit (LEO), the magnetic field strength is about 40 uT and the vector direction varies with latitude in a known pattern. More precise estimates of the local magnetic field can be obtained with a spherical harmonic expansion of the Earth's magnetic field. These expansions can be queried at the local position to find the local magnetic field to about 150 nT accuracy [8]. Such models include the World Magnetic Map (WMM) [9] and the International Geomagnetic Reference Field (IGRF) [10].[2] If a satellite knows its own location to sufficient

[1] As of writing, the most recent released version is Rev 13, last updated in 2014.

[2] The WMM is jointly maintained by the United States' National Geospatial-Intelligence Agency (NGA) and the United Kingdom's Defence Geographic Centre (DGC). The IGRF is maintained by the International Association of Geomagnetism and Aeronomy (IAGA).

accuracy and can query a stored magnetic map, it can compare the measured magnetic field in the spacecraft's body frame to the expected magnetic field in a global reference frame to determine the spacecraft attitude. Since the measurement is of a single vector, the measurement is degenerate in a rotational axis around the magnetic field direction, so the magnetometer measurement is often used with other sensors including gyroscopes, Earth horizon sensors, or star trackers.

In addition to providing orientation information, the Earth's magnetic field can provide a source of torque through the use of satellite magnetorquers. Some recent research has focused on magnetic only control, where the satellite holds a 3-space vector orientation without the use of reaction wheels or control thrusters, instead using only magnetorquers and the change in magnetic field orientation over an orbit to solve the along-axis magnetic field degeneracy [11, 12]. The performance of these systems will depend on the ability to achieve an accurate and non-polluted magnetic measurement.

Magnetometers can also be used for scientific observations of solar system bodies and space weather events. Satellite-borne magnetometers provide constraints on planetary geology by mapping the global or crustal magnetic fields of solar system bodies. This technique has been used in the observation of every planet in the solar system [13–20], the Earth's moon [21], as well as multiple asteroids [22, 23]. In addition to measuring the magnetic fields of objects in the solar system, magnetic field observations are used to learn about the space plasma environment, such as the connection between interplanetary magnetic fields and solar coronal activity [24].

The term *space weather* refers to the magnetic and electromagnetic activity of the Sun as it relates to operation in the space environment [25]. The Earth's magnetic field partially shields the Earth from solar wind, but changes in solar magnetic activity can change the size and effectiveness of this shield. As the solar wind changes the shape of the Earth's magnetosphere, charged particles from the Sun can be trapped along Earth's magnetic field lines [26]. As these charged particles follow the Earth's magnetic lines they can create bulk current flow which comes near the surface of the Earth at the magnetic poles. This bulk current creates measurable magnetic pertur-

bations on the ground and can negatively affect satellite operations [25]. Collisions of these charged particles with Earth's upper atmosphere creates visible aurorae. Additionally, the motion of these particles around the Earth's magnetic fields produces radio emission in the range of 100s of kiloHertz, a phenomenon known as Aurora Kilometric Radiation (AKR) [27]. This emission is a major source of HF emission in the solar system and total power output from the Earth can exceed 1×10^9 W [28]. The observation of these radio emissions is a primary mission objective for AERO-VISTA.

1.1.3 The AERO-VISTA Missions

AERO and VISTA (collectively AERO-VISTA) are a pair of 6U CubeSats. The two identical spacecraft will work together toward the same mission goals, but the entire mission can be broken into two parts, the AERO part and the VISTA part. AERO stands for Auroral Emissions Radio Observer, and defines a mission using a six-element vector sensor to measure radio emission from the Earth's aurora in LF through HF bands (approximately 100 kHz to 5 MHz). These observations will provide new scientific data on heliospheric, planetary and astrophysical plasmas [29]. A vector sensor is an electromagnetic instrument with three *electric* field antennas (e.g. dipole or monopole) and three *magnetic* field antennas (e.g. loop) co-located to completely sample the electromagnetic vector. This is advantageous for low frequency observations as it is impractical to build an electrically large antenna at such low frequencies. An antenna with directional discrimination ability would have to be at least several wavelengths in size, which could be dozens of kilometers wide at frequencies as low as 100 kHz. The vector sensor can measure direction of propagation and polarization information while still being electrically small. However, the direction-finding ability of a single vector sensor can be degraded in the presence of multiple strong interfering signals [30].

The VISTA (Vector Interferometry Space Technology using AERO) mission will demonstrate one way to achieve improved imaging at the same wavelengths as the AERO mission. The VISTA spacecraft will measure the radio environment at the same time as the AERO spacecraft, but with a physical separation of a few to several

kilometers between them [31]. Each spacecraft also carries a small chip scale atomic clock for precise time-stamping of the RF data [32]. This allows the two satellites to synthesize a large antenna using techniques analogous to ground-based very large baseline interferometry (VLBI) [33]. While either satellite alone can perform HF direction finding measurements to fulfill the scientific objectives of the AERO mission, AERO and VISTA will need to simultaneously observe and synchronize their measurements to demonstrate interferometry and fulfill the technology demonstration VISTA mission.

1.2 Thesis Structure

Chapters 2 and 3 describe the source of magnetic interference and how this is mitigated on large missions. Chapter 4 describes how we know our magnetometer will be accurate enough for our mission as long as we use the calibration method of Chapter 5. Chapter 6 describes how we screen components for magnetic interference. Chapters 7 and 8 describe the design of the magnetic sensing instrument and how we implemented it in a stand-alone payload. Chapter 9 summarizes our findings and identifies future work. Each chapter is introduced in more detail below.

In **Chapter 2** we review the relevant theory of magnetic field generation and discuss how the magnetic interference from an object or subsystem can be estimated. This effort focuses on quick estimates and simplifying approximations to triage each potential source of interference based on whether the object is (i) definitely *not* a concern, (ii) of possible concern so more careful measurement is needed, or (iii) definitely a source of significant interference.

Chapter 3 discusses how magnetic cleanliness and accurate magnetic sensing has been conducted on a range of more expensive magnetic sensing missions. We end Chapter 3 by identifying which lessons can be learned from these missions even if we do not have the time and budget to follow their exact methodologies.

In **Chapter 4** we compare the expected performance of a magnetometer to magnetic sensing requirements. We start the chapter with an overview of the requirements flow down for AERO-VISTA magnetic sensing and deconfuse common performance metrics found in magnetometer datasheets and requirements. We compare the datasheet for our chosen magnetometer (the HMC1053) to AERO-VISTA measurement requirements and describe the techniques we've used for comparing different parameterizations of magnetic performance. We then measure non-ideal effects which were described in the magnetometer datasheet (such as as hysteresis effects, noise, temperature coefficients, and static offsets). From these measurements, we identify which parameters are significant as compared to our measurement requirement and we describe and demonstrate how each of these effects can be calibrated out of our measurement if measurements can be compared to a known-good reference.

Chapter 5 describes how each non-ideal effect identified in Chapter 4 can be combined into a single measurement equation with 27 unknown parameters. We use this single equation with the data collected in Chapter 4 to evaluate the performance of our magnetometer implementation with this calibration method applied. We show calibration into the noise floor in our measurement environment and demonstrate repeatability better than our 100 nT requirement. We then show that without modification, this measurement equation will also calibrate out interference from an arbitrary number of magnetic objects in the vicinity of the magnetometer as long as those objects are exclusively magnetically hard or magnetically soft.

Chapter 6 describes how we can measure objects quickly without expensive magnetometers for magnetic screening. We describe a method to estimate an object's dipole moment and magnetic hardness with only a smart-phone magnetometer and small magnet for test equipment. These procedures should be useful for any CubeSat mission looking to quickly and inexpensively perform magnetic testing.

Chapter 7 documents the design of the magnetometer instrument for AERO-VISTA. This design implements magnetic sensing with Honeywell's HMC1053 AMR magnetic sensor. The chapter includes a detailed noise estimation and a complete error budget of a proposed analog amplification system. This discussion and analysis covers all steps in the processing chain up to digitization by the analog-to-digital converter. We end this chapter with actual magnetic noise measurements with our engineering model.

Chapter 8 describes how we have implemented the magnetometer design from Chapter 7 in a standalone payload called the Auxiliary Sensor Package (ASP). This focuses on the magnetometers and the electrical design as these are most relevant to the rest of the thesis, but we also briefly discuss the imaging system, payload mechanical design, and payload software.

The Appendices contain details that are not critical to the rest of the thesis, but we do use some of their results. Where appropriate, the reader is referred to the appendices for a more detailed discussion, additional test data, or design details.

This page is intentionally left blank.

Chapter 2

Estimating Magnetic Interference

On all spacecraft, it is difficult to measure the outside magnetic field with great accuracy because the spacecraft itself generates a magnetic field and pollutes its magnetic environment. This effect depends on the spacecraft subsystems and the size of the spacecraft. Generally, small satellites such as a CubeSats are going to have magnetometers close enough to other subsystems such that the magnetometers will be measuring a combination of the both the ambient magnetic field and spacecraft-generated polluting field.[1]

The self-interfering magnetic field can be static or time-varying; it could remain fixed with the spacecraft coordinate system, or it can rotate as the spacecraft moves through its orbit. Some effects can drift with aging and temperature; others may change with orientation or spacecraft operating mode.[2] In this work, mitigation of all these effects consists of two parts: (i) minimize the interfering field where possible, and (ii) apply simplifying assumptions to create a tractable model of the local magnetic environment which can be calibrated.

Accurate magnetic measurement on a resource constrained small satellite mission is easier when the magnetic system designer can quickly provide input on design trades for the other spacecraft systems. One motivating example encountered during

[1] Though there have been CubeSat missions with long booms to distance the magnetometer from the rest of the CubeSat, such as CINEMA [34].

[2] A notable example is the solar panel magnetic field which depends on both illumination from the sun and spacecraft charge state. This is discussed more in Section 2.5.

the design of AERO-VISTA is the choice of materials in connector selection. One connector option is an off-the-shelf component which costs only tens of dollars and can be acquired within a week; however, it comes with no guarantees of magnetic cleanliness. Alternatively we can choose an explicitly non-magnetic connector for a cost of hundreds of dollars and a several week lead-time. The engineers in charge of the particular subsystem and the integration schedule would prefer the off-the-shelf part, and it is important that the magnetic system designer be able to identify where true magnetic cleanliness is required and where a "good-enough" strategy can be employed to preserve project budget and timeline.

To provide rapid approximate insight into what is or is not a problem for a given magnetic measurement system, this chapter will briefly review relevant concepts of magnetic field generation, with a particular emphasis on quickly calculating an estimated magnetic field from simplifying assumptions about materials and geometries. We will analyze some mathematical models for representing complex combinations of magnetic sources and geometry with a few parameters, and will end with a treatment of the most common magnetic polluters in spacecraft systems.

2.1 Magnetic Characterization

We summarize key properties in magnetic analysis used in this work and their units in Table 2.1.

Table 2.1: Properties and units for magnetic characterization [6].

Property	Symbol	SI Unit	CGS Unit	Explanation
Flux Density	**B**	A/m	Oe	Magnetic flux density is defined by its effect on moving charges or currents
Magnetizing Field	**H**	T	G	Magnetic field neglects any contributions from the material in which the measurement is made
Permeability	µ	H/m	unitless[1]	Degree to which a magnetizing field creates a magnetic flux density in a given medium
Susceptibility	χ[2]	unitless	unitless[3]	Measure of material permeability with respect to the permeability of free-space

[1] Prior to the adoption of the SI system, there were several standard ways to define electromagnetic units on top of the CGS system (two common options were Gaussian units and MKSA, see for reference the Appendix of Jackson's Electrodynamics [35]).
[2] There are several types of susceptibility. We usually deal with volume susceptibility χ_v, but this unitless value could be converted into other measures like mass susceptibility χ_{mass} or molar susceptibility χ_{mol} using material density and molar mass.
[3] The cgs-emu system of units susceptibility would be multiplied by 4π to find the SI susceptibility due to the different definitions of permeability.

Note that both the B and H fields are sometimes called simply "magnetic field" depending on the context. In cases where the measurement takes place in a vacuum, the values are interchangeable via the permeability of free space μ_0 and the usage is indicated by the units.

2.1.1 Dipoles

The basic unit of magnetism is a dipole, and the magnetic field of more complicated geometries can often be well-approximated as a dipole. The field generated from a dipole can be calculated with vectors as in Eq. (2.1) [35]:

$$\vec{B} = \frac{\mu_0}{4\pi}\left[\frac{3\hat{r}(\vec{m}\cdot\hat{r}) - \vec{m}}{r^3}\right]. \tag{2.1}$$

When we are not concerned with direction, we can simplify the numerator in the brackets of Eq. (2.1) to write an inequality of scalars:

$$\frac{\mu_0 m}{4\pi r^3} \leq B \leq \frac{\mu_0 m}{2\pi r^3}. \tag{2.2}$$

When we remove the information on the orientation between the distance vector and magnetic moment vector, we can only know the magnitude of the magnetic field to within a factor of two. In this chapter, we are dealing with quick estimates and upper bounds, so taking the conservative estimate will suffice:

$$B \approx \frac{\mu_0 m}{2\pi r^3}. \tag{2.3}$$

2.2 Fields from Currents

Moving charges create magnetic fields. All spacecraft systems which use electric power, and therefore cause currents to move, will produce an interfering effect on local magnetic measurements. The relationship between magnetic field and current path is simply represented with Ampere's Law ([36] Eq. 29.20).[3]

$$\int \vec{B} \cdot d\vec{l} = \mu_0 I \tag{2.4}$$

The integral of the magnetic field along a closed path is equal to the product of the permeability times the current passing through the loop. While this equation always holds true, we are not usually interested in the integrated magnetic field, but rather the magnetic field at a point. Ampere's law is still useful for quick derivations if geometric symmetry allows us to relate the integrated magnetic field to the magnetic field at a point. The more brute-force method of calculating the magnetic field caused by any given current path is given by the Biot-Savart law ([36] Eq. 28.7).

[3]Many references use bold to represent three-space vectors like the magnetic field. We will use the bold notation for matrices in later chapters so we use over-arrows to represent vectors such as $\vec{B}$.

$$B(r) = \frac{\mu_0}{4\pi} \int_C \frac{I d\vec{l} \times \hat{r'}}{|\vec{r'}|^2} \tag{2.5}$$

For any given contour path C made up of differential line segments dl, we can calculate the magnetic field at a point r, by using the displacement vector r' and the Biot-Savart law.

If we could exactly define the total 'dl's and associated currents in a spacecraft, we could deterministically calculate the total magnetic field at the measurement point caused by spacecraft current paths. Unfortunately, this would require knowing the exact route path of every wire between subsystems, the exact geometry and paths of currents inside subsystems such as inside PCBs and solar panels, and exact knowledge of how all these current paths turn on and off as the spacecraft conducts its various functions. All this information is effectively unknowable without a herculean effort of digital modeling.[4]

Instead of using the Biot-Savart law to estimate all spacecraft fields with a giant digital model, we will use the law to calculate characteristic magnetic fields from some simple geometries which are frequently found inside spacecraft. See Appendix B for details on simulation of complex geometries for the plots generated in this section.

2.2.1 Infinite Line Current Approximation for Finite Line

All lines look infinite at close range, so the simple infinite line current is a useful approximation for many real spacecraft systems. The magnetic field from the infinite line current can be calculated using either an infinite integral of the Biot-Savart law, or Ampere's law together with the symmetry of an infinite cylinder [37].[5]

$$B_{\infty-line} = \frac{\mu_0 I}{2\pi R} \tag{2.6}$$

[4]Efforts like this are used in a limited capacity in large expensive missions, such as discussed in Chapter 3.

[5]These equations deal with the magnitude of the estimated field as this is the value we are frequently concerned with in interference estimation. In most cases, the direction of the magnetic field can be recovered by application of the right hand rule and simple geometric arguments. In all other cases, the Biot-Savart integral should be solved formally.

Where R is the distance from the measurement point to the infinite line current. To give an idea to what extent the infinite approximation may hold true, we can numerically calculate the magnetic field about a line segment of length 2R and divide by the field calculated if the wire were infinite to create the error topograph in Figure 2-1. In this plot, and others in this section, all distances are normalized to the size of the source in question. The field computed with the approximation is compared to the field in the exact case so the topograph values are also unitless.

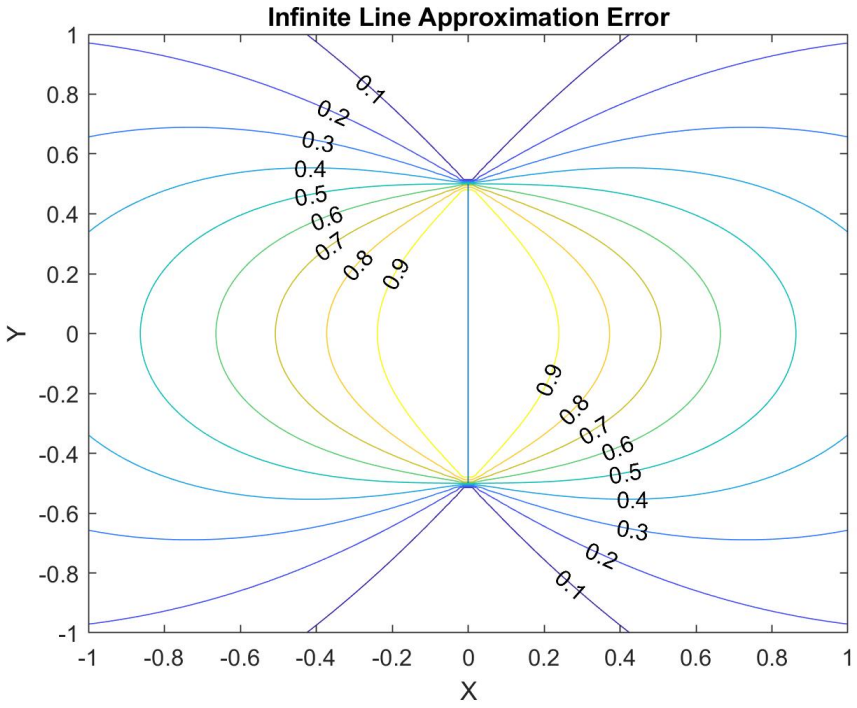

Figure 2-1: Error contours for using the infinite line approximation for a finite line source. Length units are normalized to line length. This approximation is good at small separation.

The infinite line approximation used in the proximity of a finite line will always overestimate the magnitude of the interfering field, indicating that an infinite line approximation can be used as a bounding assumption. Very near the short segment of current, the infinite line approximation is accurate to better than 10%. The approximation is particularly poor near the ends of the short segment. At a distance of about 0.8 along the bisecting axis, the error is about a factor of 2.

2.2.2 Dipole Approximation for Finite Line

Short segments of current look like simple dipoles at large distances, so a dipole approximation is useful for estimating the current contribution of high current sources at larger distances. A simple but accurate method to approximate the magnetic field from a small line current at large distances is to treat the line current as an equivalent dipole located at the geometrical center of the line current. The magnetic field in this approximation is given in Eq. (2.7) [37] and the error of this approximation is given in Figure 2-2.

$$B_{dipole-approx} = \frac{\mu_0 I}{2\pi} \frac{l}{r^2} \tag{2.7}$$

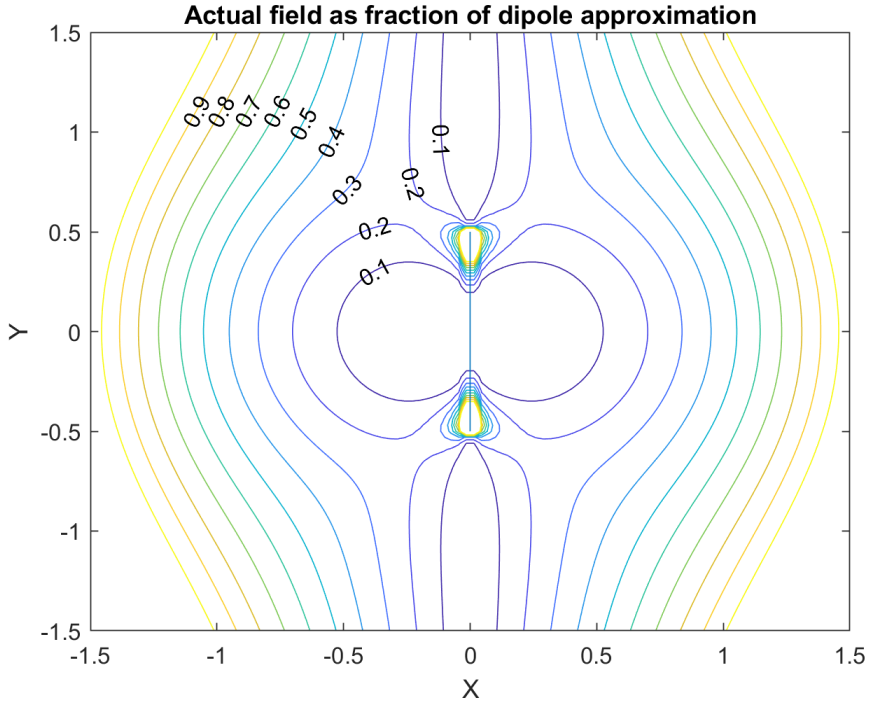

Figure 2-2: Error contours for using the dipole approximation with a finite line source. This approximation is good at larger separations.

2.2.3 Current Loop

In real spacecraft systems, the current does not appear at one end of a line segment and disappear at the other. Instead, all real systems deal with loops of current. These can be approximated as dipoles where we combine the definition of dipole moment Eq. (2.8) ([36] Eq. 27.24) and Eq. (2.7) to create Eq. (2.9).

$$m = IA \tag{2.8}$$

$$B_{dipole-approx} = \frac{\mu_0}{2\pi}\frac{IA}{r^2} \tag{2.9}$$

The current times loop area represents the dipole moment of the loop. This is most accurate far from the current loop, where the detailed structure of the loop is unimportant and the enclosed loop area appears as an infinitesimal point. The error of this approximation in the plane of a loop of unit-length diameter is provided in Figure 2-3.

Another option for estimating the field from a loop of current is to calculate the field at the center of the loop. This approximation will be better for large loops of current where the measurement location is enclosed by the current path and is roughly centered. The error of this approximation both in plane and perpendicular to the circle of unit diameter are provided in Figures 2-4 and 2-5.

The center-field approximation is accurate to within a factor of 2 throughout much of the volume of interest, decaying to closer to the dipole approximation at large distances ($>$ 1 radii of the wire), and closer to the infinite line approximation at closer distances (within 0.3 radii of the wire).

2.2.4 Parallel Wires

Infinite parallel wires are a good model for many current paths in satellites, such as parallel cable wire routings and power supply paths on printed circuit boards (PCBs). When far away from two parallel wires which are close together, the distance to each

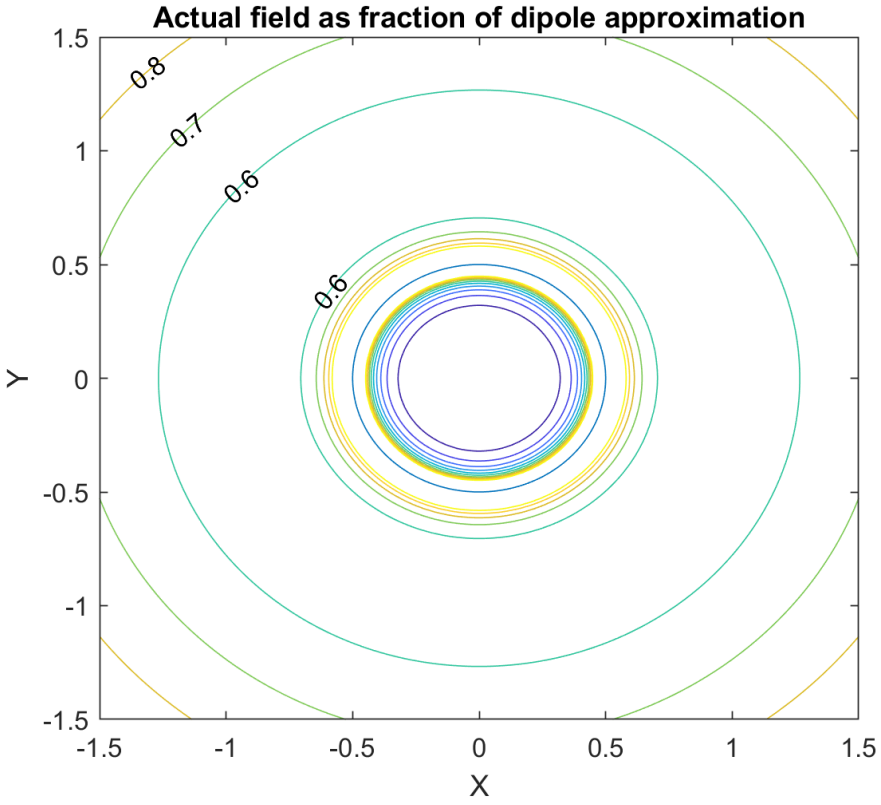

Figure 2-3: Error contours for using the dipole approximation on a current loop in the plane of the loop (XZ-plane). This approximation is most accurate at large separation.

wire is very similar, and therefore the magnetic fields mostly cancel each other. With two wires separated by d and measured from a distance r (assuming we measure in the same plane the two wires are in) then we can write the combined magnetic field as

$$B = \frac{\mu_0 I}{2\pi R} - \frac{\mu_0 I}{2\pi(R+d)} \tag{2.10}$$

In the case where d«R we can simplify to

$$B \approx \frac{\mu_0 I d}{2\pi R^2} \tag{2.11}$$

This approximation works well at distances significantly greater than d away from the wires. This is shown in Figure 2-6 where $d = 1$.

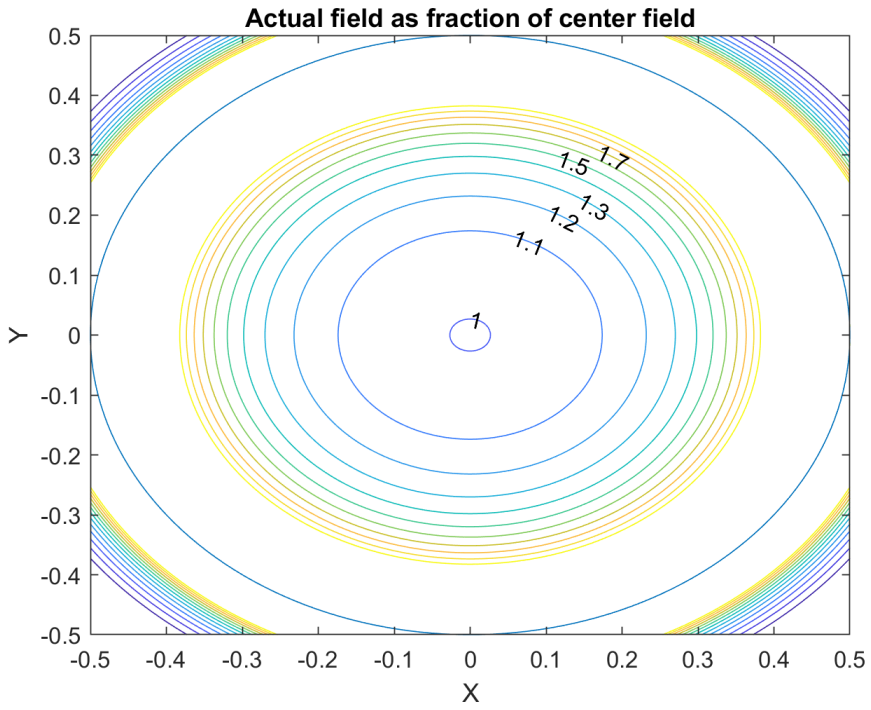

Figure 2-4: Error contours for using center-field approximation on a current loop. Magnetic fields shown in the plane of the current loop. This approximation is good near the center of the loop.

2.3 Materials

Material magnetism can be analyzed in two ways: either (1) each atom is a tiny dipole with an intrinisic dipole moment and a definable dipole vector direction, or (2) each atom includes electrons in discrete orbitals, and the net rotational motion of each electron in each orbital is effectively a current loop which will lead to a dipole moment.[6] At an atomic level, material magnetism is conceptually similar; there is a single dipole in each atom that may be arranged in any orientation and has a known dipole strength.

Material complexity is introduced when this single atom picture is expanded to include other atoms in a bulk material. Now each atom's dipole moment may interact with its neighbors and the external magnetic field. The way in which each atom interacts with its neighbors and the external fields can create three main material

[6]See Young and Freedman's University Physics Chapter 28 [36] for further reading.

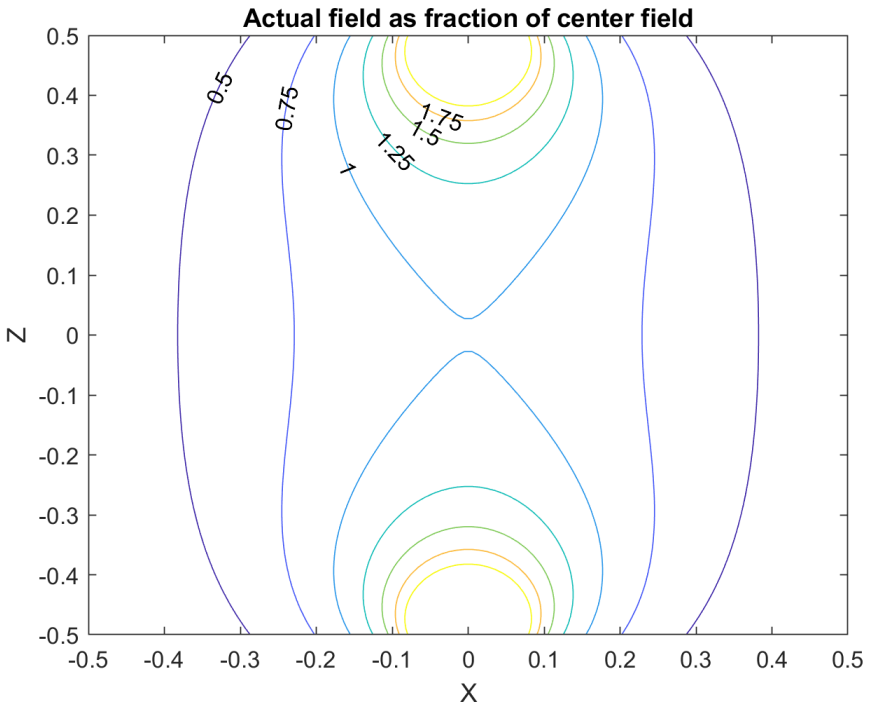

Figure 2-5: Error contours for using the center-field approximation on a current loop. Magnetic field shown in a slice perpendicular to the current loop.

categories: paramagnetic, diamagnetic, and ferromagnetic materials.

2.3.1 Material Types

Paramegnetic Materials

Important materials in spacecraft which exhibit paramagnetism include aluminum, tungsten, and lithium. Paramagnetic materials are weakly attracted to magnetic fields as the material forms an induced field in the same direction as the applied field. At the atomic level each atom of a paramagnetic material has a permanent dipole moment due to an unpaired electron in one atomic orbit. Due to thermal agitation, the dipole moments do not interact with each other and all the atoms are oriented in random directions. However, when an external magnetic field is applied, the atoms will tend to align themselves with the applied magnetic field as this is a lower energy state. This alignment is weak so the net induced magnetic field is small compared to the applied magnetic field. The magnetic susceptibility of paramagnetic materials is

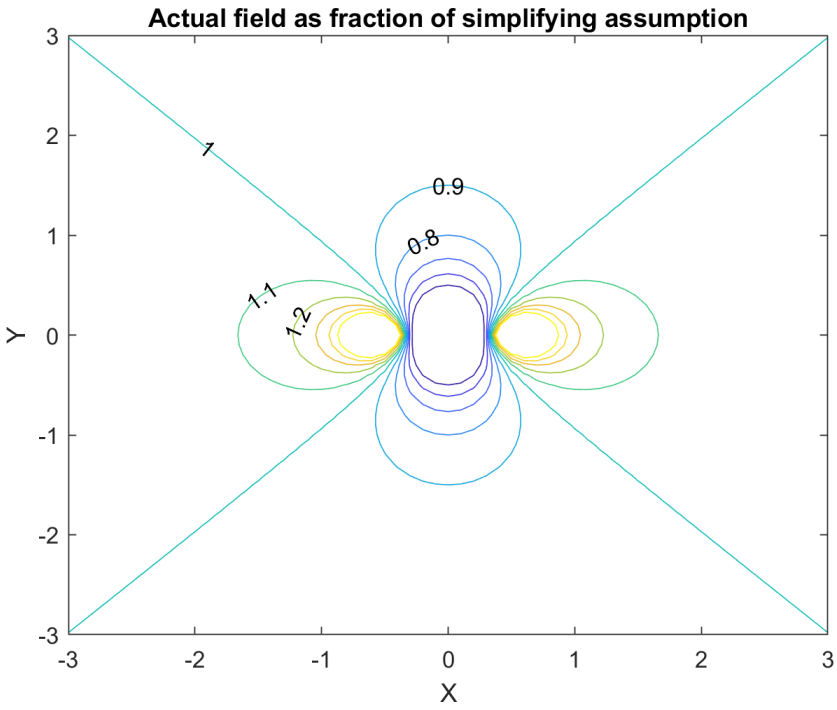

Figure 2-6: Error contours for approximating magnetic field from two parallel wires using Eq. (2.11). Length units normalized to the separation between the two wires. This approximation works best at larger distances.

positive and of order 10^{-5} [38].

Diamagnetic Materials

Important diamagnetic materials in spacecraft include copper and lead. Diamagnetic materials have no unpaired electrons and so have no permanent magnetic moment. Diamagnetic materials exhibit a weak repulsion from magnetic fields due to quantum mechanical effects. Diamagnetism is a property of all materials, but materials are only classified as diamagnetic when the diamagnetic effect is the dominant contribution to the material's magnetism. Diamagnetic materials are commonly referred to as "non-magnetic". Diamagnetic materials have a negative magnetic susceptibility, usually on the order of -10^{-5} [38].

Ferromagnetic Materials

Important ferromagnetic materials in spacecraft include some stainless steels and nickel. In ferromagnetic materials, the intrinsic magnetic moments of each atom align over distances the size of metal grains. Each of these grains has an intense magnetic field in a particular direction, but the direction of each grain is randomized such that the material is not net-magnetic. When an external magnetic field is applied, the grains which are aligned with the external field grow into areas previously occupied by other grains so that the material exhibits a net magnetization in the same direction as the applied field. This effect can be very strong, with magnetic susceptibilities on the order of 10^5 [38], so materials which exhibit ferromagnetism may be simply referred to as "magnetic".

The magnetic susceptibility of many materials are difficult to know without thorough testing as they can depend strongly on material handling and processing details. However, it is universally true that ferromagnetic materials have magnetic susceptibilities orders of magnitude larger than either paramagnetic or diamagnetic materials. Therefore, spacecraft designers concerned about magnetic interference should avoid ferromagnetic materials where ever reasonably possible. This encourages the use of common spacecraft materials such as aluminum, lead, and the "non-magnetic" varieties of stainless steel.

2.3.2 Hysteresis

Ferromagnetic materials retain some magnetization after the incident field is removed, such that a negative incident field is necessary to return the material magnetization to zero. This memory effect is called hysteresis. Hysteresis curves plot material magnetization (or "internal flux") against incident field (or "magnetizing field") as seen in Figure 2-7.

At low magnetization, the material behaves nonlinearly such that the relative permeability changes with incident field. Materials tend to have a lower permeability

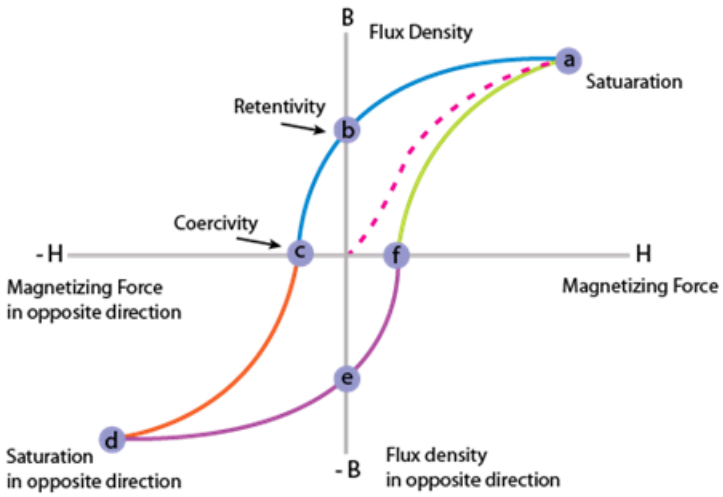

Figure 2-7: Hysteresis diagram [1].

at lower field strength as shown in Figure 2-8. If the material in question is in this nonlinear zone, the interfering field will be less than what would be calculated from a single maximum magnetic permeability value such as reported in Table 2.2.

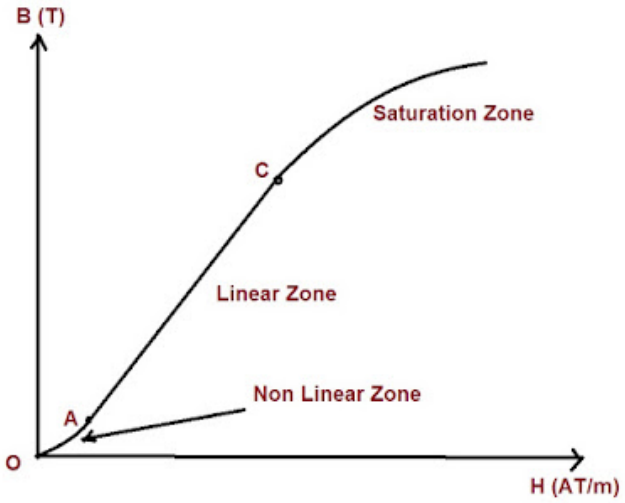

Figure 2-8: Magnetic non-linearity [2].

2.3.3 Ferromagnetic Hardness

Materials which are difficult to magnetize tend to retain some magnetic field when the external field is removed. Materials which are magnetically soft are easily re-magnetized by an external field. One way to parameterize ferromagnetic hardness is coercivity, or the amount of incident field necessary to remove a material's magnetic field.

Earth's magnetic field magnitude in low Earth orbit (LEO) is approximately 50 μT, or about 40 A/m of magnetizing force [39]. Even "soft" magnetic materials like nickel or electrical steel are hard enough that the Earth's magnetic field will not demagnetize them. Therefore, the dominant interference of most ferromagnetic materials will be a constant offset only slightly perturbed by the magnetic field of the Earth. If the material is very magnetically soft, then it will have no effective constant offset, and instead will be constantly remagnetized by the incident magnetic field as the spacecraft tumbles through Earth's magnetic field. We will use these two simplifying assumptions about ferromagnetic interference when calibrating out spacecraft self-interference in Chapter 5.

Materials which have coercivities on the order of Earth's incident field will exhibit significant hysteresis effects as the incident magnetic field on the spacecraft changes, and this hysteresis will make calibration more complicated. Such materials include nickel, raw iron, and electrical steel, so these materials should be avoided where possible, particularly near the magnetometers.

2.3.4 Materials of Interest

A summary of common magnetic materials used on spacecraft is provided in Table 2.2. Magnetic susceptibilities of about unity or less can usually be ignored except when in very close proximity to the magnetometer or when a significant volume of material is on the spacecraft. A material with coercivity near 40 A/m will be only partially remagnetized by Earth's magnetic field, so will be particularly difficult to calibrate out. Some materials have magnetic properties that depend strongly on the

incident field or history of mechanical working, so the single values reported below may not accurately represent all uses of that material.

Table 2.2: Estimated magnetic properties for some materials of interest.

Material	Magnetic Susceptibility	Coercivity (A/m)	Common Use in Spacecraft
Iron 99.8% pure [38]	5,000	80	Magnetorquer cores
316 Stainless [40]	0.002-0.01	30,000	Fastener
304 Stainless [41]	<0.8	10,000	Fastener
Carbon Steel (0.9% C) [38]	100	6000	Hardware, springs
410 Stainless [42]	100	3000	Fasteners
Nickel [38]	600	60	Connector Plating
Mu Metal [43]	100,000	0.04	Magnetic Shielding

Aluminum

While aluminum is notionally non-magnetic, it does have a non-zero magnetic susceptibility and is used extensively on spacecraft. The volume magnetic susceptibility χ_v of aluminum in the SI system is roughly 2×10^{-5}, so even completely embedding the magnetometer in aluminum will result in a maximum magnetic magnitude error of 20 ppm, and this will just appear as a constant gain offset which will be calibrated out, so we can ignore all (pure) aluminum in our magnetic analysis.

Steel

Steels may be used in spacecraft as structural elements, springs, and fasteners. General purpose (not explicitly non-magnetic) steel may be used for inexpensive hardware and can be quickly identified because it attracts a permanent magnet. This steel tends to have high susceptibility, on the order of 10^3, and may have low enough coercivity as to be partially remagnetized by the Earth's magnetic field, introducing hysteresis effects into magnetic measurement.

Non-magnetic stainless steels consist of the austenitic iron phase, but this phase is unstable under cold working and other stresses such as radiation effects. These steels gradually degrade into more magnetic phases so the magnetic susceptibility will increase. This effect can change the magnetic susceptibility from on the order of 10^{-2} to 10^{1}. Of the standard stainless steels available for fasteners, stainless steel 316 is most immune to these degradation effects, keeping a magnetic susceptibility under 0.1 even under high radiation and mechanical stress [44]. In the low Earth orbit radiation environment, the effect of radiation on steel even over a many year mission duration will be negligible, so on-the-ground screening will still be valid in orbit.

Mu Metal

Mu metal is a ferromagnetic nickel alloy designed for very high magnetic permeability and very low coercive force. Mu metal can be used to shield magnetic interference from a system generating a large magnetic field, and may be an attractive option for shielding significant magnetic sources on large spacecraft. However, the presenence of the mu-metal itself will also perturb the magnetic field measured by the magnetometer since the very high permeability material will create its own dipole moment in the presence of Earth's magnetic field (or any other magnetic field created by the spacecraft outside the mu-metal shield). If necessary, this interference could likely be filtered as a completely magnetically soft interference due to the low coercivity of mu metal, but the effect is likely to be of large magnitude and possibly non-linear so it would be better to keep fields away from the magnetometers in the first place, rather than shield sources with mu metal. Additionally, the magnetometer can not be shielded with mu metal as the local magnetic field of interest will be shielded from the magnetometer as well.

Calculating Perturbing Fields from Materials

The magnetic materials may be magnetized by manufacturing or ground handling to near-saturation, after which they will retain a strong magnetization (the magnetic

remanence). This effect is important for estimating things like spacecraft residual dipole, but as long as that field is constant while on orbit, it can be calibrated out as a static offset and so is less of a concern for magnetic sensing. The total magnetic dipole created by a material in the presence of some external field H can be calculated as:

$$m = \chi V H. \tag{2.12}$$

Where χ is the volume magnetic susceptibility,[7] V is the volume, and H is the magnetic field (A/m in SI units). From this dipole moment we can estimate the interfering field from this material using the magnetic field from the dipole equation, Eq. (2.1). When we are dealing only with field changes, we can use Earth's magnetic field of about H=40 A/m unless something on the spacecraft generates an interfering field of larger magnitude. One such source are magnetorquers, which are discussed in more detail in Section 2.5.2.

2.4 Parameterizing Magnetic Interference

2.4.1 Single-Dipole Model

The simplest way to parameterize a spacecraft's DC magnetic field is the single-dipole model. The spacecraft dipole moment can be measured in four basic ways: (1) measuring torque on spacecraft in a known magnetic field, (2) measuring the induced electromotive force (emf) in a nearby coil when the spacecraft is rotated, (3) mapping shape of magnetic field around the spacecraft, and (4) observing the attitude control characteristics once the satellite is in orbit [45].

The single dipole model works well as long as the magnetic field in the location of interest is approximated by a dipole, and this condition is met in a region called the far field. In the far field, the magnetic field shape is approximately the same as

[7] Some references denote the volume susceptibility as χ_V. Since volume susceptibility is the only dimensionless susceptibility, we drop the subscript here.

would be measured at an infinite distance. This requires that any source structure be much smaller than the distance to the measurement location. In situations where the magnetic measurement is made relatively near to the magnetic sources, a higher order model will be needed.

2.4.2 Multi-Dipole Model

In the multi-dipole model, some number of dipoles are placed in space with a given orientation and moment strength, such that six parameters can completely describe each dipole contribution (three for three-dimensional position, and three for vector moment strength). This technique is best used where very small magnetic precision is expected (on the order of 1 nT or less), and measurements will need to be made in the spacecraft's near field. The multi-dipole model is generally solved for some number N dipoles using some number M 3-axis measurements, where the relationship between N and M depends on the relative positioning of the magnetic measurements [46]. Ideally, the magnetic field would be sampled at every point on a uniform sphere surrounding the spacecraft, allowing for a complete solution of the internal magnetic field, however on the order of 100 measurements has been show to accurately model spacecraft in the near field [46].

2.4.3 Multipole Expansion

A multipole expansion of the spacecrafts magnetic field assumes that all magnetic generation is centered at one point within the spacecraft, but the field generated is parametrized as a sum of multipole moments. (For equations and further discussion see work by Ness et al. [47]) With field measurements in multiple locations around the spacecraft, the coefficients for each expansion term can be derived.

2.4.4 Dimensionality

When screening components or measuring spacecraft magnetic fields, it is useful to know how magnetic fields fall off over distance. The smaller the desired magnetic

vector resolution, the more difficult it is to make a given measurement. High resolution measurements require both a quieter magnetic environment (necessitating travel to remote locations or use of expensive shielded rooms) and may require more expensive reference magnetometers. Simple screening is better performed at short distances where fields in question are maximum. The interfering field can then be estimated at farther distances using dimensionality arguments. For example, if the object to be measured is small enough, it may be sufficient to consider the object a point source and model it as a simple dipole. Then the magnetic field falls of with the cube of distance. The use of dimensionality for simplified magnetic screening as applied to the AERO-VISTA mission is described in Section 2.4.4.

2.5 Selected Spacecraft Systems

While each spacecraft may have particular payloads or other specialty hardware which would need to be treated separately, there are also some systems which produce magnetic interference which are common to most spacecraft which we will discuss in more detail in this section.

2.5.1 Currents

Systems in the spacecraft which consume or generate significant electrical power are likely to generate large magnetic fields, because the magnetic field from a current loop is proportional to both the current and the area enclosed by the loop. For EMI (electromagnetic interference) reasons, spacecraft systems are often (but not always) routed with minimal loop area, both in the cables and within each system. This also keeps magnetic field production to a minimum.

Solar Panels

Solar panels can create a large interfering dipole because they tend to cover a larger area (frequently covering full sides of some spacecraft), and produce relatively large currents. As an example, we analyze two arrangements of the DHV-CS-10 solar panels

manufactured by DHV Technology [7]. If a particular satellite needs six of these panels in series on a 6U CubeSat, there are two representative routing techniques shown in Figure 2-9.

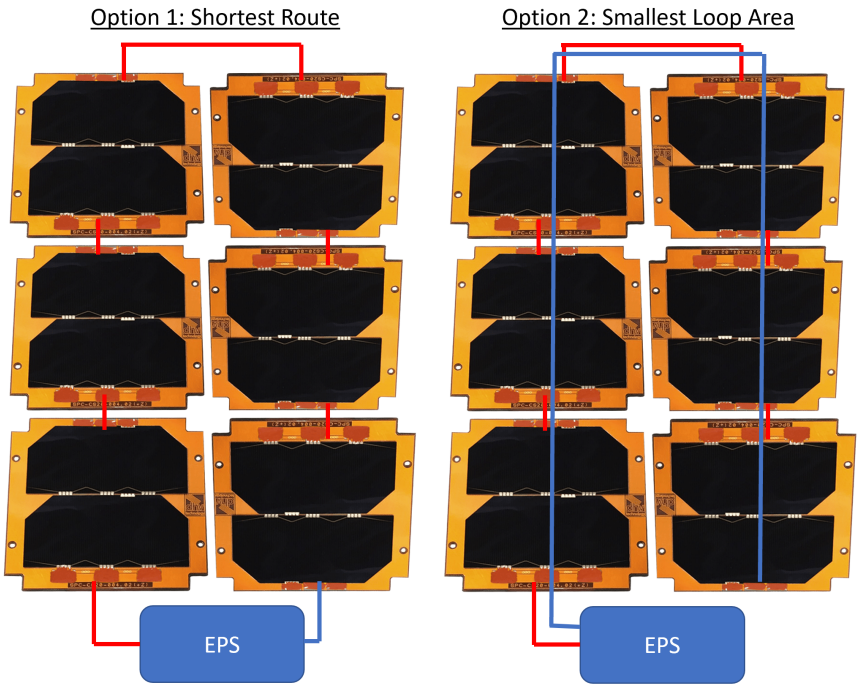

Figure 2-9: Solar panel routing options. Reduced loop area in routing reduces generated magnetic field.

Option 1, with the shortest route, creates a loop of approximately 10 cm x 30 cm. With a maximum power current flow of 0.5 A, this produces a dipole of $0.015\,\mathrm{Am}^2$, a significant fraction of the moment produced by some CubeSat magnetorquers such as the $0.02\,\mathrm{Am}^2$ of the EXA MT01 [48]. In addition to this perturbing dipole, the relatively large loop area of Option 1 would create a field of order 1-10 uT throughout much of the spacecraft. This can be approximated such as with Eq. (2.9) or is computed numerically as seen in Figure 2-10.

If the route matching in Option 2 keeps the distance between wires to less than 1 cm on average, than the total loop area is reduced from $300\,\mathrm{cm}^2$ to $70\,\mathrm{cm}^2$ with a similar reduction in magnetic field creation. Solar panel manufacturers follow this principle in the creation of solar panel arrays, as seen in the promotional picture from ISIS [3] (Figure 2-11).

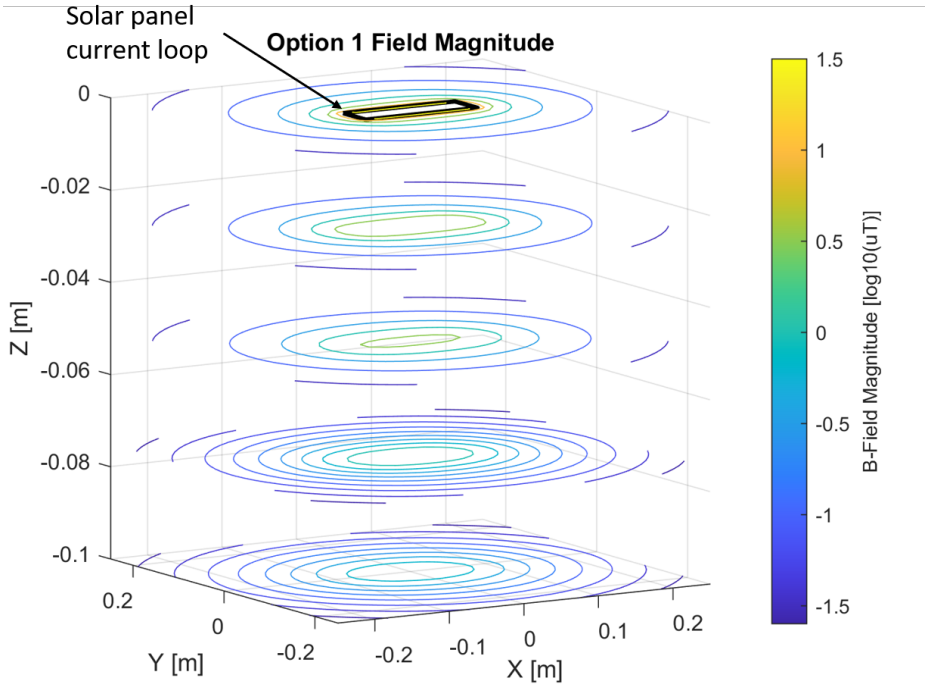

Figure 2-10: Cross sections of solar cell current interference. Large loop areas like that found in some solar panel assemblies (Option 1 in Figure 2-9) can produce large interfering fields in the spacecraft.

PCB Traces

By simply keeping the supply and return current paths symmetric and near each other, the resulting magnetic field is kept to a minimum. When the distance from the wires is significantly larger than the distance between the wires, magnetic fields from parallel wire paths can be estimated as

$$B \approx \frac{\mu_0 I}{\pi R^2} \tag{2.13}$$

PCBs are usually designed with ground planes and power planes in parallel in different layers of the PCB. Very close to the PCB, the current flowing in these planes may be best modeled as an infinite sheet of current in which case the magnetic field can be calculated as

$$B = \frac{\mu_0 J}{2} \tag{2.14}$$

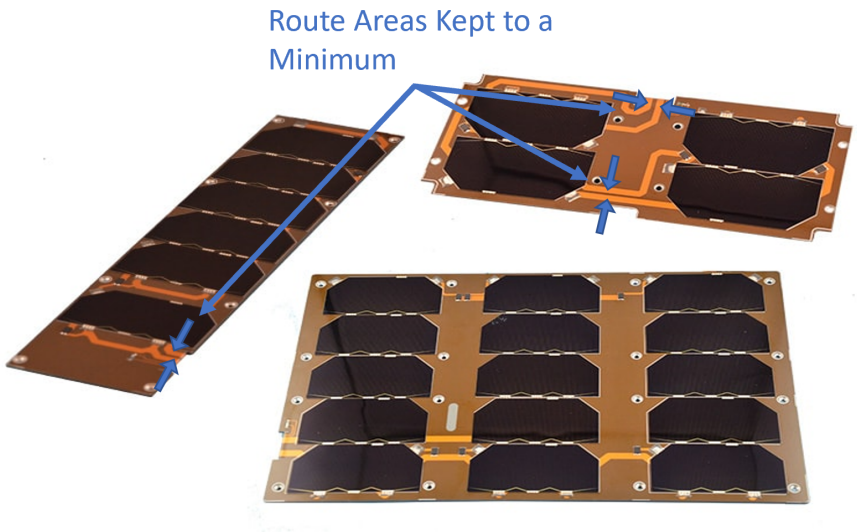

Figure 2-11: ISIS solar panel arrays have been routed for minimum current path loop area [3]. This reduces radio frequency EMI and minimizes the perturbing magnetic field.

However, very close to the PCB, the opposite return current will also appear as an infinite sheet, and since there is no distance dependence in the infinite current sheet approximation, the magnetic field will be close to zero. A more conservative approximation would be to assume that the current is not flowing in an infinite sheet, but is instead confined to a narrow wire, in which case we could use the parallel wire approximation. A typical PCB might have maximum current flow of 1 A, so the magnetic field at a component height of 5 mm above these current paths would be 0.016 T, >100x the strength of Earth's typical magnetic field. We conclude it is important to place magnetometers on PCBs in locations far away from high current power supply paths, and to ensure these currents flow in planes not traces.

Twisted Pair Cables

Twisting the cables reduces the external field beyond that for parallel wires by an amount proportional to either the pitch of the twisting or by an additional factor of the distance between the conductors as seen in work by Baltag *et. al.* [49] equations 31-33. Twisting reduces magnetic field production since consecutive loops nearly cancel each other out in the far field. It may be adequate to simply estimate an

upper bound for twisted pair cables by treating them as simple parallel conductors.

2.5.2 Materials

Materials on the spacecraft can be magnetized during ground handling or in flight. On the ground, sources of magnetizing fields include transportation and test equipment encountered during pre-launch activities. Magnetizing sources in space can include the spacecraft's own magnetorquer firing or solar panel magnetic fields. Soft magnetic materials may be significantly demagnetized or remagnetized by the Earth's magnetic field alone, so long-term effects such as magnetization from ground handling are less of a concern. Hard magnetic materials are not demagnetized or remagnetized by the Earth's magnetic field, so strong magnetization encountered on the ground or in flight are the dominant concern. This subsection analyzes common sources of both soft and hard materials found on spacecraft.

Non-Magnetic Fasteners

Many fasteners claim to be non-magnetic, but no truly non-magnetic materials exist (see Section 2.3). In particular, even very low magnetism steels can have their composition changed during cold work (repeated plastic deformation at non-elevated temperature), either in the manufacturing process, or during use. The non-magnetic fasteners which are easiest to acquire (inexpensive and short lead times) are 18-8 or 304 stainless steel varieties. However, these are likely to create the most magnetic interference of the non-magnetic varieties. The permeability of steels like 18-8 and 304 increases with cold working faster than other varieties such as 316 stainless steel [40]. Volume susceptibilities approaching 1 can be found in randomly selected 304 stainless steel hardware [41].

Stainless steel 316 is also relatively easy to acquire, having dedicated sections on websites like McMaster-Carr[8], and exhibits lower magnetization than 304 stainless steel. However, these steels can still be made mildly magnetic by the cold working

[8]As of writing, available at https://www.mcmaster.com/bolts/material stainless-steel/material 316-stainless-steel/

process. Under very high cold working, 316 stainless steel keeps a volume susceptibility below about 0.1 [44], but this is significantly higher than the about 0.002 expected without cold working. A conservative analysis can use the upper bound of 0.1, but for large fasteners relatively near the magnetometers, it may be appropriate to conduct piece-by-piece magnetic screening for fasteners with particularly desirable properties. Beyond these "non-magnetic" stainless steel alloys, there are less magnetic options made of non-ferrous elements including aluminum ($\chi \approx 2.2^{-6}$), titanium ($\chi \approx 1.8^{-6}$), and bronze ($\chi \approx 1.3^{-4}$) [38].

Magnetic Steel Hardware

Other steel hardware may be used on spacecraft including hinges or springs. If the steel lists its composition as one of the "non-magnetic" stainless steel alloys, its magnetism could be estimated with the techniques discussed in Section 2.5.2. If not, then it is safest to assume that the steel is of a magnetic variety and treat it as a magnetic variation of stainless steel or low carbon (mild) steel, with a relative permeability of 100-1000.

Connector Plating

The metal body of connector pins from reputable manufacturers are typically bronze, a non-ferromagnetic alloy. Some inexpensive connectors may use steel as the base material, so some care should be exercised in selecting connectors that will stay near magnetometers. High-quality connectors typically have a 3-layer contact finish consisting of the base material, then a nickel underplating, then tin or gold plating. Neither tin nor gold contribute significantly to magnetic pollution in the small layers found in connector plating, but the underplating of nickel can create magnetic interference due to nickel's relative permeability of 100. Nickel underplating is typically 50-150 microns thick. As an example, the ubiquitous 0.1" pitch header pins used in electronics contribute roughly $3\,\mathrm{mm}^3$ of nickel per pin.[9] Using 100 as a representative nickel relative permeability and Earth's field as a magnetizing source, each header

[9]For example, see the Wurth Electronics 6130XX family

pin would contribute roughly $1 \times 10^{-5}\,\mathrm{Am}^2$ of dipole moment. This would produce a field of about 1 uT up to 1.2 cm away in the dipole approximation.[10]

Magnetorquers

Magnetorquers are used for attitude control by producing torques against Earth's ambient field. The magnetorquers produce a dipole moment which will produce a torque given by:

$$\vec{\tau} = \vec{m} \times \vec{B} \tag{2.15}$$

Typical CubeSat magnetorquers produce magnetic moments of order 0.1 to 1 Am^2. This produces fields of 1 uT at distances up to about 0.6 m away in the dipole approximation. Therefore, accurate measurements of local magnetic field cannot be made while magnetorquers are firing unless a long deployable boom is used.

Operationally, it may be possible to require that the magnetometers be turned off during high-resolution magnetic sensing. The satellite could be allowed to freely tumble, or could rely on only reaction wheels during a magnetic data acquisition.[11]

The magnetorquer firing events can cause unexpected shifts in field for two reasons. First, the magnetorquer itself can have a remanence effect where the magnetization inside the magnetorquer material is not fully returned to zero, causing an uncertain DC offset in the local magnetic field, which depends on the direction the magnetorquer was most recently firing in. Secondly, the magnetorquer field can remagnetize other materials in the spacecraft. If the coercivity of the spacecraft material is much above that produced by the magnetorquers, then no new static offset will be created by magnetorquer firing. If the coercivity of the spacecraft material is below the Earth's magnetic field, then the material will be remagnetized by the Earth's field after magnetorquer firing, also minimizing the uncertainty created by previous magnetorquer firings. However, if the material has a coercivity that allows for mag-

[10] Header pins on magnetic sensors such as the PNI RM3100 evaluation board have the sensors as close as 5mm away from the header pins. Therefore, magnetization of the header pin is a possible source of gain or constant offset errors in these devices.

[11] Though the reaction wheels themselves will also generate magnetic interference.

netization by the magnetorquer but not by Earth's ambient field, than this material will create a memory of previous magnetorquer firings. This will look like a different DC offset in the local magnetic field after each magnetorquer firing, and calibration across different magnetorquer firing events will be particularly difficult.

In the case of a $1\,\mathrm{Am}^2$ magnetorquer, the magnetorquer field will be equal in magnitude to the Earth's magnetic field at about 15 cm distance, so materials placed closer to the magnetorquer than this could create this difficult-to-calibrate memory effect. This can be mitigated with three strategies: (i) screen for materials which exhibit coercivities which could create the undesirable memory effect, (ii) place the materials far enough away from the magnetorquer that the magnetizing field at the material is not more than Earth's magnetic field, or (iii) place the material far enough away from the magnetometer than even though the material will be differently magnetized by magnetometer firings, the field magnitude created at the magnetometer location is adequately low.

2.5.3 Summary

This section has provided some guiding equations and estimation techniques to quickly determine whether a given item will significantly pollute the spacecraft's magnetic environment. The approaches we have presented here generally only produce results within a factor of a few, and material coercivities and susceptibilities can range over orders of magnitude for different processing steps and material purities. These techniques should not be used as the only magnetic cleanliness verification for a small spacecraft, but they can allow for quick triage into categories of: (i) definitely not a significant magnetic pollutant (ii) maybe a magnetic pollutant, further testing may be required, and (iii) definitely a magnetic pollutant. Applying this simple screening early on in spacecraft subsystem development allows the spacecraft designer to develop requirements on other systems early during design trades.

The material and current path estimates used in this chapter can be simplified into the most commonly used categories as shown in Figures 2-12 and 2-13. In Figure

2-12, we separate the material into three magnetic hardnesses. The softest materials are significantly remagnitized by Earth's magnetic field (B_E), and we estimate the magnetic field with a dipole approximation on the magnetized material (see Eq. 2.7). A material with memory is magnetized by the magnetorquers but not by Earth's magnetic field; the field from this component is estimated with a dipole approximation and the magnetization computed from the material susceptibility and magnetizing field from the magnetorquer. The magnetizing field from the magnetorquer is defined as H_τ and is calculated with a dipole approximation on the magnetorquer moment m. Completely hard materials are neither remagnetized by Earth's magnetic field nor the magnetorquers; the fields from these components are calculated based on the material magnetism M as might be created during ground handling as described in Section 2.5.2.

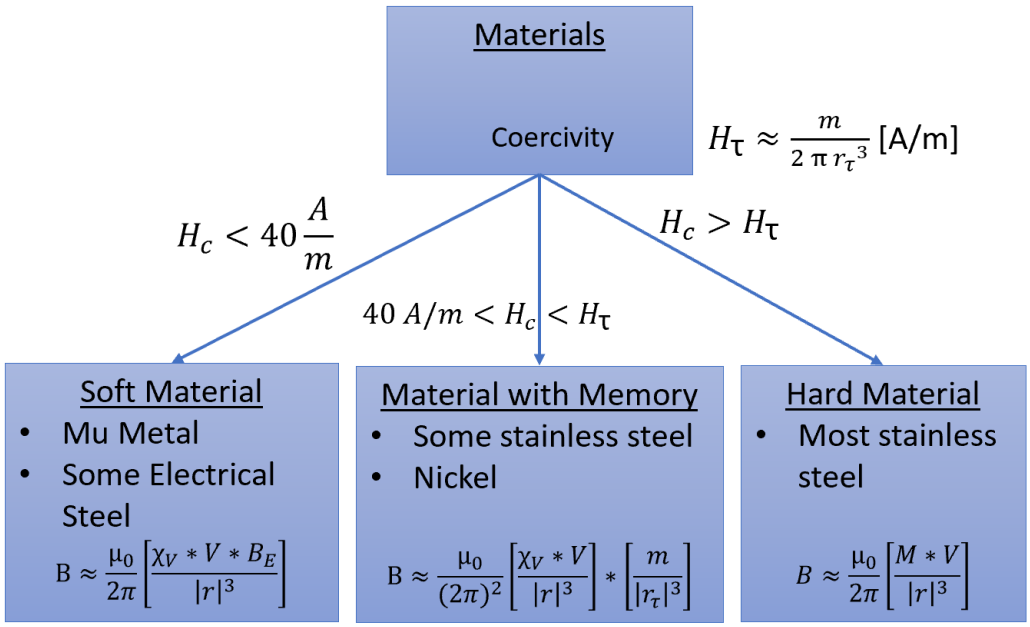

Figure 2-12: Material field estimation summary. B_E is the Earth's magnetic field, about 50 uT. H_τ is a threshold coercivity based on the magnetic moment m produced by the magnetorquer at a distance r_τ from the object under consideration. Hard materials are characterized by material magnetism M.

The magnetism produced by current paths often are often well-approximated by the three options shown in Figure 2-13. Loops that are small compared to the distance

of the measurement location are best approximated as small dipole loops, for which the field can be calculated as in Eq. (2.9). Fields close to a single wire where the return path is much farther away can be estimated as an infinite line current with magnetic field calculated as in Eq. (2.6). Currents with close supply and return paths can be approximated as parallel wires where the field is calculated as in Eq. (2.11).

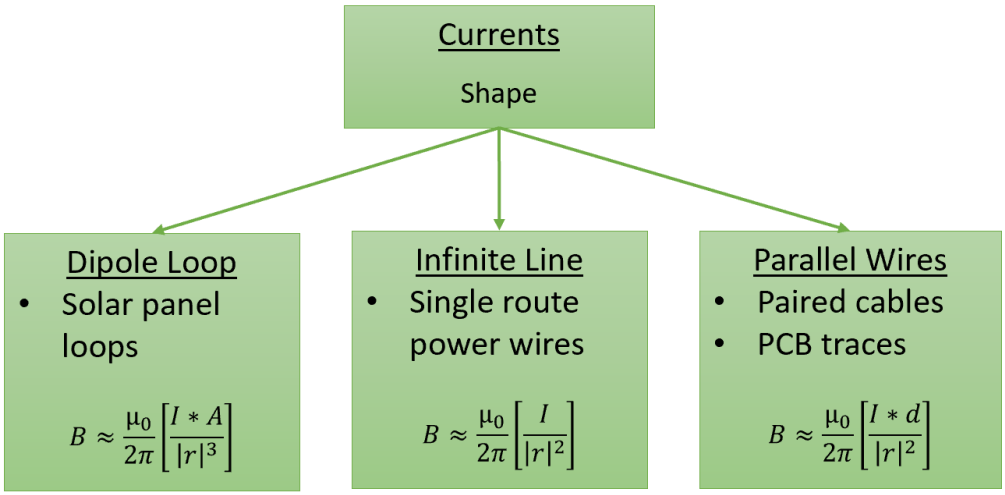

Figure 2-13: Current field estimation summary.

This page is intentionally left blank.

Chapter 3

System Level Mitigation Strategies

For space science missions that intend to measure the solar magnetic field in deep space, it is common for magnetic measurements to be made with accuracy of well under 1 nT [50]. As a result, requirements for magnetic cleanliness are often set somewhere between 0.1 nT and 1 nT at the measurement point [51]. To meet this strict magnetostatic cleanliness environment, two overarching strategies are employed: (i) move the magnetometer as far away from any interfering sources as possible, and (ii) minimize the interfering magnetic field generation as much as possible. To achieve minimum interfering fields, the magnetic measurement devices are fitted at the end of long booms of a few to several meters length, such as the 11 meter boom used on the Cassini-Huygens mission [52].

3.1 Magnetic Budget

If the length of the magnetic measurement boom is significantly larger ($>$ 5x) than the maximum dimension of the spacecraft, then the total magnetic field contribution from the spacecraft could often be approximated as a dipole using dimensionality arguments (Section 2.4.4), and we could calculate the maximum allowed dipole moment of the entire spacecraft based on boom length and magnetic measurement requirement. A naive dipole budget could be made by estimating the relative contribution to the spacecraft magnetic field of each subsystem, and divvying up the total allowed

dipole moment to each subsystem. This method is overly strict, as it neglects the fact that many dipole moments will partially cancel each other out as spacecraft with many modelled dipole moments will in general not have each interfering dipole moment aligned [53].

A more realistic dipole budget can be generated by stochastically simulating the unknown parameters as the system design evolves. Using the technique of Weikert [53], each interfering subsystem can be grouped into three categories: (i) known magnetic moment and known direction, (ii) known magnetic moment and unknown direction, and (iii) unknown magnetic moment and unknown direction. As the spacecraft design matures and more measurements are available, subsystems will proceed backwards through this list as first the mangetic moment magnitude and then direction is modeled or measured.

The estimated total magnetic moment is computed in a Monte-Carlo simulation by varying the unknown parameters such as moment and direction, and vector summing the contribution of the interfering field from each subsystem. The budget can be considered "met" if the total magnetic field at the measurement point is under the requirement at some probability level, such as 3σ. Generally, this will be a much looser requirement than the simple summing approximation. In the case of the magnetic budget for the Rosetta spacecraft, the sum of the vector magnitudes is 4.5 times that calculated by the stochastic simulation with varying unknowns [53].

As the magnetic design matures, the measured or estimated dipole contributions of each component or subsystem of the spacecraft are placed in physical space in the spacecraft coordinate system to estimate the real field at the magnetic measurement point. This is referred to as the Multi-Dipole Model or MDM [46]. This model relies on the fact that any magnetic distribution can be modelled as a sum of dipoles. Once this model is created, it can be manipulated to exercise any remaining degrees of freedom for minimal magnetic interference, and also can be used to predict the optimal location of trim magnets [54].

The creation and maintenance of both the dipole budgets and MDMs are supported by software such as GAMAG developed by ASTOS solutions [55]. Such soft-

ware can compute the field at a measurement point based on a Monte-Carlo dipole budget or an MDM, and can also solve the reverse problem by fitting a measured near-field magnetic distribution with minimal dipoles to estimate the magnetic field contribution at a boom length. This is important for spacecraft with long booms, which may be so large that they cannot fit within the uniform-field region of even very large magnetic test facilities [50].

This magnetic modelling and budgeting campaign is an effective way of minimizing total interfering magnetic field and is used for high-budget science missions such as Cassini and Psyche, which have measurement requirements on the order of 1nT down to 10 pT [50]. However, this approach is also high-effort. Even the levying of a basic dipole budget requires the creation of a magnetic cleanliness enforcement position, and in the case of Cassini [52] and Psyche [56], this takes the form of a Magnetic Control Review Board (MCRB) . It also requires participation from each of the subsystem designers. The engineers working on each subsystem might be taught best practices for magnetic cleanliness, and will spend time trying to meet the dipole budget and interacting with the MCRB to report updated best estimates. Finally, basic dipole budgets assume that each system can be modelled as a dipole, which requires that the subsystem be small as compared with the distance to the magnetometer. This is valid for long boom arm measurements, but is not generally valid for small satellites without deployables.

In the case of small-satellite science without deployable booms, and without a magnetic control board, the dipole budget of each subsystem and even each component may be a poor estimation of the magnetic contribution of the field at the measurement point. This is because the measurement point is close enough to the material that they are physically large and not well approximated by a single dipole. Instead of the resource intensive method of levying requirements on every component or subsystem, on AERO-VISTA we have sought to optimize material trades and placement where possible and where maximum benefit could be achieved. We also rely heavily on our ability to calibrate out the spacecraft effects (see Section 5). We make decisions not just based on the incident field created by a subsystem

or component, but also by the ease or difficulty by which that contribution may be calibrated.

3.2 Boom Measurement

On missions using a boom for magnetometer separation, the final boom length is determined iteratively with the development of the rest of the system, including the analysis of the dipole budget and the Multi-Dipole Model. While we are using the term "boom" to represent the distance of the magnetometer from any interfering sources, the concept of separation includes non-deployable structures. For example, long satellites may be able keep magnetically active systems many centimeters away from the magnetic measurement devices even without a deployable structure.

The boom measurement greatly reduces the coupling of spacecraft magnetic fields to the magnetic measurement device. In a common scenario of a predominantly dipole moment, the magnetic field will fall with the cube of distance. As discussed in the Section 2.4.4, other higher order terms in the multi pole expansion will fall-off even faster.

The boom length is chosen to provide adequate mitigation of magnetic fields at the sensor. Longer booms provide more magnetic isolation, but are more complicated and expensive to develop and deploy in space. Disadvantages of long booms include: (i) increased development cost to develop deployable device, (ii) increased project risk with boom deployment, (iii) increased difficulty in ADCS control with a long flexible deployable which can couple into spacecraft dynamics, (iv) increased launch mass and spacecraft size, and (v) uncertainty in magnetometer orientation caused by flexible connection from boom tip to spacecraft. With improved magnetic cleanliness and filtering techniques, the sensitivity of any magnetic measurement can be improved without resorting to a longer boom.

3.3 Magnetic Screening

Magnetic screening on spacecraft components before assembly or even during the prototyping stage can identify magnetically problematic components early in the design and integration cycle. This is desirable because it allows the relevant subsystem engineers to find alternative components or mitigation strategies for the offending component.

Magnetic screening is a viable primary method for system level magnetic interference mitigation even for some large and expensive missions. For the Advanced Composition Explorer (ACE) spacecraft "an informal process of screening and design review was maintained by the Johns Hopkins Applied Physics Laboratory (APL) and individual experimenters" [57]. The ACE spacecraft achieved $<$0.35 nT magnetic interference at the magnetometer location 4.19 meters from the center of the spacecraft [57].

Magnetic screening may be less resource intensive than levying a dipole budget on the different subsystems. First, it reduces the level of systems design effort by removing the need to generate and maintain a system level dipole budget or to create a magnetic dipole model. Secondly, it reduces the burden on the subsystem engineers to minimize or characterize the magnetic properties of their subsystem. Instead, the subsystem engineer can periodically work with a magnetic cleanliness engineer to ensure that some key components or the whole subsystem are adequately magnetically clean. Using only magnetic screening of suspect problem components does incur risk of unexpected interference from an unmeasured source, so a rigorous dipole budget and magnetic dipole modelling methods may still be needed on some missions. However, the cost trade-off is desirable for low-cost short-development time missions like CubeSats.

3.3.1 Screening Methods

Handheld screening

A first pass check of magnetic interference can be performed with a handheld magnetometer to look for magnetically "hot" materials [56]. This simple screening technique can be applied as follows:

1. Measure the magnetic field in a location where the magnetic field is adequately quiet and constant. [1]

2. Introduce the item to the vicinity of the handheld magnetometer and see if the magnetic field significantly changes.[2]

3. Record whether the material passes this screening stage as "not an item of concern" or "possibly an item of concern".

See section 6.4 for an example application of using this screening method with inexpensive magnetometers such as those found in a commercial cell phone.

More detailed measurement

Items which are recognized as magnetically "hot" or categorized as an item of potential concern, should be measured in more detail. Either a single measurement could be made with careful dimensionality analysis to estimate the incident field at the magnetic measurement location (see 2.4.4), or the multi-pole moment or MDM could be measured as would normally be used for the system level measurement (see Section 3.6).

[1] See section 6.1 for a discussion of requirements on magnetic quietness and where those locations might be found

[2] At this stage "significantly changes" may be estimated by a simple dipole model with a significant factor of safety of order 10x. Items that approach the magnetic measurement requirement should be considered "of possible concern" at this stage

3.4 Component Placement

For the purpose of magnetic cleanliness analysis, there are two types of components of interest: the magnetic measurement device (magnetometer), and devices which can perturb the magnetic environment. Since magnetic fields decrease with distance, the first order of business is to keep the interfering devices as far away from the magnetic measurement device as possible. If some more detailed knowledge of the interfering sources are known, then other placement optimizations can be made.

One way to optimize placement is to create opposite pairs to mostly cancel out each other's magnetic field. The opposites can be either materials or current paths. One instance of creating opposite pairs in current is the twisted pair cable or paired solar panel routing discussed in Section 2.5. Here the current flowing in an interfering cable is mostly cancelled out by placing it near a cable with current flowing in the opposite direction. An example of cancelling dipole moments might be to break a circuit board inductor into two inductors in series with the second inductor placed such as the effective dipole generated will be in the opposite direction as the first dipole. This effectively cancels the dipole moment at large distances so the quadrupole moment dominates. This is desirable because the quadrupole moment falls with an additional factor of distance [35].

Finally, if a detailed magnetic model of the spacecraft is available, component placement of both the magnetometer and interfering systems can be adjusted to create localized areas of minimized field using techniques like Monte Carlo simulations such as discussed by Nikopolous [54].

3.5 Trim Magnets

Trim magnets can be used for two reasons:

1. Majority cancellation of a system with known permanent DC magnetic field. This effectively is creating an artificial cancelling pair as discussed in Section 3.4.

2. Adjustment of spacecraft dipole moment for ADCS considerations (not magnetic measurement cleanliness reasons).

One example CubeSat which needed a trim magnet was ASTERIA, which flew with a residual magnetic moment of about $0.17\,\mathrm{Am}^2$, while the torque rods were only able to generate $0.125\,\mathrm{Am}^2$ [58]. The addition of a trim magnet to counteract the constant spacecraft moment would have helped with momentum management during ASTERIA operation [58].

3.6 System Measurement

Measurements of magnetic fields around large systems or around the entire spacecraft are used as the final validation step for magnetic cleanliness efforts. The measured field may be taken at the final location of the magnetometer where a simple one-to-one comparison of perturbing field to measurement requirement can be made. Alternatively, measurements made at other locations enable the creation of magnetic models as discussed in Section 3.1. This model is then used to estimate the perturbing field at the measurement location.

3.6.1 Verification at Measurement Location

One simple way to verify magnetic constancy is to place a reference magnetometer (or the final science magnetometer) in the actual spacecraft measurement location and then measure the magnetic field at that location for noise and drift. This measurement will necessarily be limited by the capabilities of the magnetometer, but can be used as long as the magnetometer itsef is able to measure the desired precision.[3] This method will not determine whether there are static spacecraft magnetic fields unless the background magnetic field can be subtracted or nulled such as by using a magnetic test chamber of concentric Helmholtz coils [50].

Verification of magnetic constancy and repeatability should show the necessary repeatability over expected environment variation. This could include (i) changing

[3]This method was used on AERO-VISTA to screen for magnetic hysteresis as described in 6.3

incident field, such as when the satellite tumbles through Earth's magnetic field, or (ii) changes in satellite operational state, such as turning payload components on and off. The effects from changing incident field can be verified by rotating the spacecraft in Earth's magnetic field before returning to the starting position to repeat the measurement, and the changing of operational state can be achieved by commanding the spacecraft during ground testing. Verifying the repeatability of the measurement over spacecraft rotation requires the ability to return the spacecraft precisely to some previous orientation, and the validations obtained from these measurements will only be as good as allowed by the magnetic noise at the measurement location (see Appendix C for detailed measurements of environmental noise).

3.6.2 Fitting

Multiple measurements of the spacecraft magnetic field can be combined to model the magnetic field of the spacecraft. This model may be a simple dipole model, a multi-dipole model (MDM) or an expansion of multipole moments in spherical harmonics. These require several measurements around the spacecraft at known locations together with fitting algorithms as discussed in references in Section 2.4.

3.7 Summary and Application to AERO-VISTA

This chapter has surveyed some methods by which missions achieve and prove the necessary magnetic cleanliness to make science measurements precise to 10 nT or less. We discussed (i) the development of a magnetic interference budget, (ii) measurement from a long boom, (iii) screening of potentially magnetic components and subsystems, (iv) component placement, and (v) trim magnets.

Most missions referenced here had budgets of about $100 million (ACE [59]) to $3 billion (Cassini [60]), so the methods used for design and verification of the magnetic sensor and magnetic cleanliness are going to naturally be different than those used on inexpensive ($1-10 million) CubeSat missions like AERO-VISTA. Additionally, magnetic measurements are secondary data products for the AERO-VISTA mission.

The measurements of the magnetic field are helpful in meeting many high-level science requirements, but are only required for one L1 requirement [4]. Therefore, much less development effort has focused on the magnetometers and magnetic sensing than on other mission activities. With limited resources available, we have sought to learn from the formal methods and advanced missions while acknowledging we do not have the resources to perform the same testing and verification.

Magnetic Interference Budget Formal budgeting of magnetic interference would have us tracking the maximum expected magnetic interference from each major component or each subsystem on the spacecraft. We would ensure that the total interference summed using directionality assumptions (or Monte Carlo analysis) would produce interference below our measurement floor. While we have not tracked the total expected field from all components, we have instead recognized that the interference of the entire budget is frequently dominated by one or a few large sources due to the generally random nature in which the interference vectors add together. Therefore, we measure and mitigate major possible interfering sources individually while not yet tracking the potential summing effects of multiple interferers.

Boom Measurement AERO-VISTA could not afford another long deployable to place the magnetometers at the end of a long boom. Instead, we have placed the magnetometer as far from major spacecraft systems as possible and put the magnetometers in the very extreme "top" corners of the spacecraft where the largest and most power hungry spacecraft subsystems reside about 30 cm away at the "bottom" of the 6U spacecraft bus.

Magnetic Screening When a potentially magnetic component or material is considered for budget or development time reasons, a quick magnetic screening is performed to estimate whether the proposed component might create interference approaching the precision requirement at our magnetometer location (see Chapter 6).

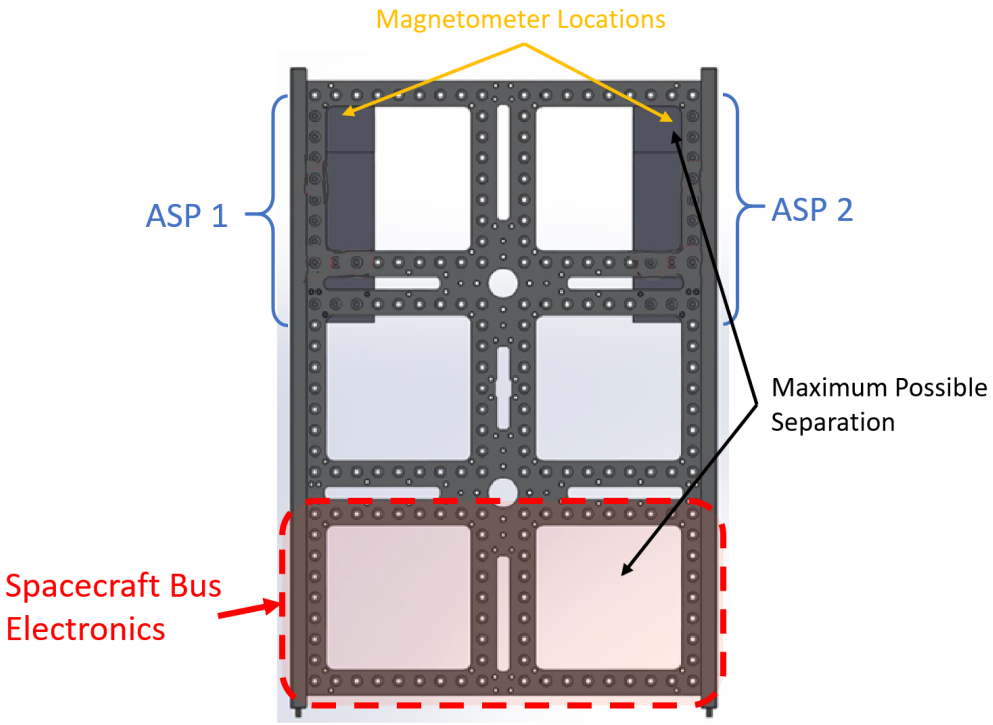

Figure 3-1: Magnetometers are placed as far away from powerful bus electronics and magnetorquers as possible in the 6U spacecraft.

This page is intentionally left blank.

Chapter 4

Magnetic Sensor Requirements and Expected Performance

Early in the magnetic system design, the high level scientific requirements are mapped into lower level requirements on the magnetic sensing subsystem. The requirements flow depends on the properties of the selected magnetometer. Magnetic sensing technologies can have different non-ideal properties which together contribute to total magnetic error. For the AERO-VISTA mission, we require magnetic measurements with 100 nT precision at 10 samples per second [4]. In this chapter, we compare the precision requirement to the performance of our selected magnetometer, the HMC1053 anisotropic magnetoresistive (AMR) magnetometer made by Honeywell Aerospace (for details on our magnetic sensor design, see Chapter 7). We map the non-ideal properties of the magnetometer to expected total error using both the datasheet parameters and actual magnetic measurements of magnetometer performance. With this parameterization, we are prepared to implement the calibration method discussed in detail in Chapter 5.

4.1 Performance Metrics

There are several metrics for magnetic sensing performance commonly encountered in requirements and datasheets. Here we briefly define some important parameters

which are used in the rest of this chapter.

Accuracy and Precision An accurate measurement reports results that are on average near the "real" value. A precise measurement may not be on average near that real value, but the spread is small when a measurement is repeated.

Resolution Resolution is the minimum change which can be distinguished relative to the full measurement range. For example, a signal which is discretized into an 8-bit value has 2^8 resolution elements. Resolution may also be used to describe systems whose precision is noise limited, such as completely analog measurements. For example, the HMC1053 magnetometer reports a resolution of 120 μGauss for a bandwidth of 50 Hz [61], equivalent to the noise floor in the given bandwidth.

Sensitivity The sensitivity of a measurement is the minimum change which can be distinguished in absolute terms or physical units. Two magnetometers with the same mapping of least significant bit to magnetic field have the same sensitivity, but a magnetometer with more bits has a different resolution. For example, the PNI RM3100 magnetometer reports magnetometer performance as a sensitivity of 13 nT [62].[1] This sensitivity is the magnetic field per LSB and does not include noise effects, though some definitions of sensitivity include the noise (such as the deconfusion guide by Electronic Design [63]).

Noise Magnetic noise is an apparent changing of the magnetic signal when the incident field is actually constant. The magnetic noise of sensors is sometimes reported as a single value, such as for the RM3100 with noise of 20 nT (or something similar depending on setting details) [62]. However, noise is generally a frequency dependent effect with larger noise spectral density at lower frequencies. If measurements are assumed to be be independent, simply measuring at a higher rate could improve the effective noise floor by a factor of $\sqrt{N}$ for an N factor increase in the number

[1] The RM3100 magnetometer was originally selected for use on AERO-VISTA, but later removed for EMI concerns. See Appendix D for details.

of measurements [64]. In practice, this often does not help, because increasing the sample rate increases the bandwidth over which noise is collected. See Appendix C for a detailed discussion of measuring magnetic noise and its spectral characteristics.

Repeatability Repeatability is the ability to read the same value from the sensor repeatedly when the same incident field is a applied. Repeatability is similar to precision, but precision usually characterizes two measurements made one right after another with minimal time and environmental change between the two measurements. Repeatability can be used more broadly to describe the difference between two measurements when more time or environmental variation has occurred between the two measurements. Magnetic devices often exhibit repeatability errors between power cycles or when significant changes are made to the magnetic environment. For example, the HMC1053 reports a repeatability error of 0.1% of full-scale when 3 sweeps across ± 3 Gauss are made [5]. This is 100 times the resolution limit reported by the same device. For AERO-VISTA, the requirement for precision also implies repeatability to the same level during spacecraft operations over an orbit. The AERO-VISTA mission expects to use magnetic map values at low-latitudes to calibrate measurements at higher latitudes where science collection occurs (see Section 5.4). This takes approximately 15 minutes and may involve spacecraft tumbling, so our precision requirement is tied together with a repeatability requirement over this amount of time with a potential incident field change of about ± 1 Gauss (roughly the magnitude of Earth's magnetic field).

4.2 Measurement Requirements

The science requirements flow into mission requirements which themselves flow down into instrument specific requirements. By mapping each requirement to a parent requirement we ensure that verifying each lower level requirement will allow us to meet the higher level mission requirement. The flow of science requirements into payload requirements for the magnetometers in the AERO-VISTA mission is summarized in

Figure 4-1 and drawn from the AERO-VISTA requirements documents [4]. In this chapter we will base magnetometer performance comparisons against the 100 nT precision requirement, keeping in mind this also requires repeatability across environmental variation.

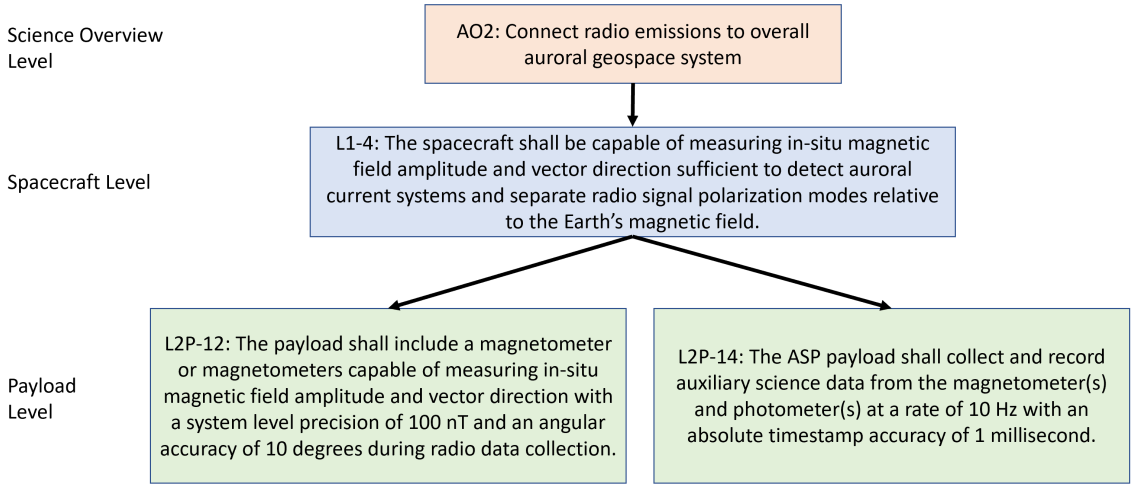

Figure 4-1: Magnetic requirements flow from the high-level science goals to the payload-specific requirements. Requirements and labels come from AERO-VISTA requirements documents [4].

4.3 Non-Ideal Properties

Ideally, we would be able to compare the requirements flowed down to the instrument level in Section 4.2 directly to datasheet parameters, and therefore prove that our system will meet the measurement requirements by analysis. In reality, there are effects beyond the simple requirement parameters discussed in Section 4.1. Some of these parameters may be ignored if they are of sufficiently low magnitude; others may need to be calibrated out, still others may need to be accepted. We categorize non-ideal effects for the HMC1053 based on datasheet analysis in Section 4.4.1 and measure the actual error contribution of these non-ideal properties for one device in Section 4.4.2. The relative importance and interaction of these non-ideal effects are used to inform the measurement equation and calibration method discussed in Chapter 5.

4.4 HMC1053 Non-Ideal Properties

In this section we evaluate how the non-ideal properties of the HMC1053 affect the precision and repeatability for the AERO-VISTA magnetometers. These effects are compared to the requirements in Section 4.2.

4.4.1 Datasheet Interpretation

The HMC1053 datasheet [5] reports typical values for some non-ideal properties which we can evaluate by mapping the datasheet parameters to our mission requirements. Figure 4-2 shows a summary of the errors, where the values in red are above our measurement precision requirement of 100 nT, and therefore will have to be calibrated out. The values in green are below the precision requirement and therefore will not need to be calibrated. In this subsection, we discuss how each parameter is mapped to the expected contributed error reported in Figure 4-2. In Section 4.4.2 we report the actual measurement of contributed uncertainty from the HMC1053's non-ideal effects.

Linearity Error Ideally, the output signal would be proportional to the applied magnetic field. Non-linearities in this transfer function are quantified by the linearity error. The datasheet reports a linearity error of 0.1% over a measurement range of ± 1 Gauss. Taking the full-scale range to be 1 Gauss, this is an error of 1 milliGauss or 0.1 uT. However, we expect the measurement range to be ± 0.5 Gauss, not a full ± 1 Gauss. So at a minimum we can expect the linearity error to be half the value we just calculated (50 nT). Plotting the trend of error percentage over measurement range shows that the error grows faster than linear with measurement range (see Figure 4-3), so we may get even better performance than this.

Hysteresis Error Hysteresis effects create memory in the magnetic measurement which is difficult to calibrate. The hysteresis error reported in the datasheet is 0.06 %FS when swept over ± 3 Gauss. This corresponds to an error of 0.18 uT. If the hysteresis error scales at least as fast as linear we can expect a hysteresis error of less

Effect	Uncertainty /Error (typical)	Error in nT
Sensitivity	20%	10,000
Sensitivity Tempco	600 ppm/C	1500
Cross-Axis	3% FS	1500
Offset Tempco	500 ppm/C	1250
Linearity	0.1% FS	50
Hysteresis	0.06% FS	25

Figure 4-2: Magnetic errors due to selected non-ideal effects of the HMC1053 as calculated from the datasheet parameters. Values in red are above our precision and repeatability requirement of 100 nT, values in green are below this threshold. FS indicates a percentage of full-scale.

than 30 nT. This would place it under our measurement requirement, but verification by test is appropriate given that we have assumed the scaling of the hysteresis errors with changing full scale range.

Repeatability Error The repeatability error is reported as 0.1% of full-scale over the range of ±3 Gauss. Using the same analysis and assumption as for the hysteresis error, we can expect a measurement error of no more than 50 nT, but this too should be verified through test, as we have assumed a relationship between full-scale range and sensitivity.

Bridge Offset The Wheatstone bridge used for magnetic sensing is not perfectly balanced due to manufacturing tolerance, even if no magnetic signal is applied. The bridge offset is as large as ±1.25 mV/V [5], which maps to a measurement uncertainty of 1.25 Gauss, more than double the magnitude of Earth's magnetic field. This offset is largely corrected without calibration by the use of polarity switching with the

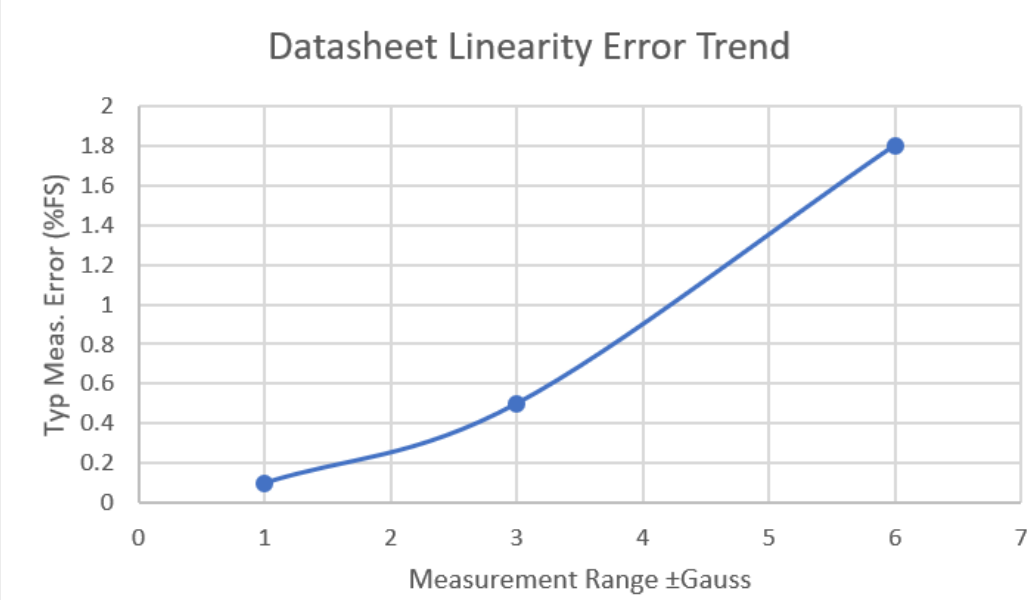

Figure 4-3: Linearity error as a percentage of full scale increases faster than linear with the magnitude of the full scale applied field. The data points in this plot are taken from text in the HMC1053 datasheet [5].

magnetometer set/reset straps as discussed in Section 7.6.

Sensitivity In this context, sensitivity refers to the transfer function from incident magnetic field strength to electrical signal strength. This is given as nominally 1.0 mV/V/G where the extra Volts unit in the denominator accounts for the difference in bias voltage. The sensitivity uncertainty by datasheet parameters is 0.2 mV/V or 20% of the measured magnitude.

Sensitivity Temperature Coefficient The sensitivity of the magnetometer (again in this context, the sensitivity refers to the transfer function mapping incident magnetic field to signal level) changes with temperature by a typical value of -2700 ppm/°C with a ±300 ppm/°C uncertainty. We map this into measurement uncertainty using the total temperature range expected to be experienced by the magnetometers onboard the satellite. We expect operational temperature to range from about 0 °C to 50 °C, so the change in measurement may be as great as about 13.5% with an uncertainty of 1.5%. Over the full-scale range of 50 uT, this will result in measurement uncertainty of up to 750 nT.

Bridge Offset Temperature Coefficient The static bridge offset changes with temperature at a typical rate of 2500 ppm/°C with 400 ppm/°C uncertainty. This fraction is with respect to the static bridge offset corresponding to a field strength of about 125 uT. Therefore, the offset change with temperature is up to 313 nT/°C with uncertainty of 50 nT/°C. Even over very small temperature changes, this effect will need to be calibrated. The rate of temperature change calculated here is used together with spacecraft thermal analysis to choose the set/reset sampling technique as discussed in Section 7.6.

Cross-axis Effect The cross-axis effect is reported as ±3% FS at 1 Gauss applied and 1 Gauss cross-field. For a measurement of 50 uT of Earth's field we can expect a maximum cross-axis effect of 1.5 uT.

Noise Noise is a quantity which varies over frequency. The HMC1053 specification table lists a noise spectral density at 1 kHz of $50\,\mathrm{nV}/\sqrt{\mathrm{Hz}}$, but this is not representative of noise performance at lower frequencies. The "Noise Characteristics" section of the datasheet provides the following descriptions [5]:

- The noise density is $50\,\mathrm{nV}/\sqrt{\mathrm{Hz}}$ at the 1 Hz corner
- The noise density drops below $10\,\mathrm{nV}/\sqrt{\mathrm{Hz}}$ at 5 Hz
- The noise density fits the Johnson Noise value of $5\,\mathrm{nV}/\sqrt{\mathrm{Hz}}$ beyond 50 Hz
- The 10 Hz noise voltage averages around 1.4 micro-Volts[2]

To better understand this textual description, these point parameters were combined to estimate a plot of the spectral noise density of the HMC1053s as described in detail in Appendix E. As in Appendix E, we assume that the noise density falls log-linearly from the specified data points. For frequencies below 10 Hz we use the 10

[2]There is some ambiguous terminology used in the noise characterization of the HMC1053; given the frequency domain description, we would expect far less low frequency noise in the 10 Hz bandwidth than the 0.8 uV quoted as the "standard deviation". We would instead expect a value closer to 0.2 µV as we would calculate by dividing the "noise voltage average" by 6 to find 0.23 µVrms. While the AERO-VISTA mission will meet our requirements with the 0.8 µV value, we have verified in testing (see Section 4.4.2) that the 20 Hz bandwidth P2P noise is at most about 1.6 µVpp. Therefore, we can conclude that the "noise voltage average" of 1.4 µV is referencing a P2P value (not rms) in the stated 10 Hz bandwidth.

Hz standard deviation integrated value. At the lowest frequencies we have assumed the flicker noise spectral dependence of 1/f. At high frequencies we have used the Johnson-Nyquist noise approximation which is flat with increasing frequency. This allows us to plot the noise as in Figure 4-4.

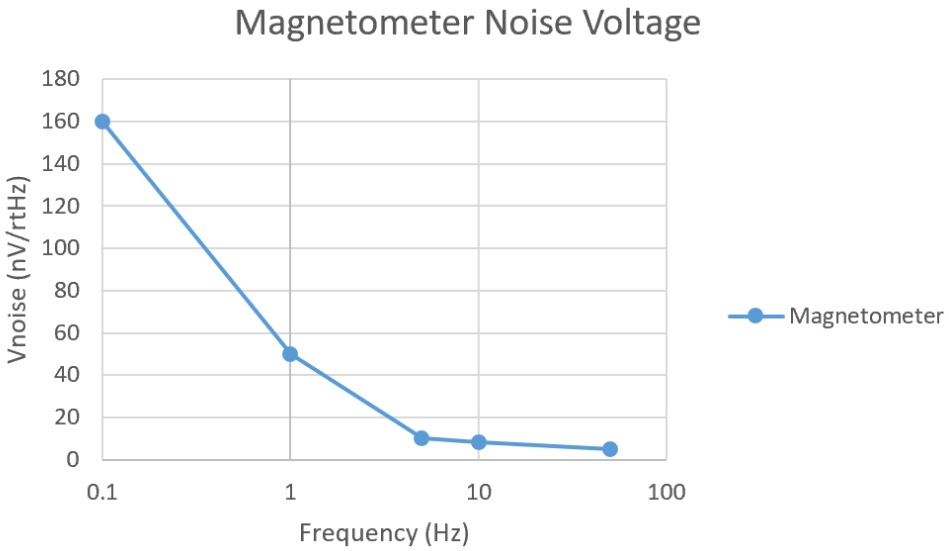

Figure 4-4: HMC1053 noise power spectral density using datasheet parameters. See Appendix E for a detailed discussion of converting from point values to spectral noise density plots.

We are interested in the expected noise floor at our requirement system sample rate of 10 Hz, and at the actual ADC sample rate of 50 Hz.[3] We can integrate the total piecewise equation to find the expected rms and peak-to-peak (P2P) noise. We assume that the P2P noise is six times the rms noise [65]. By integrating our piecewise equation (plotted in Figure 4-4) over the frequencies of interest we compute the P2P noise values summarized in Table 4.1. We will meet our magnetic measurement precision requirement if the uncertainty is noise dominated, even in the case of looking at P2P noise up to 50 Hz.

[3]The sample rate of 50 Hz comes from practical decimation limits for our selected ADC as discussed in Chapter 7.

Table 4.1: Magnetic noise in frequency ranges of interest. The contribution from 10 Hz to 50 Hz is dominated by the contribution from DC-10 Hz so the total value from DC-50 Hz is the same as from DC-10 Hz to within 2 significant figures.

Freq range[1]	rms V(uV)	P2P V (uV)	rms B^2(nT)	P2P B^2 (nT)
DC - 10 Hz	0.23	1.4	9.4	57
10 Hz - 50 Hz	0.04	0.24	1.0	6.0
DC - 50 Hz	0.23	1.4	9.4	57

[1] In integration we have considered any value reported at 0.01 Hz to be equal to the value at DC.
[2] We have used our instrument bias voltage of 4.096 V to map the voltage noise to equivalent magnetic field noise.

4.4.2 Measurement of HMC1053 Non-Ideal Properties

This section evaluates the accuracy and stability of the HMC1053 magnetometer as implemented on the MagEval test board. The MagEval test board is a custom PCB implementation of our magnetic sensing instrument without worrying about flight form factor or reliability. This system integrates the HMC1053 magnetometer with pre-amplifiers, an ADC, and a Raspberry Pi for control. This has been used to verify the performance of the HMC1053 magnetometers and also reduced design risk going into the Engineering Model. See Section A.2.1 for design details and more lessons learned. In this section we use the MagEval magnetometer implementation to identify non-ideal contributions to the measured field and validate assumptions made in the datasheet interpretation in Section 4.4.1. These results inform the creation of the calibration model implemented in Chapter 5.

Equipment and Testing Setup

In this testing campaign, the following equipment was used to exercise all expected non-ideal properties as identified in Section 4.4.1:

- Low static magnetic-field room in MIT's EAPS Department Paleomagnetism Laboratory.

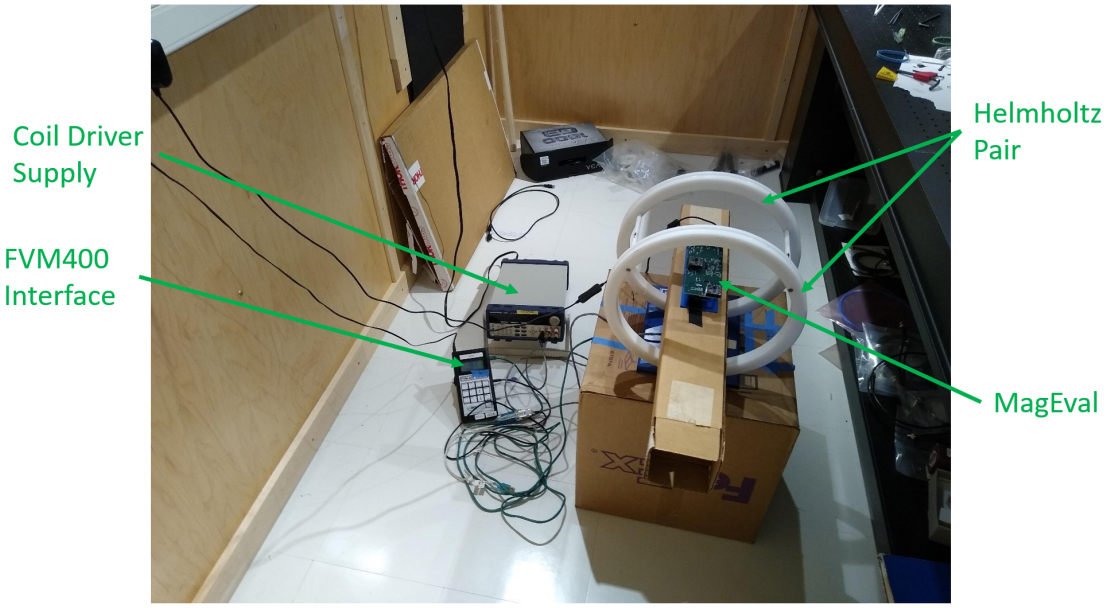

Figure 4-5: Test setup in MIT's Department of Earth, Atmospheric, and Planetary Sciencies Department Paleomagnetism Laboratory. In this facility, the static magnetic field magnitude is kept below about 1 uT and environmental noise is reduced.

- MagEval (see Section A.2.1) with Raspberry Pi Zero serving as driving computer.
- FVM-400 Vector Magnetometer. [66] with serial to USB converter.
- Smart phone with mobile-hotspot turned on for SSH networking.
- Laptop for data interface to the FVM-400 and to SSH into MagEval.
- Single-axis two-coil magnetic generator (a Helmholtz pair).
- Variable DC power supply for the magnetic generator.
- Hot air gun to create temperature variation.

MagEval Configuration MagEval has both RM3100 reference magnetometers installed and the bias voltage is provided from the internal 2.5V reference. The software implements the measurement of a single axis with the following sequence (see Chapter 7 for magnetometer design details, and Section A.2.1 for MagEval details).

1. A set pulse is provided to the HMC1053
2. The ADC is reconfigured to reset the conversion

3. The next conversion is stored as a positive measurement
4. A reset pulse is provided to the HMC1053
5. The ADC is reconfigured to reset the conversion
6. The next conversion is stored as a negative measurement
7. The effective measurement is created by averaging the positive and negative pulse readings $val = \frac{positive - negative}{2}$

The ADC is configured to 20 SPS, which is slow enough that the Raspberry Pi Zero catches all necessary interrupts. Each measurement sequentially reads all of the axes of the test magnetometer, then all of the axes of both of the reference magnetometers. Next, the Pi configures the ADC to measure temperature from both temperature measurement devices on MagEval. Therefore, there are eight ADC conversions for every full MagEval measurement, two each for three different test magnetometer axes and two more for the two temperature measurements. The reference magnetometer measurements take much less time than the ADC conversions. Therefore, we expect a minimal full sample period slightly more than 0.4 s (8 samples at 20 SPS). In practice, with the additional configuration steps and the reference magnetometer measurements we have observed a typical sample period of about 0.45 s.[4]

FVM Fluxgate Magnetometer Configuration The FVM Fluxgate Magnetometer is operated in remote continuous sample configuration, entered by pressing ALT+Remote after power up. In this configuration the magnetometer writes to its serial port a data string of format `'@-001388+043956-001019` 4 times per second. This data format corresponds to the X, Y, and Z axis magnetic measurements in nT at the magnetometer. This data string is always the same length and can be parsed by character position.

[4]The channel switching required for MagEval negatively affects effective sample rate performance. We learned this lesson from MagEval testing and have selected a simultaneous sampling ADC for the ASP Engineering Model (see Section A.2.1).

Results and Data Analysis

Several consecutive tests were used to measure each non-ideal property. In this section we describe each category of test performed and use the measured magnetic fields to estimate the error contributed by each non-ideal effect.

FVM400 Reference Noise This measurement uses only the FVM400 with the MagEval physically removed. This allows us to check the reference device operation and measure the noise floor in the room. We also analyze the consistency of the sample rate from the reference magnetometer. Figure 4-6 shows the sample period is consistent at just under 0.25 seconds, varying by about 10% peak-to-peak during the measurement. Figure 4-7 shows the three components of the reference field. The reference field X and Y components vary by a few tens of nT, but the Z component varies by a few hundred nT. The high Z-axis noise is likely interference from the Boston subway system as discussed in Appendix C. The quickly varying Z-field shows a maximum excursion rate of about $140\,\mathrm{nT\,s^{-1}}$. At an effective sample rate of 0.4 s, we expect the Z-axis variation to induce sample-to-sample error up to about 60 nT, though it may be less depending on our ability to synchronize the reference and test magnetometers to sub-sample accuracy.

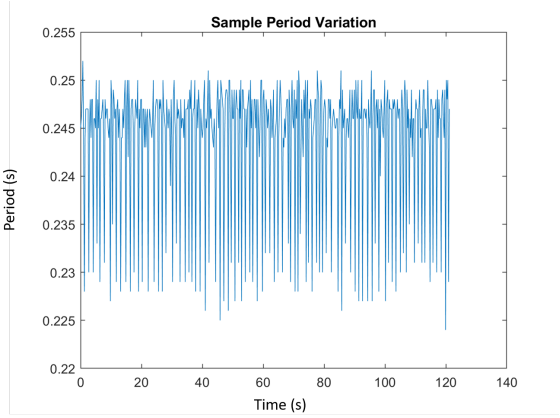

Figure 4-6: Sample period for the FMV400 reference magnetometer is relatively constant near 0.25 seconds.

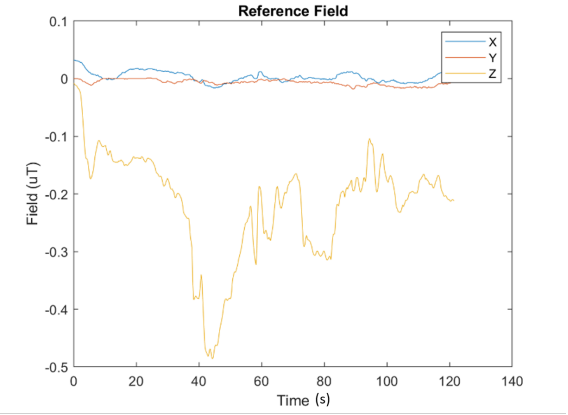

Figure 4-7: The ambient magnetic noise as measured by the reference magnetometer is low in X- and Y-axes, but relatively large in the Z-axis.

MagEval Magnetic Noise This measurement used only the MagEval board without the FVM400 reference magnetometer nearby. We show the sample variation measurement in Figure 4-8 to ensure that no samples are dropped. Additionally, we see that the board temperature varies by <0.1 °C over the measurement interval.

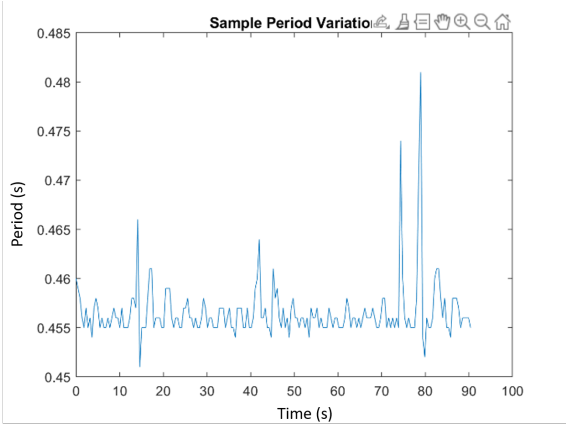

Figure 4-8: MagEval sample period is constant near 0.45 seconds.

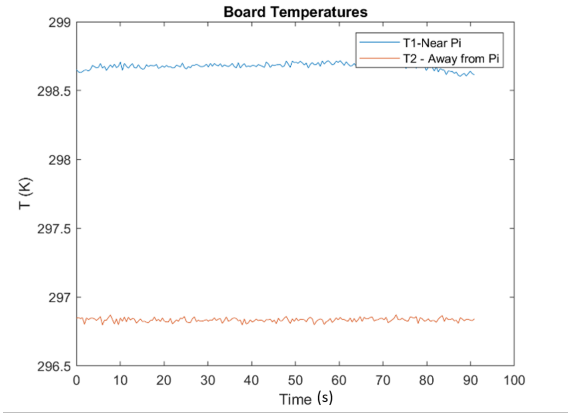

Figure 4-9: MagEval board temperature is relatively constant (<0.1 °C variation) when not deliberately perturbed.

Note that in all magnetic field plots in this chapter (see Figure 4-10 for an example) the magnetometer axes (X,Y,Z) are distinguished by color and the magnetometer source is distinguished by line style. We see magnetic field variation similar to that measured with the FV400 reference as in Figure 4-7, where the X- and Y-axes are relatively constant and the Z-axis shows more rapid long-term variation. The test magnetometer (HMC1053) does not have significant sample-to-sample variation like the RM3100 references show. We will not plot the RM3100 reference magnetometers in the rest of this section unless they are needed for the discussion. Finally, we plot the field just for the test magnetometer in Figure 4-11 to analyze the static field and noise.

We see P2P variation for the X-axis of <50 nT, similar to the FV400 reference magnetometer; the Y-axis appears noisier and the Z-axis shows significant environmental variation, similar to the FV400 measurement. We will align timestamps between the test magnetometer and the reference magnetometer for further measurements.

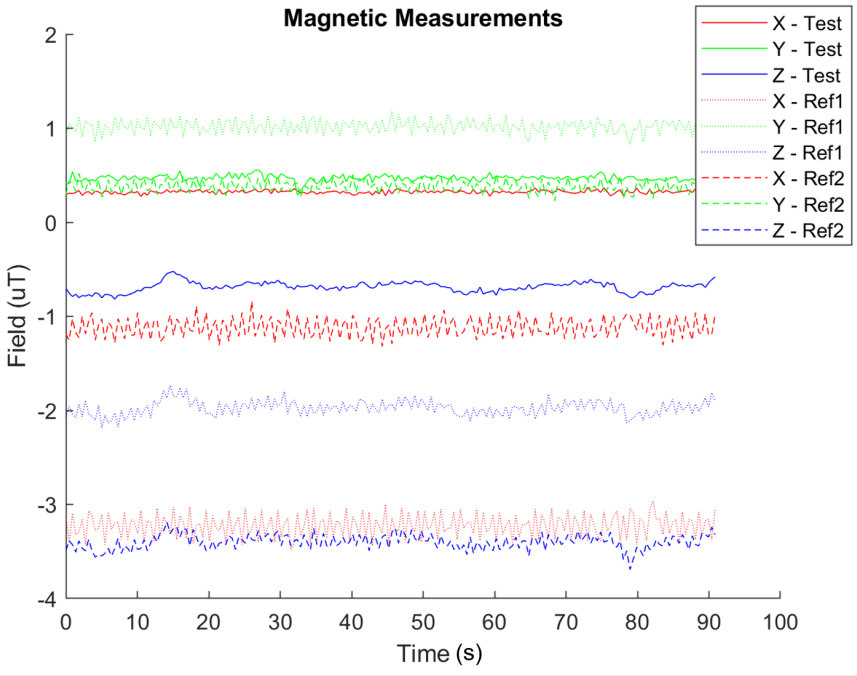

Figure 4-10: MagEval magnetic fields from all magnetometers plotted simultaneously. The test magnetometer ("Test") shows less high frequency noise than the RM3100 references ("Ref1" and "Ref2"), though both show the Z-axis long term variation observed in the FVM400 data (see Figure 4-7).

Simultaneous Magnetic Comparison In this test, the reference and test magnetometers are held near each other and operated at the same time to measure the static field offset. The observed fields are plotted in Figures 4-12 through 4-15. The static offsets are significantly larger than our measurement requirement (3 uT compared to 100 nT), but these can be calibrated out as described in Chapter 5. The rms difference between test and reference measurements with and without the static offset subtracted are provided in Table 4.2.

Table 4.2: Difference (delta) between reference and test measurements in frequency ranges of interest with and without the average offset subtracted. The noise floor of about 20 nT is expected from the analysis conducted in Section 4.4.1.

Axis	Average Delta [uT]	rms Delta-Offset [uT]
X	0.328	0.013
Y	0.034	0.024
Z	-0.467	0.018

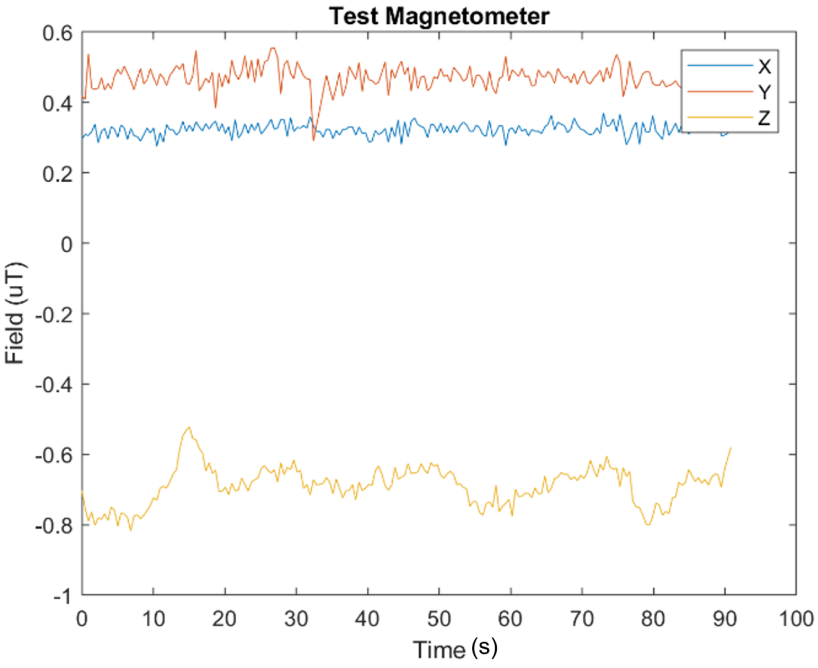

Figure 4-11: MagEval test magnetometer shows noise floor similar to FVM400 reference magnetometer. P2P variation in the X-axis is <50 nT.

Simultaneous Measurement Comparison with X-Field Applied In this experiment, the magnetometers were placed in a single-axis magnetic field generator (pictured in Figure 4-5) aligned with the X-axis. The alignment of the measurement device with the field generator was performed by eye and may only be accurate to within about 10°; however, this will only change the incident field on both the test and reference magnetometers in the same way. Therefore, any effects observed in the difference will be inherent to the measurement device and not the source of the magnetic field.

In Figure 4-16 we can see the sensitivity difference between the reference magnetometer and the test magnetometer. To calculate the magnitude of this effect, we read the maximum and minimum X-field strength values to find an appropriate linear scaling factor. We ignore the Y- and Z-axes for now; the cross-axis effects will analyzed separately and are reported in Section 4.4.2.

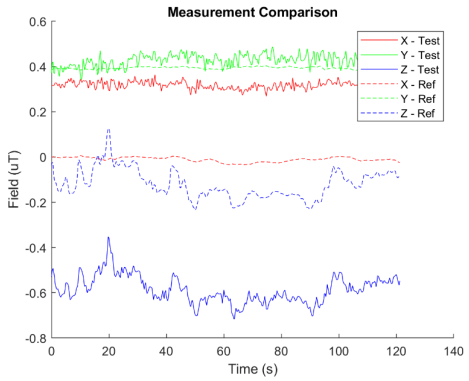

Figure 4-12: Measurement comparison between test and reference magnetometers.

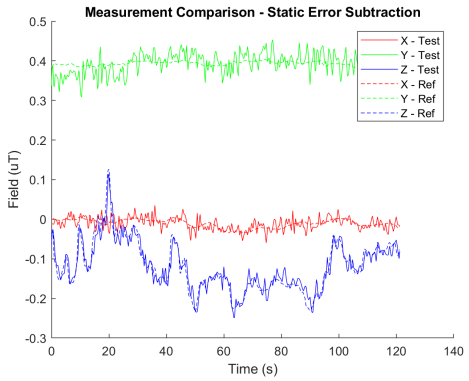

Figure 4-13: Measurement comparison with static offset subtracted.

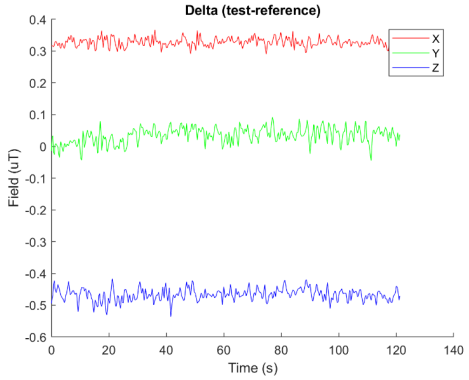

Figure 4-14: Difference (delta) between test and reference magnetometers.

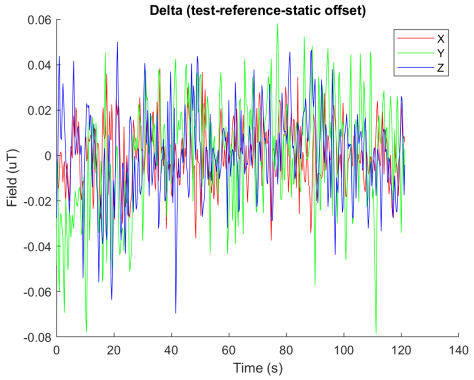

Figure 4-15: Difference (delta) between test to reference magnetometers with static offset subtracted.

Along the X-axis, the calibration coefficient is the same for the positive and negative values to 5 significant figures. We continue our data analysis with this coefficient applied. With both scaling factor and offset correction applied (as in Figure 4-18), we see good agreement between the test and reference magnetometers. We analyze the linearity and noise by removing any samples which are more than 0.1 uT away from the preceding or following sample; this eliminates glitches at the vertical portions of the stair step due to imperfect synchronization between the magnetometers. With this method, the rms error with the applied correction is 18 nT, no worse than when the field was static as summarized in Table 4.2. The flat profile of Figure 4-18 shows there is no observable non-linearity effect.

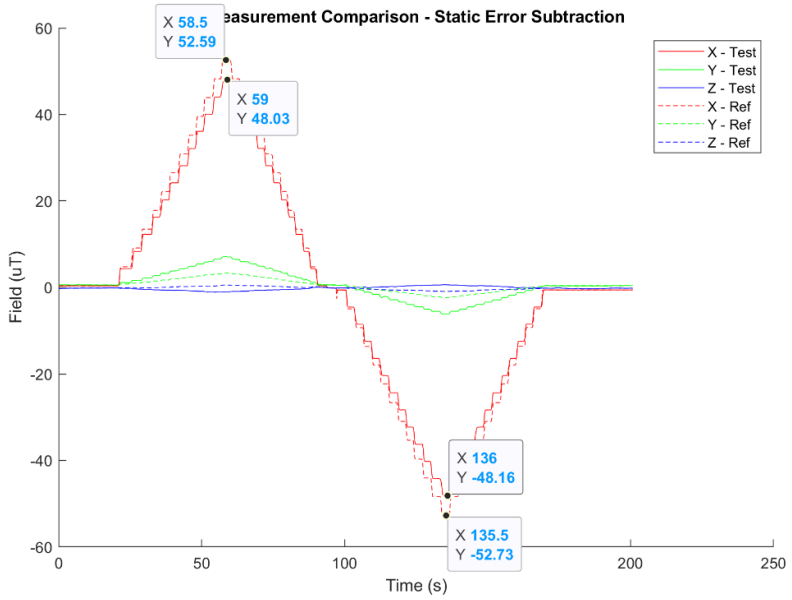

Figure 4-16: X-field comparison with static error subtracted.

Table 4.3: X-field sensitivity error coefficient calculation.

Direction	Ref-Peak [uT]	Test-Peak [uT]	Calibration Coefficient
+	52.59	48.03	1.0949
-	52.73	48.16	1.0949

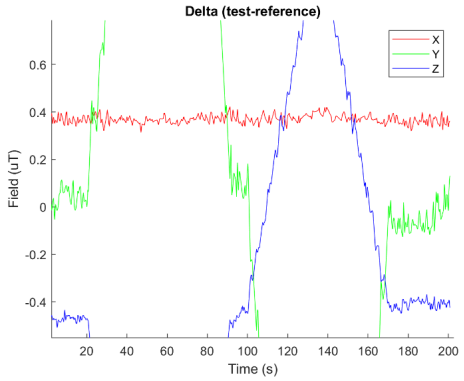

Figure 4-17: Difference in magnetic field measurement from test and reference magnetometer with X-field applied after scaling factor correction. Here we zoom in the vertical axis to focus on flatness of the X-measurement.

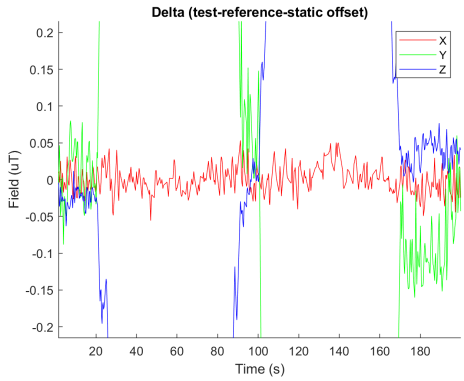

Figure 4-18: Difference in magnetic field measurement from test and reference magnetometer with X-field applied after both scaling factor and offset correction. The corrected X-measurement shows no residual features so non-linearity and hysteresis are not significant in this measurement range.

Simultaneous Measurement Comparison, Y-field Applied Here we use the same experiment and analysis technique as used to analyze the X-axis; this time applying the incident field along the Y-axis of both the test and reference magnetometers.

Table 4.4: Y-Field sensitivity error coefficient calculation.

Direction	Ref-Peak [uT]	Test-Peak [uT]	Calibration Coefficient
+	53.2	47.7	1.1153
-	65.25	58.26	1.1120

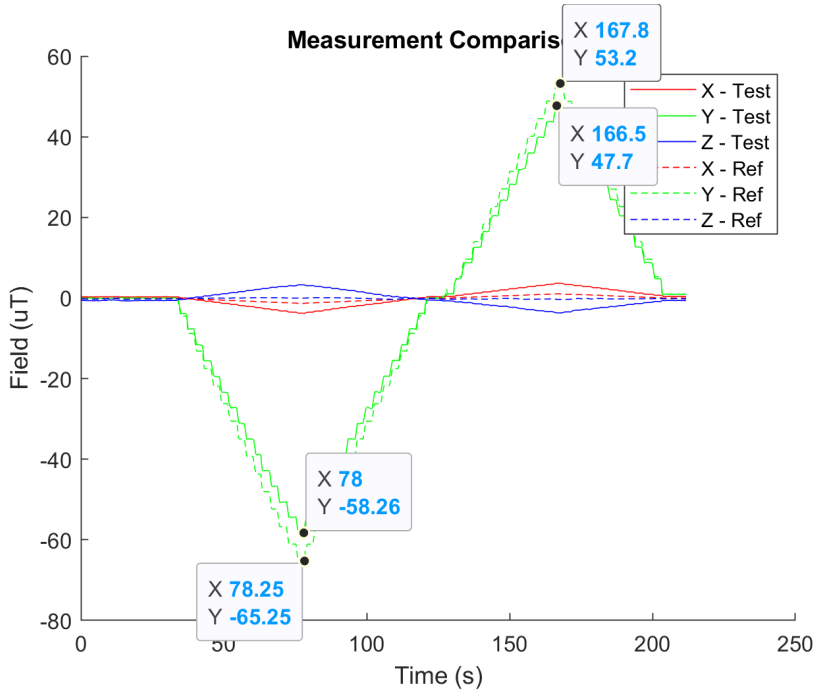

Figure 4-19: Y-field comparison with static error subtracted.

Along the Y-axis, the calibration coefficients are about 0.3% different for the positive and negative measurement (see Table 4.4). This may be due to the rounding of the positive coefficient field strengths or noise on the selected samples. However, a single value of 1.12 minimizes residuals. After calibration, the remaining Y-axis rms error is 76 nT, and like the X-axis, no nonlinearity is apparent with both the scaling and static offset corrections applied.

Simultaneous Measurement Comparison, Z-field Applied Here we use the same analysis applied to the X- and Y-axes previously to find the Z-axis calibration coefficients reported in Table 4.5. We again find somewhat different calibration coefficients, but a single calibration coefficient of 1.115 minimizes residuals. The rms error in the Z-axis with this sensitivity correction is 80 nT.

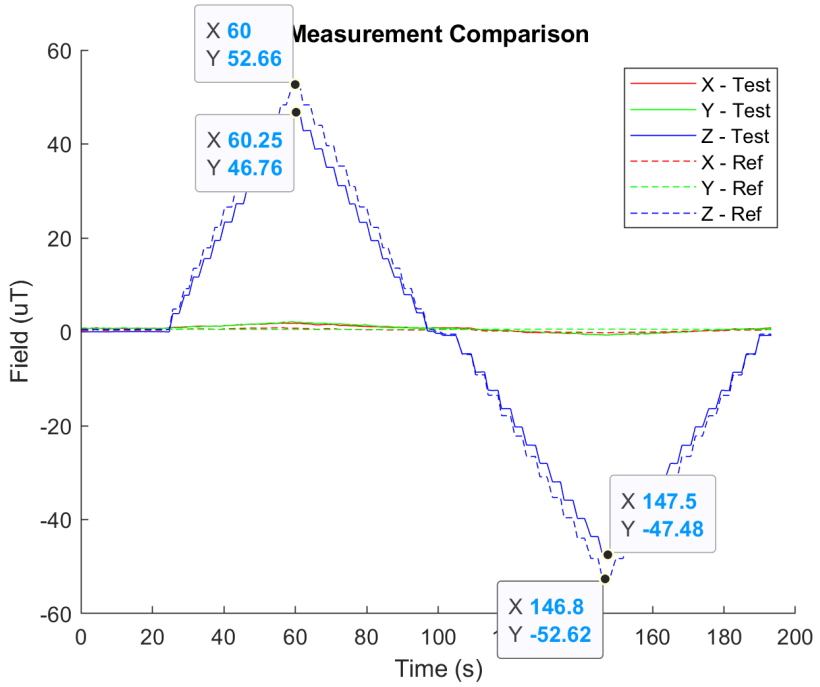

Figure 4-20: Z-field comparison with static error subtracted.

Table 4.5: Z-field sensitivity error estimation.

Direction	Ref-Peak [uT]	Test-Peak [uT]	Calibration Coefficient
+	52.66	46.76	1.1262
-	52.62	47.48	1.1083

Temperature Effects In this test, the test magnetometer was heated with a hot air gun to 81 °C (about 354 K) before being allowed to cool to room temperature. A static X-axis field was applied during this measurement to observe how the offset or sensitivity may change due to temperature. The magnetic field measurement during the temperature perturbation is shown in Figure 4-22.

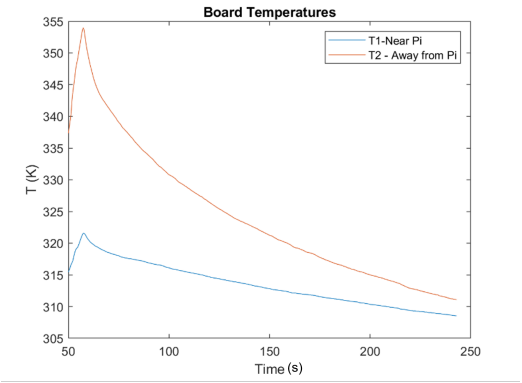

Figure 4-21: Board temperatures during temperature perturbation measurement. T1 is the temperature sensor near the magnetometers and is used for calibration. T2 is located near the Raspberry Pi. The magnetometer temperature peaks at about 81 °C (about 354 K).

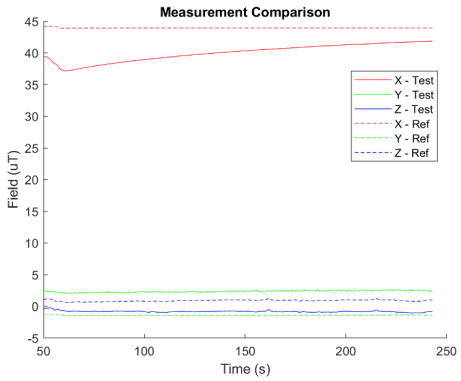

Figure 4-22: Magnetic field measurement variation during temperature perturbation despite constant incident magnetic field.

Table 4.6: Selected datapoints from temperature test showing magnetometer error over temperature variation.

Time	Temperature (T2) [K]	Delta [uT]
100	330.7	-1.038
125	325.4	-0.2704
175	317.8	0.7893
225	312.5	1.665

With a best linear fit, we find a temperature coefficient of 0.1472 uT/°C. Treating this as a temperature dependent sensitivity variation with the applied field of 43.94 uT finds a sensitivity coefficient of 0.335%/°C. We apply this linear sensitivity calibration and show the calibrated results in Figure 4-23. This basic calibration procedure is expanded to the full measurement equation in Chapter 5.

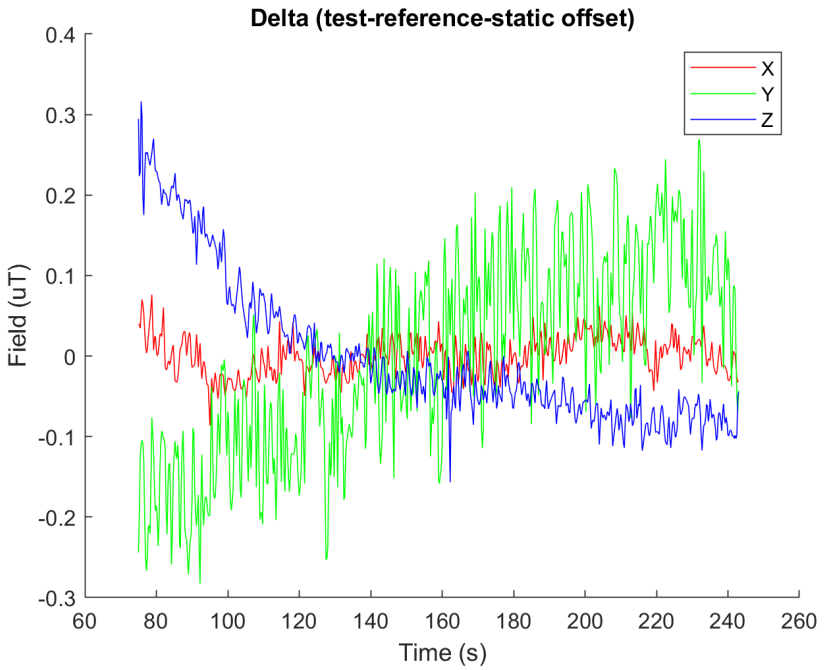

Figure 4-23: X-Axis variation over temperature is removed (to within 23 nTrms) by linear fit.

Hysteresis In this test we applied large field swings (>±100 uT) with a period of about 1 minute, and observed if the zero-field measurement changed depending on which field direction was most recently applied. For Figures 4-24 and 4-25, note that the reference magnetometer saturates at about 100 uT.

In Figures 4-24 and 4-25, we see that the difference between the test and reference magnetic field does not change much depending on if a positive or negative field has most recently been applied (0.39 ±0.03 uT) but that the amplitude measured by both devices does show hysteresis, or about 0.47 uT of remanence. This is likely due to some magnetization of metal present on MagEval (such as the header pins on the

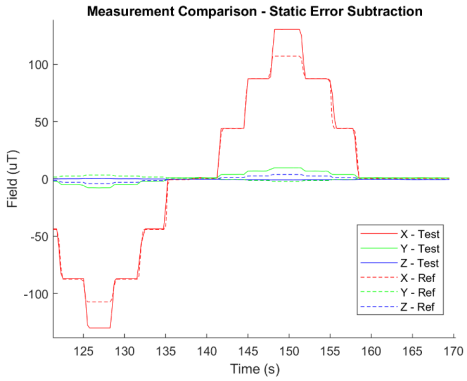

Figure 4-24: Hysteresis comparison with static offset subtracted. A large magnetic field is applied along the X-axis to screen for hysteresis effects.

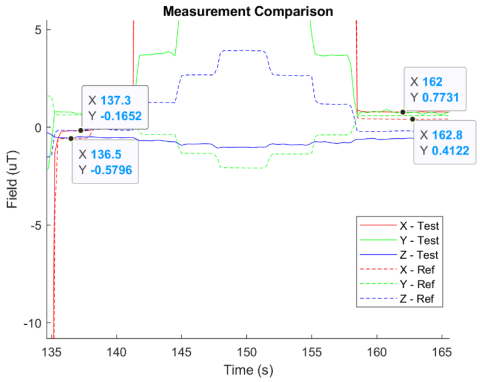

Figure 4-25: Hysteresis comparison zoomed in and labeled before and after large field application. Both the reference and test magnetometers show similar hysteresis effects, which indicates we are measuring an interference from nearby materials and that the hysteresis is not inherent to the test magnetometer itself.

RM3100 test board discussed in Section 2.5.2). Whatever the cause, it appears to affect the test and reference magnetometers equally so is not inherent to the magnetometer itself, and will not be a problem for the flight magnetometer implementation as long as the sensor package is kept free of magnetic materials (see Section 2.5.2).

Cross-Axis Coupling In this experiment we use the same data as collected for the X, Y, and Z axis sensitivity measurements, but instead look at the cross-axis effects. We expect some misalignment of the measurement axis with the coil since this was done by hand, but we do expect good alignment between the reference magnetometer and the test magnetometer (these are kept in fixed orientation with a 3D printed mount as described in A.2.1). With this alignment fixed, any misalignment cross-axis effects seen by the test magnetometer should also be seen by the reference magnetometer, and therefore no measurement difference would be created.

The remaining field differences in the cross-axes during the single axis experiments are as large as 4 uT, and therefore must be calibrated out (see for example Figure

4-18). We apply the calibration coefficients we have previously computed, but not the temperature calibration since that was not performed for all axes and the temperature during these measurements is relatively constant. Using the X-axis as an example: we can collect the cross-axis terms by simply looking at the peak-to-peak variation of the Y and Z field differences as a fraction of the X field peak-to-peak. We report all measured cross-axis terms in Table 4.7.

Table 4.7: Cross-axis coupling coefficients (with single-axis gain coefficients on the diagonal). This becomes the sensitivity matrix in Chapter 5.

Incident \ Affected	X	Y	Z
X	1.0949	0.0939	-0.0342
Y	0.0477	1.1200	-0.0703
Z	0.0165	0.0317	1.1150

Summary of Non-Ideal Properties Investigation

In this summary, we collect the relative error contribution of magnetometer noise, gain error, static offset, linearity error, temperature sensitivity, hysteresis, and cross-axes effects, and compare each contribution to our accuracy requirement. These can also be compared to the datasheet estimate in Figure 4-2. Where there are multiple instances of such a measurement (multiple axes for example) we report the worst-case value from the measurements. Each error contribution is compared to a "threshold" error, above which we will want to apply calibration. For Table 4.8 we define this threshold as 50 nT, leaving a factor of two margin for our 100 nT requirement.

Table 4.8: Summary of measured non-ideal properties and calibration demonstration.

Effect	**Value**	**%Threshold**	**Was Calibration Shown?**
Noise	24 nTrms[1]	50	NA
Gain[2]	5.86 uT	11,700	Yes
Static Offset	444 nT	1,780	Yes
Linearity	<10 nT	<25	No
Temperature Sensitivity[3]	10.9 uT	218,000	Yes
Hysteresis[4]	50 nT[5]	100	No
Cross-Axis	4.7 uT	9,400	Yes

[1] Not including the Y-axis noise which was notably higher in later measurements, possibly due to an accidental change in ADC operating parameters.
[2] At full-scale of ±50 uT range.
[3] Assuming a range of 50 °C.
[4] Over ±120 uT range.
[5] Likely will be reduced by designing with less interfering steel near magnetometer.

Second Order terms In Table 4.8 we reported each of the major interfering terms but did not consider the combination of multiple effects (e.g. how the static offset varies with temperature). We can estimate which second-order terms will be significant contributors by combining their fractional effect. For example, the static offset was 444 nT, and the temperature sensitivity can cause effects up to 20% of full-scale; therefore, we can expect that temperature variation of the offset may change by about 97 nT, and this should be calibrated out. Using this analysis, we estimate the maximum effect of the second order terms in Table 4.9. We ignore effects which were not significant even with only first order contributions.

Table 4.9: Second-order non-ideal effects.

Effect	**Static Offset**	**Gain**	**Temperature Sensitivity**	**Cross-Axis**
Static Offset	-	NA[1]	97 nT	NA[1]
Gain	-	-	1.3 uT	0.55 uT
Temperature Sensitivity	-	-	-	1.02 uT
Cross-Axis	-	-	-	-

[1] The static offset contribution has no applied-field dependence.

This page is intentionally left blank.

Chapter 5

Regression for Calibration and Interference Filtering

In Section 4.4.2 we evaluated the non-ideal properties of the HMC1053 for their expected impact on measurement repeatability. We summarize the findings of Section 4.4.2 by listing the properties which need to be calibrated, including necessary second order effects:

- Static offset
- Gain
- Linearity
- Cross-axis coupling
- Temperature dependence of gain
- Temperature dependence of offset
- Temperature dependence of cross-axis coupling

5.1 The Measurement Equation

In this section we will use the known non-ideal effects to write an equation that captures the expected mapping of the real incident field to the measured field with non-ideal effects included. The calibration model, which was constructed from the individual calibration steps described in Section 4.4.2, is given in Eq. (5.1), with terms

described in Table 5.1.

$$\vec{B_{act}} = \left[\mathbf{S} + \mathbf{K_S} * T\right] * \vec{B}_{meas} + \left[\vec{O} + \vec{K_O} * T\right] \tag{5.1}$$

Table 5.1: Terms in the measurement equation.

Term	Type	Description
$\vec{B_{act}}$	Vector	The real magnetic field at the measurement location
$\mathbf{S}$	Matrix	Sensitivity matrix scales the signal based on the real sensitivity of each axis and includes linear off-axis effects
$\mathbf{K_S}$	Matrix	The linear temperature dependence of each of the terms in the sensitivity matrix
T	Scalar	Temperature of the sensor
$\vec{B}_{meas}$	Vector	The raw three-axis measurement coming from the magnetometer
$\vec{O}$	Vector	Static offset value for each axis
$\vec{K_O}$	Vector	The temperature dependence of the static offset

5.1.1 Verification with Test Data

The predictive power of the calibration equation has been evaluated by applying the entire calibration model to all data collected in the determination of the non-ideal effects as described in Section 4.4.2. The results of this regression are provided in Table 5.2.

Table 5.2: Derived regression coefficients.

Axis	Sx	Sy	Sz	Ksz	Ksy	Ksz	Oz	Koz	RMSE
X	1.026	-0.163	-0.211	0.0032	0.0047	0.0080	-1.210	0.0360	0.0236
Y	-0.160	2.370	0.043	0.0027	-0.0520	-0.0028	-0.071	-0.0009	0.0593
Z	-0.086	0.096	1.214	0.0046	-0.0011	-0.0040	4.323	-0.1607	0.0332

The most important takeaway is that the magnetic field root mean square error for all axes is less than 60 nT, indicating we will meet the 100 nT precision requirement (as long as our collected data is adequately representative of the orbital magnetic environment). The observed error is approximately the environmental noise floor in this location; the calibration results may be better than observed but we do not have the facilities to test to a lower noise floor.[1]

The results are generally as we expected from the discussion of the non-ideal properties of the AMR sensors from Section 4.4.1. The diagonal components of the sensitivity matrix are near unity with the exception of Syy, which can be explained by looking at the sensitivity matrix temperature dependence. The data used in this regression used units of uT for magnetic fields and degrees Celsius for temperature. The Ksyy term is also anomalously large at -0.052 as compared to less than magnitude 0.01 for all other sensitivity terms. Most (but not all) measurements were taken at room temperature of approximately 25 degrees Celsius, and plugging T=25 into the Syy and Ksyy finds a room temperature Syy dependence of 1.07, approximately unity as expected. This shows a that lack of proper calibration data can cause anomalous fitting effects and we will need to be careful to properly capture a

[1]The measurements used to create Table 5.2 were made in a non-shielded room as described in Section 4.4.2.

wide range of calibration data on orbit. The offset values themselves and their own temperature dependence all fall within ranges predicted based on individual analysis as summarized in Table 4.8.

5.2 Extension to Interfering Sources

Here we describe how the measurement equation can be extended to included potential interfering sources, such as material and current-path interference effects.

5.2.1 Material Interference

The most significant magnetic interference will come from ferromagnetic materials (see Section 2.3). Many ferromagnetic materials can be categorized into primarily "hard" materials or "soft" materials based on how the material coercive force compares to the local magnetizing field (see Section 2.3.3). Here we use the magnetically soft and hard limiting approximations to show that the calibration equation which we have already derived can account for arbitrary spatial distributions of soft and hard materials without modification.

Magnetically Hard Interference

As discussed in Section 2.3.3, sources which are very magnetically hard (high coercivity and remanence) can be approximated as constant dipoles based on their constant magnetization state. The interference from any single constant dipole element can be written as in Eq. (5.2), taken from Eq. (2.1).

$$\vec{B}_{dipole} = \frac{\mu_0}{4\pi}\left[\frac{3\hat{r}(\vec{m}\cdot\hat{r}) - \vec{m}}{r^3}\right] \tag{5.2}$$

For constant moment m, and separation from the material in question to the measurement location r, it is apparent that the contribution to the magnetic measurement will be constant, and for the i'th interferer we can consider a B_i, which sums as in Eq. (5.3).

$$\vec{B}_{hard} = \sum_i \vec{B}_i \tag{5.3}$$

If we separately consider the "external" magnetic field with no interference (which is what we want to measure), we can write the following:

$$B_{ext} = B_{act} + B_{hard} \tag{5.4}$$

$$\vec{B_{ext}} = \left[\mathbf{S} + \mathbf{K_S} * T\right] * \vec{B}_{meas} + \left[\vec{O} + \vec{K_O} * T\right] + \vec{B}_{hard} \tag{5.5}$$

So to find $\vec{B_{ext}}$ in the presence of an unknown but constant $\vec{B}_{hard}$ we can use the same measurement equation as before (Eq. (5.1)) but with a different definition of $\vec{O}$ where we use prime to indicate instrument-only offset vector.

$$\vec{O} = \vec{O}' + \vec{B}_{hard} \tag{5.6}$$

Since the original (instrument-only) offset was also unknown prior to fitting, accounting for any number of static interferers requires no new unknown terms in the measurement equations.

Magnetically Soft Interference

For any magnetically soft interferer, the magnetic moment of the interferer can be calculated from the incident environmental field.

$$\vec{m}_i = (\mu_{r_i} - 1) * V_i * \frac{1}{\mu_0} * \vec{B_{env}} \tag{5.7}$$

$$\vec{B}_{soft_i} = \frac{1}{4\pi}\left[\frac{3\hat{r_i}(\chi_i V_i \vec{B_{env}} \cdot \hat{r_i}) - \chi_i V_i \vec{B_{env}}}{r_i^3}\right] \tag{5.8}$$

$$\vec{B}_{soft_i} = \left[\frac{\chi_i V_i 3}{4\pi r_i^3}\right]\left(\vec{B_{env}} \cdot \hat{r_i}\right) - \left[\frac{\chi_i V_i}{4\pi r_i^3}\right]\vec{B_{env}} \tag{5.9}$$

$$\vec{B}_{soft_i} = \left[\frac{\chi_i V_i}{4\pi r_i^3}\right]\left[3\hat{r_i}^T\hat{r_i} - \mathbb{1}\right]\vec{B_{env}} \tag{5.10}$$

Therefore, we can define a sensitivity matrix contribution from each magnetically soft interfering source.

$$\mathbf{S_{soft_i}} = \left[\frac{\chi_i V_i}{4\pi r_i^3}\right]\left[3\hat{r_i}^T\hat{r_i} - \mathbb{1}\right] \tag{5.11}$$

We represent the instrument intrinsic sensitivity matrix from before as $\mathbf{S'}$ and the new total sensitivity matrix can be defined.

$$\mathbf{S} = \mathbf{S'} + \sum_i \mathbf{S_{soft_i}} \tag{5.12}$$

The unknown interference and the unknown instrument sensitivity can be combined so that we do not need any more unknown parameters to fit the interference from the magnetically soft source. This is analogous to how magnetically hard interference was indistinguishable from the instrument-intrinsic offset.

Limitations and Assumptions

Our analysis above holds for materials which are completely magnetically hard (coercivity much larger than the environmental field) or completely magnetically soft (coercivity much lower than the environmental field). For materials with magnetic hardness in between these two limits, hysteresis effects will be present in the data which will make the calibration problem dependent on past events.

The treatment of the magnetically soft material also assumes that the change in magnetization, and therefore magnetic moment, is linear with the amplitude of the applied field. Given that the incident magnetic field will dominantly be the Earth's magnetic field with a relatively constant amplitude this is a reasonable assumption in our limited application.

5.2.2 Current Paths

The current paths on the spacecraft also produce interfering magnetic fields. The total magnetic field can be found for a known path and current with a path integral of the Biot-Savart law (originally used in Eq. (2.5)).

$$\mathbf{B} = \frac{\mu_0}{4\pi} \int_C \frac{I\mathbf{dl} \times \mathbf{r}'}{|r'|^2} \tag{5.13}$$

The current magnitude I can be removed from the integral as it is constant over the path. The solution to this integral is not known without knowing the path, but we do know that the integral is constant.

$$\vec{B}_{current} = \vec{D}I \tag{5.14}$$

Where we have introduced the "dependency vector" $\vec{D}$ which is the solution to the path integral in the Biot-Savart law. For multiple interfering current paths (indexed by i) we can write the sum in Eq. (5.15).

$$\vec{B}_{current} = \sum_i \vec{D}_i I_i \tag{5.15}$$

The actual environmental field can be calculated from the measured field given this interfering field (or vice versa).

$$\vec{B_{act}} = \vec{B_{env}} + \vec{B}_{current} \tag{5.16}$$

$$\vec{B_{env}} = \vec{B_{act}} - \vec{B}_{current} \tag{5.17}$$

These results can be combined with the main measurement equation, Eq. (5.1), to create Eq. (5.18). This is the measurement equation extended to included current path interference sources. The sum over interfering current sources can be performed over as many current sources are available to measure, such as those in the spacecraft housekeeping telemetry data products.

$$\vec{B_{act}} = \left[\mathbf{S} + \mathbf{K_S} * T\right] * \vec{B_{meas}} + \left[\vec{O} + \vec{K_O} * T\right] - \sum_i \vec{D_i} I_i \tag{5.18}$$

5.3 Implementation

The measurement equation represents all the complexity of the measurement device and interference sources (at least to a level that meets performance requirements as shown in Table 5.2). To actually implement the calibration we also need to load data from spacecraft instruments, to be able to differentiate from measurement and calibration data sets, and to be able to perform the minimization with the calibration datasets to determine the unknowns in the measurement equation. We have implemented these functions in Python3 in three main modules: a calibration module, a magnetic measurement class, and a file loader.[2]

- **Calibration**: This module contains a Python class which implements the measurement equation and stores the unknown measurement equation parameters as class variables. This also provides functions which will apply the derived measurement equation to new data, and will also perform least squares minimization to find its best fit parameters.
- **Mag Measurement**: This module defines the Measurement class. The class values are all the measured terms in the measurement equation. The class provides functions which help to populate the data in a consistent format.
- **File Loader**: This module contains a list of functions which will load data from files and properly format the data in the measurement module class structure. These functions are generally called by the user or by a short user-written program. Each function in this module maps one-to-one with a method of generating and storing data, such as each of the test hardware devices described in Appendix A.
- **User Script**: This file is written by the user and is only a few lines long. This

[2]The software is hosted on STARLab's Enterprise GitHub (`AEROVISTA_ASP/GroundTools/cal_software/`).

contains information like the file path for the data and which data products are to be plotted and saved.

5.3.1 Calibration Class

The calibration class contains a numpy array for every unknown parameter in the matrix measurement equation. The calibration class also contains a variable called `useFlags` which indicates which unknown variables are actually used in the calibration. By defining different elements in this python dictionary to be Boolean True or False, the user can mask the effects of different unknown terms in the measurement equation. This is useful when testing with hardware which may not generate all of the data required for the full measurement equation. For example, the RM3100 magnetometers in the magEval board do not have any associated temperature data, and without an external interfering source, there will be no current sources to calibrate against. The calibration object stores this information as a flag to properly implement the desired calibration during regression and application, and also to document the data used to generate the calibration object. With this flag stored as a class parameter, the user knows which data should be provided if this calibration object is going to be used again to apply to new data.

The application of the calibration object to new data is achieved by implementing the measurement equation using numpy array math. The minimization of the error using calibration data uses the numpy `least_squares` function. This function minimizes the output of an error function, and this error function is defined as the difference between the calibrated data and the reference data at every measurement point. To provide the most robust minimization, every axis is minimized independently. The least_squares library expects and returns a simple list of coefficients so the Calibration class also provides functions help format the calibration parameters into this simple list. One function packs the class parameters into the list so that the minimization can be started with the default coefficients. Another function updates the class values based on a list which is returned from the minimization routine.

5.3.2 Measurement Class

The measurement class stores measurement data in a standard format. This allows the calibration class to be written without regard to the original format of the raw data from the instrument. The calibration class assumes that all data is sampled on the same time base and that all necessary data is populated into the measurement objects. The measurement class itself implements functions which make it easier to properly format the data from a variety of hardware sources. The main class variables of the measurement class are time, magnetometer, temperature, and interfering current source data. This class implements interpolation so that each variable, as stored by the class objects, will be sampled on the same time base. There is also a class list that keeps track of the names of all the current path data which is stored in the current paths data array. Finally, there is a simple string text description in the class object to document the source of the data, which is filled in manually by the user. The general procedure for populating the measurement class is as follows:

1. Load time stamps from file, and add these to the class object.
2. Load magnetometer data and associated time stamps, add to measurement class calling function for time interpolation.
3. Load temperature data and associated time stamps, add to measurement class calling function for time interpolation.
4. Load interferer data and associated time stamps, add to measurement class calling function for time interpolation.

5.3.3 File Loader

This module stores functions that load data from file locations. This software maps one-to-one with instrument programs which store data to files. These files will return a measurement class object which is properly formatted with the available data. The user can then use the returned measurement class objects (data magnetometer, and optionally reference data), and call the calibration class objects to create the calibration object or apply the calibration data. Any future use for the calibration

method described in this work should be able to use this software with whatever data format is available by only adding a new file loading function to the file loader module.

5.4 Considerations for System Integration

The calibration method we have described is performed exclusively on the ground. This is advantageous because the relative complexity of the calibration software does not need to be verified to flight standards, and the user can easily modify parameters and source data to achieve the best results. However, collecting all the system data needed to run the proposed calibration does impose some requirements on the mission and the rest of the spacecraft system.

First, to filter out the interference caused by spacecraft current paths, the magnetometer ground processing software must be provided with accurate measures of the current flowing through the spacecraft. This data is usually collected anyway as part of the spacecraft's housekeeping or health and status telemetry sets. This data is collected on AERO-VISTA at a rate of 10 Hz. As long as the current does not change significantly during the measurement period, this rate should be sufficiently high. Very high frequency variations (on the order of 100s of Hz or above) will be filtered by the analog low pass filters in the magnetic sensor. Additionally, the housekeeping data must be synchronized with the magnetometer data to at least better than a measurement period (approximately 20 ms). This is already achieved on AERO-VISTA as all data must be time stamped with 1 ms accuracy.

Finally, we need a source for calibration data. We expect to perform calibration on orbit for AERO-VISTA by collecting magnetometer data at low latitudes. At these low latitudes the magnetic field predicted by models such as the World Magnetic Map (WMM) is accurate to approximately 150 nT [8]. This accuracy is above our measurement requirement, but since we require *precision* of $<$100 nT, not absolute accuracy, these models should be sufficient for determination of calibration parameters. To extract the WMM prediction of the magnetic field as seen in the spacecraft's

body frame we will use global position information from a combination of GPS and orbital ephemeris data. The WMM provides magnetic field data with respect to an Earth centered Earth fixed (ECEF) coordinate system. This can be rotated into the spacecraft's coordinate system with data from the spacecraft ADCS telemetry. This is reported with respect to an Earth centered inertial (ECI) coordinate system, so we will additionally need to rotate the ECEF magnetic vector into an ECI magnetic vector using the absolute time stamp of the measurement.

AERO-VISTA generally is not running science observations with the main vector sensor at low altitudes, so the magnetometer sensor will be separately turned on at low latitudes to capture calibration data. We expect to capture 500 seconds of calibration data so that the data-take parameters are the same for calibration as they are for science data measurement.

Chapter 6

Ground Testing for Resource Constrained Missions

Access to magnetic testing facilities can be limited on CubeSat projects. Some reasons include: the equipment or facility is expensive, it is difficult to schedule, the spacecraft or instrument is being used for other development, integration, and test activities, or otherwise cannot be brought to a dedicated magnetic measurement facility. We perform measurements in the lab to verify the instruments developed for AERO-VISTA, and also have used ground measurements for screening components and subsystems which may significantly contribute to the magnetic field around the spacecraft. The use of these measurements in system budgeting is discussed in Chapter 3.

6.1 Environmental Considerations

When making ground measurements for magnetic characterization, we are looking for a magnetic perturbation caused by some known change (e.g. introduction of a magnetic object, turning on of an interfering system etc.). This signal exists on top of magnetic noise which is inherent to the measurement device and the environment. In the human environment, many sources can interfere with the natural magnetic field created by the Earth, such as power flowing through power lines and the movement of large magnetized steel objects such as cars. Some projects minimize these effects

by travelling to remote sites for magnetic measurement. Others may choose to make measurements in a magnetically shielded room; one in which the walls are made of one or more layers of highly magnetically permeable mu-metal (like we did in Section 7.7). We have found that the urban environment around Boston is too magnetically noisy for measurement down to our desired noise floor below 100 nT. However, some screening measurements can be made if the magnitude of the expected perturbation at the measurement location is larger than about 1 uT.

We believe Boston's subway system to be the largest interference source near MIT's campus. The currents in the subway system generally flow in the plane of the surface of the Earth, so less magnetic noise is observed in directions along the surface of the Earth compared to the up-down axis, so measurements perpendicular to the up-down axis are preferred for lower noise measurements. Travelling even just a few miles to get away from the subway system improves the magnetic measurement environment. The more immediate proximity of heavy machinery (e.g. large movable radio dishes) also appears to be at least as significant as the general urban density around the measurement location. Measurements made near large equipment even at remote radio astronomy facilities show more magnetic noise than suburban areas without heavy equipment nearby. See Appendix C for detailed environmental noise screening methods and results.

6.2 Measurement for Magnetometer Verification and Calibration

Verifying that the magnetometer produces results with the necessary accuracy or repeatability requires knowing the magnetic field at the measurement location. On large missions this may be accomplished by using magnetic shielding together with a series of nested Helmholtz cages to produce a precisely known and static magnetic field [67]. While we had access to a Helmholtz cage in MIT's Space Systems Laboratory [68] (see Section A.1.1 for more information), this Helmholtz cage is not paired with any

magnetic shielding so the field is still subject to environmental variation of the urban environment. This makes the Helmholtz cage a poor test platform both for noise floor measurements and for accuracy over range of incident field measurements.

Instead, we have used the relative stability of Earth's magnetic field in a quiet location to apply varying magnetic field incidences to verify the performance of the magnetometer over a range of incident fields. We find the "known" magnetic field at the measurement location by placing another magnetometer (the "reference magnetometer") near to the magnetometer under test (the "test magnetometer"). The magnetic measurement from the reference magnetometer can be used as the known good magnetic field value at the location of the test magnetometer as long as the following conditions are met:

- The precision of the reference magnetometer is at least as good as the desired precision level (nominally 100 nT for AERO-VISTA).
- Temporal variation of the magnetic field between the samplings of each magnetometer is at or below the desired precision level.
- Spatial variation of the magnetic field between the two magnetometers is at or below the desired precision level.
- The magnetic field caused by each of the magnetometers (or its supporting equipment) at the location of the other magnetometer is at or below the desired precision level.

We used this technique with coil magnetic field generators to produce the data used in Section 4.4.2. We also used this technique to test the spacecraft magnetic field production in Section 6.3.

6.3 Current Path Self-Interference Measurement

6.3.1 Test Setup

In this experiment we determine if the the entire spacecraft bus is going to produce magnetic errors in our measurement.[1] We use the RM3100 magnetometer on the Helmholtz cage electronics (see Section A.1.1) to observe how the magnetic field changes at the location of magnetometers in the spacecraft (see Figure 3-1). We observe the magnetic fields while the spacecraft bus performs activities including magnetorquer firing.

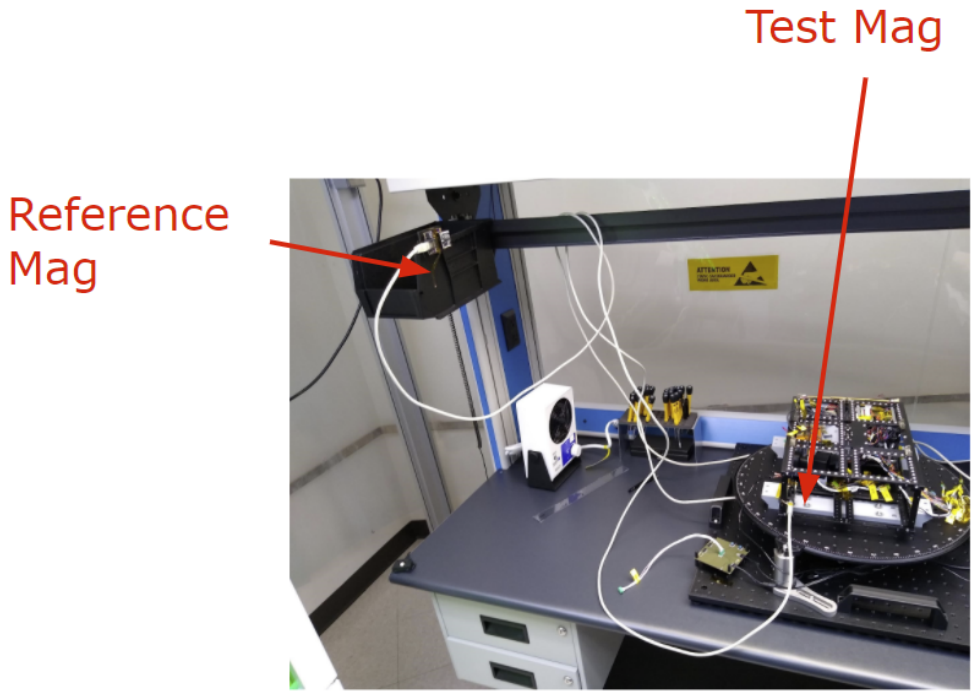

Figure 6-1: Testing the magnetic field produced by the spacecraft bus during operation. The reference magnetometer samples the local magnetic field to subtract large-scale environmental variation. The test magnetometer is placed in the same physical location the magnetometer instrument will occupy.

[1]This experiment was conducted in the Haystack Westford facility, though the magnetic noise at the time of this measurement was less than seen in the measurement of the same location in Appendix C.

6.3.2 Measurement Results

The magnetic field difference with static offset subtracted between the test and reference magnetometers is plotted in Figure 6-2. The deviation between the two magnetometers during these operations is [16, 23, 12] nTrms, approximately the gradient noise floor in this location.[2] This shows that the spacecraft bus activities do not produce a magnetic field which will interfere with our magnetic measurement (as long as the magnetorquers are not firing). Additionally, the lack of hysteresis between positive and negative magnetorquer firings shows that there is no material in the spacecraft which becomes noticeably magnetized by the magnetorquers.

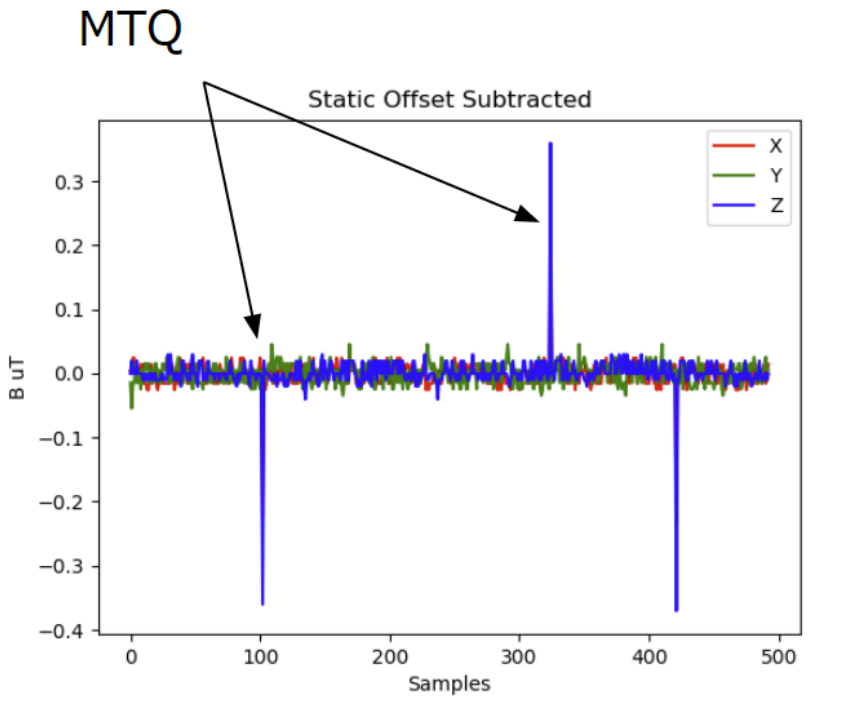

Figure 6-2: Measurement results of spacecraft bus magnetic screening. The only observable features are the magnetorquer firings. No hysteresis is seen before/after magnetorquer firing.

[2]Haystack laboratory space as measured in Appendix C.

6.4 Using Smart Phones as Magnetometers

One magnetometer which is easily accessible to most people can be found in personal smart phones. The magnetometer is generally a 3-axis sensor, and its readings can be plotted in real time or saved to files such as `.csv` for later processing.[3]

6.4.1 Phone Magnetometer Performance

The quality of any measurement depends on the precision and accuracy of the phone's magnetometer. Here we evaluate the noise floor performance of a smart phone magnetometer using the techniques described in Section 6.2. The results presented here are all from the author's personal cell phone[4] so may not be applicable to all other makes and models. If greater certainty of magnetic measurement is required, the reader is encouraged to follow the steps outlined here to verify the performance of their own cell phone. Alternatively, one could use a less-integrated but still inexpensive magnetometer such as the author's implementation of the PNI RM3100 discussed in Appendix A.

The noise floor is measured in a location with an environmental noise floor below 20 nTrms in all axes from 0.1 to 10 Hz.[5] The measurements made by the phone magnetometer is plotted and analyzed in Figure 6-3. The phone measurement shows that uncertainty during this acquisition is dominated by a slow drift with time. Filtered from DC to 10 Hz, the measurement over 1 minute shows an rms variation in the 3 axes of [108, 533, 354] nTrms. When bandpass filtered from 0.1 Hz to 10 Hz to remove the slow drift, the variation is [60, 75, 111] nTrms, approximately a 3 times improvement on average compared to the measurement down to DC. The phone magnetometer noise is about 5 times worse than either the RM3100 or our implementation of the HMC1053, though with the low frequency drift included, the

[3]There are several such apps available but this author uses the "Physics Toolbox Magnetometer" app by Vieyra Software which can be found on both the Apple App Store and the Google Play Store.

[4]A Motorola Moto G7 Power purchased in 2019

[5]Location lat-long: (42.416939, -71.473886). See Appendix C for environmental noise screening methods.

precision is closer to 20x worse than the other options.

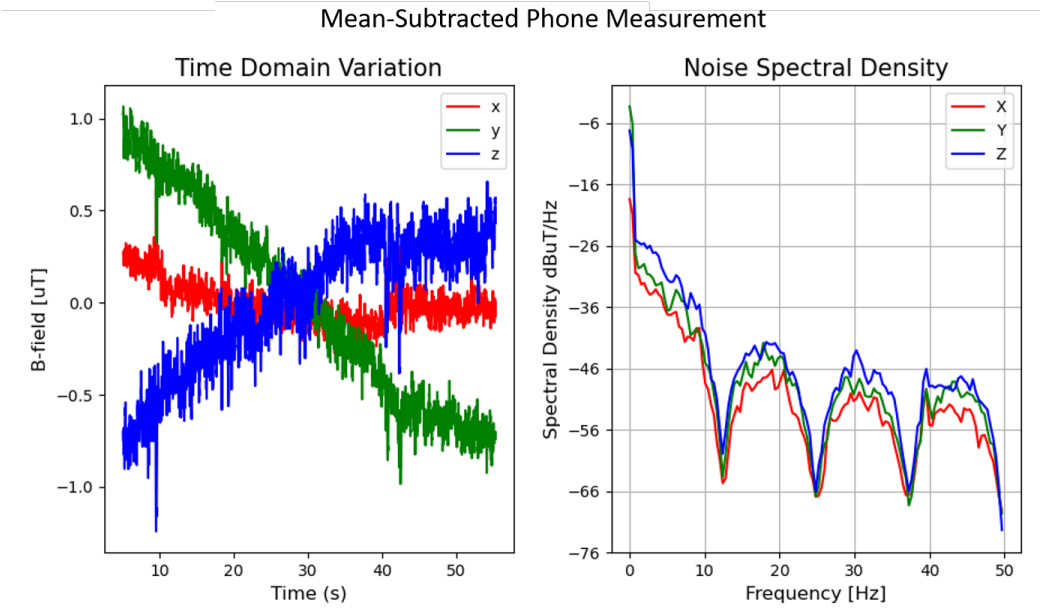

Figure 6-3: Measurement with phone magnetometer in low-noise location. The average (constant) value in each axis has been subtracted to see the variation with time and noise.

6.4.2 Preparing for Phone Magnetometer Measurements

Accurate estimation of dipole moment or other multipole moments requires knowing both the measured field strength, and the distance between the source and measurement. Magnetic signatures from CubeSat components are often only detectable at short distances, so it is important to know the location of the magnetometer within the phone to at least a few cm. This can be easily determined by using a magnetic object (a screw or any other piece of steel attracted to a magnet will suffice) and an app which continuously plots the magnetic field. The location of the magnetometer can be found by moving the magnetic object across the face of the cellphone in a search pattern and looking for maximal magnetic deflection in the plotted fields. The location where the object creates a maximal deflection in the measured field is the location closest to the magnetometer inside the phone. While this doesn't help us know where the magnetometer is along the axis perpendicular to the screen, modern

cell phones are so thin that this doesn't add much position uncertainty.

6.5 Materials Screening

6.5.1 Magnetization State

To measure the magnetization state of any object, we simply need to measure the field at a fixed location with and without the object present. This can be easily accomplished with a phone magnetometer and a non-magnetic object of known thickness (such as a book). By sliding the object in question across the magnetometer location in the cellphone with the spacer in between, the object will create a deviation in local magnetic field whose amplitude can be read off the graph. Then by using a dipole approximation or other geometric simplification, we can compute the dipole moment of the object. If desired this can be converted into a material magnetization by dividing by the object's volume.

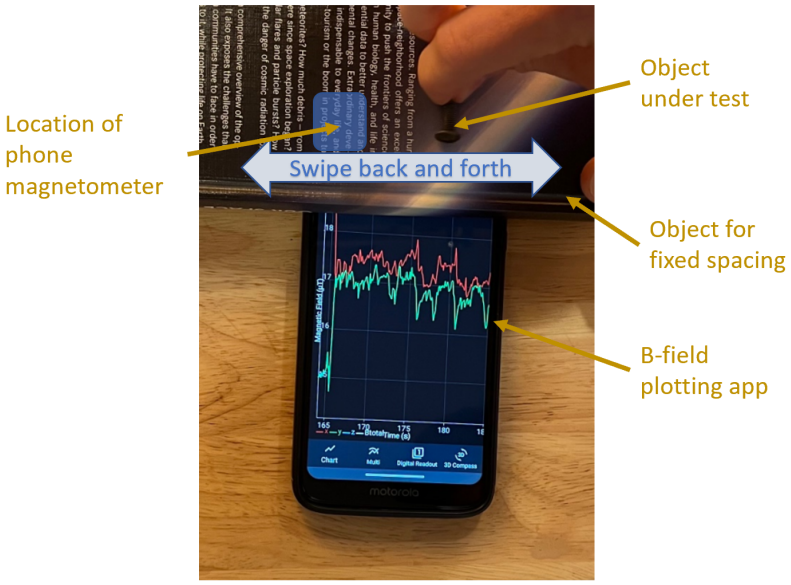

Figure 6-4: Procedure for estimating magnetization of the object.

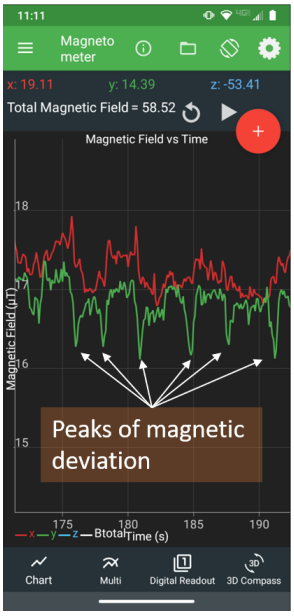

Figure 6-5: Screenshot showing magnetic perturbations caused by the presence of the screw at closest approach.

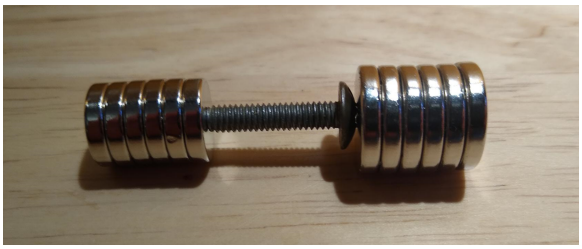

Figure 6-6: Using neodymium magnets to magnetize an object of unknown material.

Example Application We can demonstrate this procedure using a randomly selected 10-32 3/4 inch screw. We use a textbook [25] approximately 21 mm thick to create a constant space between the magnetometer and the screw. Using the center of the phone's thickness as the magnetometer location, we estimate the magnetic measurement location to screw center-of-mass distance is 28 mm at closest approach. The magnitude of the magnetic perturbation read off the screenshot in Figure 6-5 is about 1 uT. In the dipole approximation we can solve Eq. (2.3) to find an estimated moment of $1.1 \times 10^{-4}\,\mathrm{Am}^2$. This could then be used with Eq. (2.3) to estimate the object's magnetic field at other locations, such as the spacecraft magnetometer.

6.5.2 Remagnetization Properties

Maximum Magnetization (Remanence)

If the material might be magnetized by a strong field during ground handling or in space, it is good to know how much magnetization that material might retain in the worst case. Inexpensive neodymium magnets can create surface fields of thousands of Gauss [69] and can be used to magnetize an object such as the screw depicted in Figure 6-6. After magnetization, we ran the same dipole approximation screening from Section 6.5.1 and found a perturbing magnetic field of about 10 uT at the same distance, indicating this material can retain a magnetization about 10x larger (and correspondingly larger dipole moment) than what it had when we picked it up in the lab.[6]

[6]When measured one week later, the screw's magnetization had not noticeably decayed.

Magnetic Hardness

As discussed in Section 5.2.1, we can calibrate out magnetization effects for objects that are very magnetically hard or soft. If we don't know the magnetic hardness of the material from material estimation, we can measure the remagnetization properties by applying a remagnetizing field in positive and negative polarity and looking for hysteresis. One way to apply this known field is to use neodymium magnets. Any combination of magnets can be stuck together into one single magnet so the combined magnet is strong enough to produce a field of the desired strength from a reasonable distance away (several centimeters is sufficient for small objects). We rotate the magnets back and forth near the phone magnetometer looking for a distance where the incident field is the desired magnitude. For example, we might want to know if we will observe hysteresis effects with Earth's field magnetizing our objects, so we look for a distance which creates an approximately 100 uT peak-to-peak signal. Then to measure hysteresis effects in the object we apply the following procedure:

1. Attach the test object very near the magnetometer for maximum signal.

2. Bring the magnet in from far away (multiple meters) to the measured distance so that the object (and magnetometer) receive the desired magnetizing field.

3. Remove the magnet to very far away so the magnetometer can settle to a value caused only by the object and the environmental background.

4. Bring the magnet back, but this time facing the opposite direction to magnetize the object in the opposite direction.

5. Remove the magnet to a large distance so it does not appear in the measurement.

Now, the magnetization of the material after the negative and positive induced fields can be compared to look for any hysteresis effects in the material. The experimental setup and observed curves are shown in Figures 6-7 and 6-8.

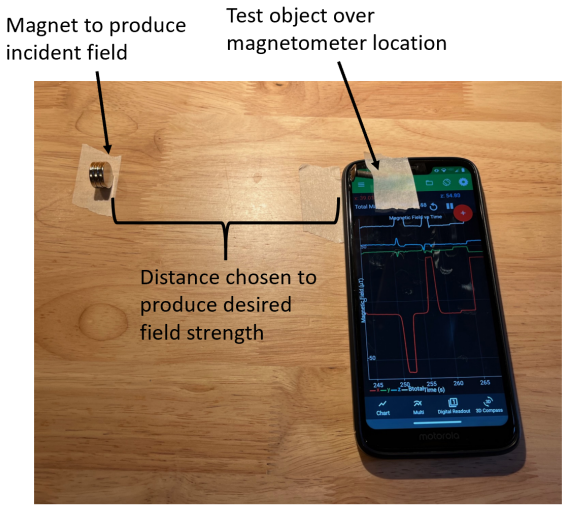

Figure 6-7: Test setup for determining magnetic hardness.

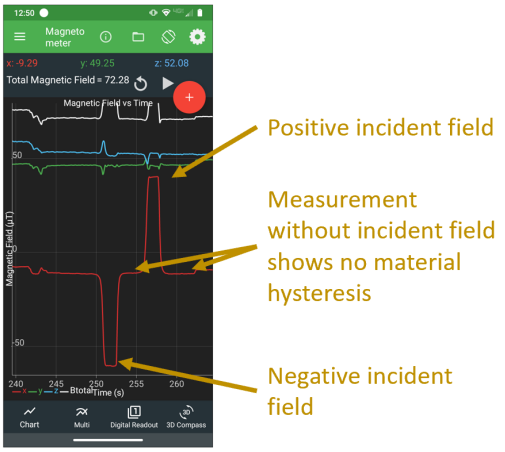

Figure 6-8: Screenshot showing magnetic measurements during material hysteresis screening.

6.5.3 Dimensionality Arguments for Improved Measurements

Objects may exhibit different dimensionality over different distances. Untuitively, any object "looks like a point" from far away, but some objects "look" more like other simple geometries (e.g. a line) when observed at a closer distance. This change of approximate geometry can be used to measure magnetization of large objects where application of the dipole approximation would require the measurement to be so far away that we can't extract the signal from the noise.

One such object screened for use on AERO-VISTA is the long thin linear spring shown in Figure 6-9. This spring is almost 29 cm long and creates no measurable field at distances beyond about 25 cm, so the dipole approximation is a poor fit for this geometry. Instead, we can approximate this spring as a finite straight line with constant linear density of dipole moment λ. Then the differential moment can be integrated over the object's length to find the expected mapping of linear moment density to magnetic field at a given measurement location.

For example, if we magnetize the spring perpendicular to its long axis (call this the X-direction) and measure the field at a place on the perpendicular bisecting plane and along the X-axis (see Figure 6-10), then the field can be calculated as derived in equations (6.1) through (6.4).

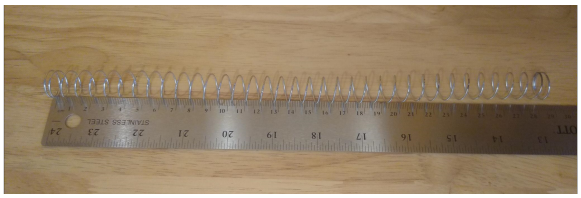

Figure 6-9: This long spring was considered for a deployment mechanism on AERO-VISTA. It is long enough that it is easier to make the magnetization estimate with an infinite line approximation than with a dipole approximation.

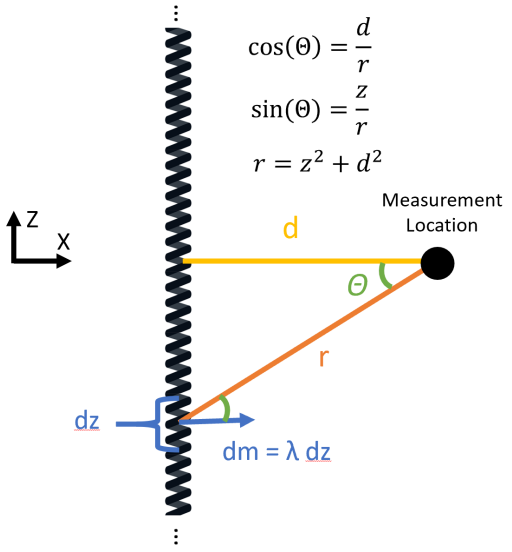

Figure 6-10: Diagram for calculation of magnetic field from a long thing line of constant linear dipole moment.

$$\vec{B} = \frac{\mu_0}{4\pi}\Big[\frac{3\hat{r}(\vec{m}\cdot\hat{r}) - \vec{m}}{r^3}\Big] \tag{6.1}$$

$$d\vec{B} = \frac{\mu_0\ dm}{4\pi r^3}\Big[3(cos(\theta)\hat{x} + sin(\theta)\hat{z})cos(\theta) - \hat{x}\Big] \tag{6.2}$$

$$d\vec{B} = \frac{\mu_0\lambda\ dz}{4\pi r^4}\Big[\hat{x}\big(\frac{3d^2}{(d^2+z^2)^{5/2}} - \frac{1}{(d^2+z^2)^{3/2}}\big) + \hat{z}\big(\frac{d*z}{(d^2+z^2)^{5/2}}\big)\Big] \tag{6.3}$$

Integrating z from $-\infty$ to ∞ for the infinite line approximation finds Eq. (6.4).

$$\vec{B} = \hat{x}\frac{\mu_0\lambda}{2\pi d^2} \tag{6.4}$$

Using the same screening method as in Section 6.5.1, we get a 4 uT perturbation at a measurement distance of 8 centimeters [38]. Solving Eq. (6.4) with this distance finds a linear moment density of $\lambda = 0.09\,\mathrm{Am}^2/\mathrm{m}$.

With the known length of 0.29 meters, we can estimate the total dipole moment of this spring to be $0.026\,\mathrm{Am}^2$. This is a large interfering dipole, particularly if it is close to the magnetometers. For this and other reasons, another spring option was eventually selected for use on AERO-VISTA.

Dimensionality Simulation Justification

We can quantify this intuition about "looking infinitely long" or "looking like a point" by simulating a finite line of moment (here with unit length, though the argument scales to any length) and comparing to the infinite line and dipole approximations (see Appendix B for simulation details). Here the line is simulated as 1 meter long with dipole density 0.01 Am.

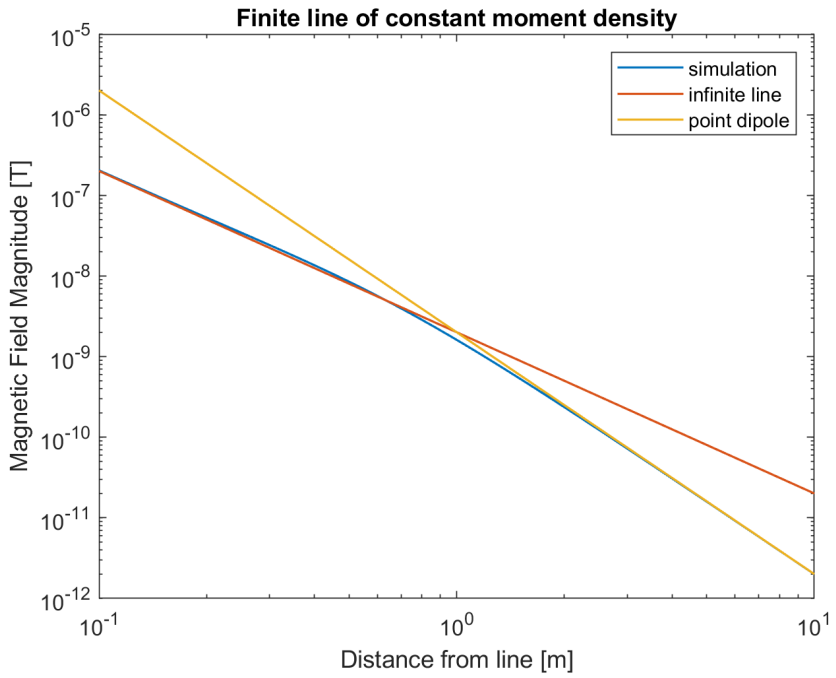

Figure 6-11: Dimensionality of the finite line of linear moment density. At close range, the object "looks" like a line, and indeed the infinite line approximation fits the simulation. At larger distances, the object "looks" like a dipole.

By switching from the simple infinite line approximation to the dipole approximation when the distance from the object is approximately equal to the size of the object (1 meter), we can easily estimate the contributed field from the object at a given distance, staying within about a factor of 2 error even at the worst case "corner" around 1 meter distance.

Chapter 7

The AERO-VISTA Magnetometer

This chapter describes the electronics built around the HMC1053 anisotropic magnetoresistive (AMR) magnetometer [61] to create a fully featured flight instrument. This section will cover all aspects of electronics design up to the digitization of the signal. Section 8.3 will discuss how the data is stored and processed together with other instruments to form the AERO-VISTA Auxiliary Sensor Package (ASP).

7.1 Constraints and Interfaces

7.1.1 Sensor Operational Theory

The HMC1053 magnetometer is a anisotropic magnetoresistive (AMR) magnetometer. Each axis has a balanced bridge, conceptually similar to a Wheatstone bridge [70]. The resistance of the bridge elements change with the magnitude of the incident field to produce a differential voltage. The anisotropic material changes resistance depending on the relative angle of the current flowing through the magnetic material and the magnetic field incident on the material [71]. The sensor passes currents through the four elements such that the differential voltage is a maximum for magnetic fields aligned (or anti-aligned) with the desired sensitive axis.

7.1.2 Sensor Interfaces

The HMC1053 magnetometer has 3 small-signal differential outputs. These outputs are proportional to the incident magnetic field in one of three axes. The polarity of the sensitivity can be inverted with the use of set/reset straps. These are coils wound around the AMR material such that a pulsed current through this circuit will realign the magnetic domains of the AMR material, changing the polarity of the signal [5]. This is useful because static instrument offsets, due either to amplification and detection circuitry, or due to the sensor itself, can be quite large (see Section 4.4.1). Inversion of the sensitive axis inverts the polarity of the desired signal but does not invert the polarity of the constant offsets, allowing for subtraction as discussed in Section 7.6. Other non-ideal effects of the magnetometer are addressed with calibration as discussed in more detail in Chapters 4 and 5.

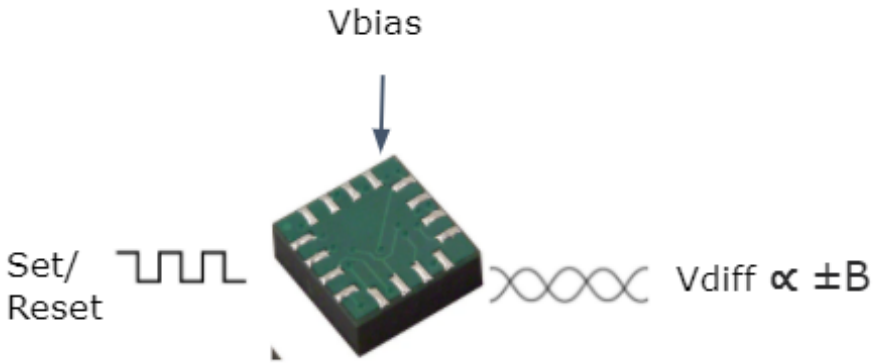

Figure 7-1: Basic operation of HMC1053 set/reset functionality. When a bias voltage is applied, a differential voltage output is proportional to the incident magnetic field. Pulsing positive or negative current through the set/reset straps inverts the output polarity.

7.1.3 Digitization and Storage

The magnetic data must be digitized and stored for eventual downlink to the ground for scientific analysis. In this chapter, we discuss the design of the sensor interface up to the point of digitization with an 8-channel ADC (the AD7771). Chapter 8 will discuss how this digitized signal is stored and eventually downlinked to the ground.

7.2 Architecture and Major Components

From Section 7.1, we need components to digitize the differential output signal and to pulse the set and reset straps. These signals are small (4 µV at 100 nT), and we are concerned with the noise floor, so we also pre-amplify the signal before it is digitized. The major components are diagrammed in Figure 7-2.

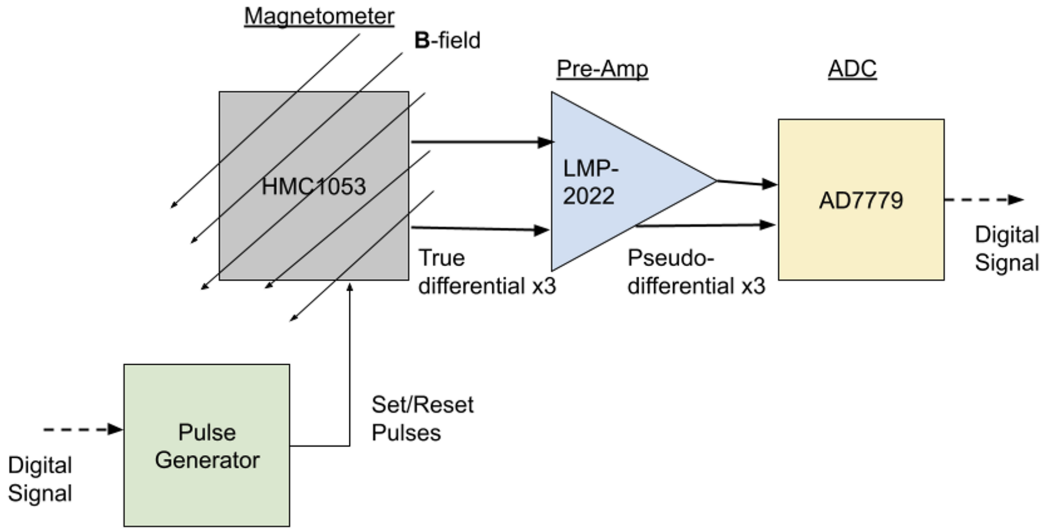

Figure 7-2: Block diagram of analog circuitry to implement magnetic sensing with the HMC1053.

7.2.1 Pre-Amplifier Selection

Several commercially available low noise operational amplifiers were evaluated for use in the pre-amplifier. Datasheet parameters were preferentially taken from the manufacturer's datasheet, but augmented with data from third party sources [72] where needed. Several op-amps were evaluated as listed in Table 7.4. Each op-amp was evaluated based on the following criteria:

- Added uncertainty to magnetic measurement
- Supply voltage requirement
- Power consumption
- Board space

Each parameter was quantified with a figure of merit rating from one to five, which itself was based on a value with physical units. Each figure of merit is given a weighting based on its relative importance to our use. We assigned weights of 5, 2, 2, 2 to uncertainty, supply voltage, power, and board space respectively. In the selection analysis we assumed some other characteristics of the sensing system as reported in Table 7.1. We now discuss the scoring of each parameter in detail and summarize the results in Table 7.4.

Table 7.1: Pre-amplifier selection parameterized assumptions.

Parameter	**Value**	**Reasoning**
Offset Calibration Period	1 second	Results in acceptable temperature drift during sample period
Maximum Temperature Drift	0.5 °C/s	Worst case thermal analysis
Bias Uncertainty Fraction	0.1	Estimate of bias which is uncalibrated
Fcutoff	100 Hz	Hardware filter frequency cutoff
Sensor Noise	95 nVrms	Magnetometer Datasheet
Supply Noise 5V	10 mVrms	Estimated from cable impedance and current draw
Other Supply Noise	0.1 mVrms	Typical LDO performance
Number Needed	8	Two magnetometers per ASP, three axes each, plus two temperature sensors
Vbias	4.096 V	Selected bias voltage for amplifiers

Uncertainty The amplifier contributed measurement uncertainty is the most important decision factor because precision lost at the pre-amplifier stage cannot be regained with other system modifications; uncertainty receives a weight of five. To evaluate the amplifier contributed uncertainty, we combined multiple sources of amplifier uncertainty into one input-referred nVrms value. This differential voltage uncertainty can be mapped into one nTrms value based on the magnetometer gain. In Table 7.2 we list the amplifier uncertainty contribution parameters and explain how these values map into the single input-referred differential voltage uncertainty. These calculations were implemented in a spreadsheet to calculate the results in Table 7.4.

Table 7.2: Pre-amplifier selection datasheet parameters used for uncertainty calculation. For the values used in mapping calculations, see Table 7.1.

Parameter	**Explanation**	**Mapping to differential voltage uncertainty**
vn 1kHz ($nV/\sqrt{Hz}$)	Spectral voltage noise density at 1 kHz	Used with the corner frequency to calculate total voltage noise in frequency range (see Appendix E)
en fc (Hz)	Voltage noise corner frequency	Used with spectral noise density to calculate total voltage noise
in 1kHz ($pA/\sqrt{Hz}$)	Spectral current noise density at 1 kHz	Used with the corner frequency to calculate total current noise in frequency range (see Appendix E)
in fc (Hz)	Current noise corner frequency	Used with spectral noise density to calculate total current noise
Ib slope (pA/V)	Change of input bias current with input voltage	Multiplied with sensor common mode variation and sensor source impedance
Ib slope (pA/C)	Change of input bias current with temperature	Multiplied with rate of temperature change and sensor source impedance
Vos Drift (uV/C)	Input offset drift with temperature	Scaled by expected temperature change between offset calibrations
PSRR (dB)	Power supply rejection ratio	Combined with expected supply noise estimate
CMRR (dB)	Common mode rejection ratio	Combined with bias voltage noise estimate

Supply Voltage The spacecraft bus can only supply the ASP with a single 5V supply. Operating from a lower voltage such as 3.3V or the 4.096V bias voltage is more desirable since these supplies can be made with low noise from a linear regulator (LDO). Operation from the 5V supply will require careful filtering and may create voltage level compatibility complications with the digital storage circuitry so is given a worse score. Operation from voltages above 5V would require a dedicated boost converter, drastically increasing design complexity and introducing new sources for noise, so no amplifiers with voltage supplies above 5V were considered.

Power Consumption With 16 amplifiers per spacecraft (4 per magnetometer, 2 magnetometers per ASP, 2 ASP per spacecraft), the amplifiers may contribute significantly to the power budget. We found that expected power consumption for all pre-amplifiers on one board ranged from 2.4 mW to 108 mW for the amplifiers analyzed, compared to the total ASP power budget of about 2 Watts. At less than 10% of the power budget even in the worst case, the power consumption receives a weight of two.

Board Space Physical space allocated to the ASPs is minimal (about $350\,\mathrm{cm}^2$ each), so the PCBs are limited in size. Components which integrate multiple amplifiers into one package or which are available in small packages are desirable. Board layout area for the range of amplifiers considered ranged from 24 to 240 square millimeters. Even the largest size is only a few percent of the total board space available so board space receives a weight of two.

Table 7.3: Mapping of figures of merit to physical units for amplifier selection.

FOM Category	Quantification
Uncertainty	nVrms
Supply V	Voltage Supply Used
Power	mW
Board space	mm^2 of PCB

Amplifier Selection Results

Table 7.4: Pre-amplifer selection trade results.

	Uncertainty		Supply		Power		Area		
Amplifier	Value [nVrms]	Score [5]	Value [V]	Score [2]	Value [mW]	Score [2]	Value [mm^2]	Score [2]	Total[1]
MAX9618	420	4	4.096	5	2.4	5	24	5	4.5
LT1097	382	4	4.096	5	14	3	240	2	3.6
LT1007	10,000[2]	0	5	2	108	1	240	2	0.9
OPA209	767	3	5	2	88	2	64	3	2.6
LT1012	288	4	4.096	5	20	3	240	2	3.6
LT6010	217	5	4.096	5	5.2	4	60	4	4.6
LMP2022	143	5	4.096	5	44	2	60	4	4.3
OPA140	262	4	5	2	72	2	70	3	3.1
OPA2188	2502	1	4.096	5	19.2	3	60	1	2.1

[1] Computed with weighted average.
[2] Error dominated by bias current. uncertainty

From Table 7.4, we see that the part numbers MAX9618, LT6010, and LMP2022 are the most promising candidates for their high selection score. For component availability issues during supply chain disruptions of 2020 and 2021 [73], the LMP2022 was selected as the pre-amplifier over the other two most viable options.

7.2.2 Digital to Analog Conversion

Noise and Uncertainty

The analog to digital conversion itself can introduce noise and errors into the signal. The amplification of the pre-amplifier allows us to pick an ADC with less regard to the input noise voltage. We have designed a pre-amplifier with gain of about 50 V/V. Our ultimate measurement goal is 100 nT precision, so any error contribution which we can keep below about 10 nT can be largely ignored as it will likely be dominated by other error contributions. With our chosen bias voltage and pre-amplifier, a signal of 10 nT will create an ADC input voltage of about 20.5 uV.

$$V_{adc} = B * G_{mag} * G_{amp} = 10\,\mathrm{nT} * 1\,\mathrm{mV\,G^{-1}} * 50\,\mathrm{V\,V^{-1}} \approx 20.5\,\mu\mathrm{V} \qquad (7.1)$$

Quantization of the signal can also introduce errors. Using our 10 nT rule of thumb, we require a dynamic range of approximately 10,000, requiring an ADC with at least 14 bits. Even more bits would be preferable because this would account for static offsets that increase the the total input range beyond just what's required for the magnetic measurement.

Sampling and Clocking

It is also important that the ADC sample all magnetometers at once. An ADC which uses an internal MUX with a single ADC circuit will need to sample at 8 times the actual data rate to sample all channels. This aliases noise into the signal at frequencies up to 8 times the effective data rate, increasing measurement noise. This lesson was learned with the prototype board, MagEval, where the ADS1248 ADC was chosen as the measurement ADC. For MagEval testing, the ADC was run at 80 SPS to achieve an effective data rate of 10 SPS, increasing the noise of each sample. Other lessons learned from MagEval testing are discussed in Section A.2.1.

Component Choice

The ADC options were also checked for added uncertainty from thermal drift of input offset and integral non-linearity, but these effects were relatively small compared to the contributions from the pre-amplifier as the signals at the input to the ADC are already amplified.

The ADC selected for the AERO-VISTA magnetometer to meet all of these requirements is the AD7771. The AD7779 was used during some initial prototyping, but component availability issues required a change of part number. These two devices have very similar analog performance, and the digital interface (register map) is identical.

7.3 Analog Design Implementation

With the conceptual block diagram from Figure 7-2 and with the major components selected, the next step is to implement the design in detail. This occurs in three stages. First, we fill in design details such as passive components with a full schematic capture. Next we assign physical parts to the components and layout the physical printed circuit board (PCB). Finally we have the PCB fabricated and the components populated on the board. In this section we describe schematic capture and layout of the magnetometer circuitry but leave fabrication and assembly details until Chapter 8.

7.3.1 Schematic Capture

The schematic for the analog design is hierarchical with the main "Magnetometers" schematic relying on multiple instances of the "Magnetometers Channel" and the "Magnetometer Filter" schematics. The magnetometer filter is the pre-ADC filter designed for a cutoff frequency of 48 Hz, and a settling time to 50 PPM accuracy of 33 ms. The filter block is used once for every ADC input (8 times per board). The magnetometer channel block is used twice per board. Each magnetometer channel independently implements the magnetometer, reference voltage, temperature sensor, set/reset switches, and pre-amplifiers for one three-axis magnetic field measurement.

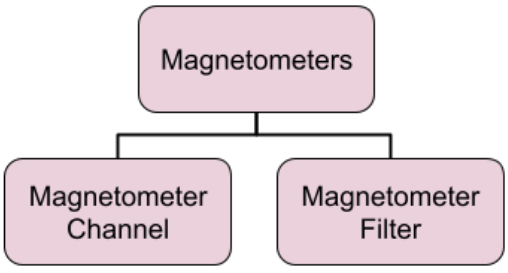

Figure 7-3: Hierarchical schematic structure for magnetometer implementation.

7.3.2 Layout

The magnetometers are placed as far apart as possible on the PCB while still maintaining separation from the magnetically active digital components of the Raspberry Pi and the switch mode power supplies. We minimize variation of power supply current signals in the vicinity of the magnetometers and ensure all high power current paths do not flow near the magnetometers. The magnetometers do not sit between the power supply location and any devices, so no other component current will be observed in the magnetometer measurements. The ground and power planes are left continuous under the magnetometer as the loop area with close parallel planes is smaller than that created by imbalances between current flow around the plane break if the plane was removed under the magnetometer.

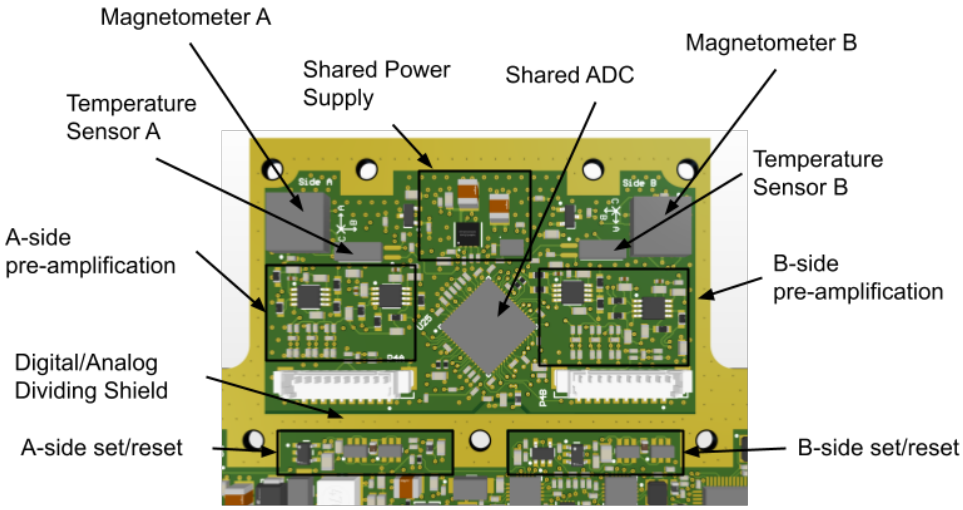

Figure 7-4: Placement for magnetometer and associated electronics. The analog signals are kept separate from the digital signals, and the magnetometers are placed as far away from metal and high current paths as possible. Figure from Hrafn V1.4.

The temperature sensor is placed as close to the magnetometer as possible to minimize temperature difference between the temperature sense location and the magnetometer location. In this layout, the edges of the two components are about 1 mm apart.

Screening of the Raspberry Pi[1] using techniques as described in Chapter 6 has determined that about 8 cm separation is adequate for the Raspberry Pi to be undetectable at our sensitivity threshold. The design and layout of the rest of the ASP PCB for minimization of interference with the magnetometers is discussed in Section 8.3.

7.4 Noise Estimation

One important contribution to the error budget discussed in Section 7.5 is the measurement noise inherent to the analog design. We analyze the magnetic design for noise contribution from the following sources:

- Magnetometer voltage noise
- Pre-amp voltage noise
- Pre-amp current noise
- Resistor noise (Johnson-Nyquist)
- ADC Noise

For each noise source, we analyze the expected spectral noise density in $\mathrm{nV}/\sqrt{\mathrm{Hz}}$. For proper comparison among all noise contributions we scale the effective noise to that at the magnetometer output based on the path gain.

Magnetometer Noise The magnetometer noise spectrum has been estimated from datasheet parameters as described in Section 4.4.1 and with results plotted in Figure 4-4.

ADC voltage noise The selected LMP2022 op-amps are chopper stabilized and have no 1/f corner frequency [75]. Additionally, the input referred voltage noise density depends on the gain of the feedback network. The feedback network used in this design provides about 50 V/V gain, setting the frequency independent voltage noise contribution of the LMP2022 to $16\,\mathrm{nV}/\sqrt{\mathrm{Hz}}$.

[1] Raspberry Pi Zero W version 1 [74].

ADC current noise The input referred noise current is mapped into voltage noise by multiplication with the impedance looking out the input terminals of the op-amp. The datasheet input-referred current noise of the LMP2022 is $100\,\mathrm{fA}/\sqrt{\mathrm{Hz}}$ [75]. The sensor network differential resistance using Thevenin equivalent circuit analysis techniques is $10.5\,\mathrm{k}\Omega$ and is dominated by the input feedback resistors used to set a constant gain. Therefore, the equivalent magnetometer-output referred voltage noise of the op-amp current noise is given by Eq. (7.2).

$$S_V = 100\,\mathrm{fA}/\sqrt{\mathrm{Hz}} * 10.5\,\mathrm{k}\Omega = 1.05\,\mathrm{nV}/\sqrt{\mathrm{Hz}} \tag{7.2}$$

The input resistance is adequately low such that the op-amp input current noise will not be a dominant noise source (it is always dominated by op-amp input voltage noise).

Resistor Noise The resistor noise is the Johnson-Nyquist thermal noise[2] contributed by the resistors in the analog network [72].

$$\overline{v_n^2} = 4k_BTR \tag{7.3}$$

Just as for computation with the input current noise, the Thevenin equivalent model finds a differential resistance of $10.5\,\mathrm{k}\Omega$, so we can compute the rms voltage noise in Eq. (7.4).

$$\sqrt{\overline{v_n^2}} = \sqrt{(4.138 \times 10^{-23}\,\mathrm{J\,K^{-1}})(300\,\mathrm{K})(10.5 \times 10^3\,\Omega)} \approx 13\,\mathrm{nV}/\sqrt{\mathrm{Hz}} \tag{7.4}$$

This is a similar noise contribution to that of the op-amp input referred voltage noise. We have set the differential resistance to this value by design; a larger resistance will reduce the gain dependence on the variable magnetometer bridge resistance, but if it is too large it will become the dominant noise source. The differential resistance

[2] We avoid using carbon composite or thick film resistors which tend to create excess noise beyond the thermal minimum [76].

is as large as possible without turning the input resistor Johnston-Nyquist noise into the new dominant noise source.

ADC Noise The ADC is after the 50 V/V gain of the pre-amplifier, so all noise contributions at the input to the ADC are scaled down by a factor of 50 for comparison to the magnetometer output voltage noise. The ADC input referred voltage noise is $270\,\mathrm{nV}/\sqrt{\mathrm{Hz}}$ at 1 kHz, and the integrated noise from 0.1 to 10 Hz is 6.8 uVrms. The ADC programmable gain amplifier (PGA) setting of 4V/V also provides a reduction of noise voltage rms by of about 2 as seen in plots like Figure 21 of the AD7771 datasheet [77].[3] These two parameters were used with a piece-wise power-law model for spectral noise density to estimate the spectral noise contribution of the amplifier as described in Appendix E.

7.4.1 Results

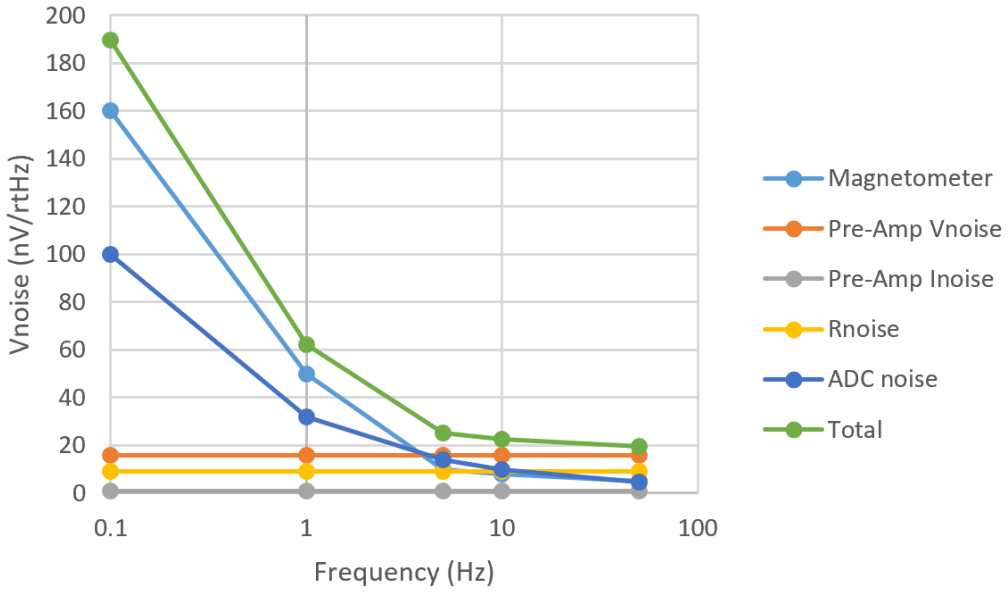

Figure 7-5: Frequency dependence of noise sources mapped to equivalent magnetometer output voltage noise.

[3]Note that on initial read, Table 25 of the datasheet [77] would seem to indicate that noise is reduced by increasing the decimation rate, and *per sample* this is true, but this does not affect the *spectral* noise density and is instead just the $\sqrt{N}$ improvement expected with hardware averaging.

The noise contributions from each source are assumed to be independent so are summed together as the square root of the sum of squares. Individual contributions and total noise over frequency are plotted in Figure 7-5. The approximate integrated noise contribution is integrated piece-wise as described in Appendix E. Integrating from 0.1 to 10 Hz finds a total noise of 416 nVrms. This corresponds to an integrated magnetic noise of 10.1 nT. This noise value is verified by test in Section 7.7.

7.5 Error Budget

Table 7.5: Total magnetic sensing circuitry error budget by analysis.

	Magnetometer	**Amplifier**	**Resistors**	**ADC**[1]	**Total**[2]	**B Error**
Offset[3]	5.12 mV	5 uV	2.9 mV	0.8 uV	5.9 mV	140 uT
Offset[3] **Tempco**	2.1 uV/°C	0.02 uV/°C	0.29 uV/°C	0.04 uV/°C	2.1 uV/°C	51 nT/°C
Non-linearity	4.1 uV	0	0	0.03 uV	4.1 uV	100 nT
Noise[4]	--	--	--	--	0.42 uVrms	10 nT
Sensitivity Tempco	0.29 %/°C	0	0.01 %/°C	6 ppm/°C	0.29%/°C	290 nT/°C

[1] ADC parameters have been scaled by pre-amplifier gain to the equivalent magnetometer output error when not defined as a fraction of full scale.
[2] Summed using square root of sum of squares assuming error independence.
[3] The offset improvement due to set/reset straps will be considered in Section 7.6.
[4] Noise from each source is separately considered in detail in Section 7.4. Here we just use the total noise contribution.

The error budget is reported in Table 7.5 and combines the uncertainty contribution from all sources to verify that by analysis we will meet our required 100 nT precision. The magnetometer contributions to error are dominant for all non-ideal properties except temperature coefficient of the offset. Offset effects are compensated for using the set/reset functionality of the magnetometer as described in Section 7.6.

Remaining errors due to offset, offset temperature coefficient (tempco), and sensitivity tempco will all be calibrated out as described and demonstrated in Chapters 4 and 5.

7.6 Sampling Method

Critical to our ability to achieve accurate magnetic measurement is the ability to calibrate out slowly varying offsets. As seen in Table 7.5, the static offset and its variation over temperature are large compared to our 100 nT measurement requirement. Here we describe how these effects can be calibrated out using the set/reset functionality of the magnetometers to periodically reverse the polarity of the magnetometer sensitivity.

Without the switching operation, we have a desired magnetic field signal $B(t)$ and an undesired offset signal $O(t)$. Together these create what we actually measure: $M(t)$.

$$M(t) = B(t) + O(t) \tag{7.5}$$

For now we ignore the various gains and scalings that would provide physical units. The switching operation is the multiplication of another function, $P(t)$, so named because it comes from the polarity reversal.

$$M(t) = P(t) * B(t) + O(t) \tag{7.6}$$

We know $P(t)$ and are measuring $M(t)$, but we know neither $O(t)$ nor $B(t)$. With only this one equation and two unknown functions, we cannot know perfectly $O(t)$ or $B(t)$; however, by making some assumptions about $O(t)$ we will get closer to subtracting out its effect and knowing $B(t)$ more accurately.

Critically, $O(t)$ does not change very quickly with time. We have seen from datasheet analysis that in the worst case the offset will change by 51 nT/°C (see Table 7.5). We have estimated that the temperature of this sensor will not change

faster than 0.5 °C/s, so the offset contribution will not be larger than 26 nT/°C. From this, we baseline a set/reset period of 1 second.[4]

Once we have the set/reset period, we know the function $P(t)$ and can estimate $B(t)$ and $O(t)$ separately. We use the set/reset polarity change to estimate the $O(t)$ at a regular interval; we denote this estimate as $O'(t)$. This in turn allows us to solve for a best estimate $B'(t)$ which should be close to the actual $B(t)$.

$$M(t) = P(t) * B'(t) + O'(t) \tag{7.7}$$

$$B(t) \approx B'(t) = (M(t) - O'(t))/(P(t)) \tag{7.8}$$

Note that in this case, division by the polarity is equivalent to multiplication because P(t) is actually only ever -1 or 1. We know $O(t)$ will change slowly with time (we've designed the set/reset period to ensure this). $P(t) \times B'(t)$ in general does not change slowly with time, so as a first pass we can simply low-pass filter the measured signal, driving the contribution of $P(t) \times B(t)$ towards zero and allowing us to find an $O'(t)$.

7.6.1 Frequency Domain

This switching and low-pass operation can be understood further with frequency domain analysis. A cartoon of the relevant signals in the frequency domain is shown in Figure 7-6.

The multiplication of the magnetic field signal by the polarity signal creates convolution in the frequency domain. Convolution with an impulse preserves the shape of the convolved signal. Then we can use a sharp low pass filter to find O'(t). Of course, this is only perfect if there is no magnetic signal at the same frequency of the polarity switching (which there is). A magnetic signal at the same frequency as the polarity switching will be shifted to zero frequency, and will be included in the estimation of the offset. This is a fundamental problem which cannot be resolved

[4]This is a software-adjustable parameter so different periods may be tested in flight.

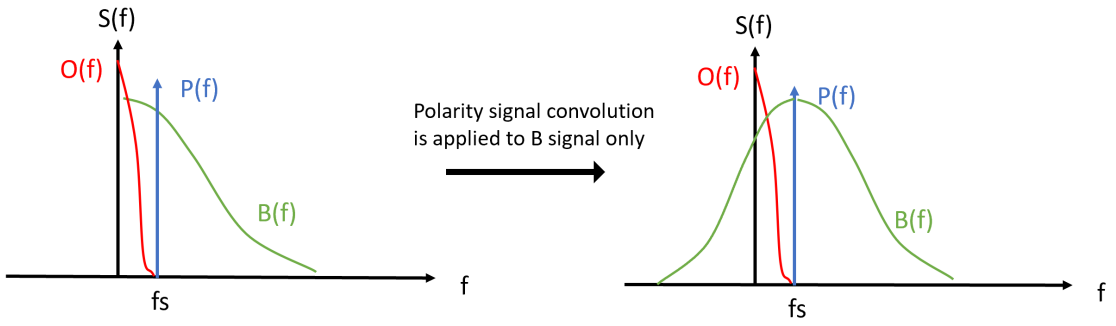

Figure 7-6: Frequency domain sketch of offset and magnetic field signals. O, P, and B represent the offset, polarity, and magnetic field signals. Multiplication of the polarity signal in the time domain is convolution in the frequency domain. The drift of the offset occurs at lower frequencies than the set/reset rate. The polarity switching function is a square wave, so in the frequency domain is actually a sinc function, but for simplicity we've approximated it as single frequency in this cartoon.

as long as magnetic fields are changing at the same time as we are performing our switching operations. By choosing to low pass filter the measurement with the offsets included, the estimation of the offset is sensitive to magnetic changes at 1 Hz. This creates artifacts in the offset estimation that show as a strong 1 Hz square wave noise signal as seen in Figure 7-7. Looking at typical noise frequency distribution such as provided in Appendix C, this is not ideal, because noise is dense at low frequencies (like 1 Hz).

However, the density of magnetic noise decreases at higher frequencies. Additionally, the change in magnetic signal due to reorientation of the spacecraft will be of the same frequency as the rotation rate of the spacecraft, very low, on the order of mHz. Therefore, the best estimate of the offset is achieved by minimizing the amount of time between the measurements used to estimate the offset.

The settling time of the analog hardware sets a minimum amount of time between the last positive polarity measurement and the first negative polarity measurement on either side of a switching event. As implemented, this settling time is 33 ms for 50 ppm settling accuracy. Rounding up, this requires ignoring 2 samples (40 ms). Instead of sampling the offset with a square wave, we now have the sampling waveform shown in cartoon in Figure 7-8. We call this "boundary sampling" because

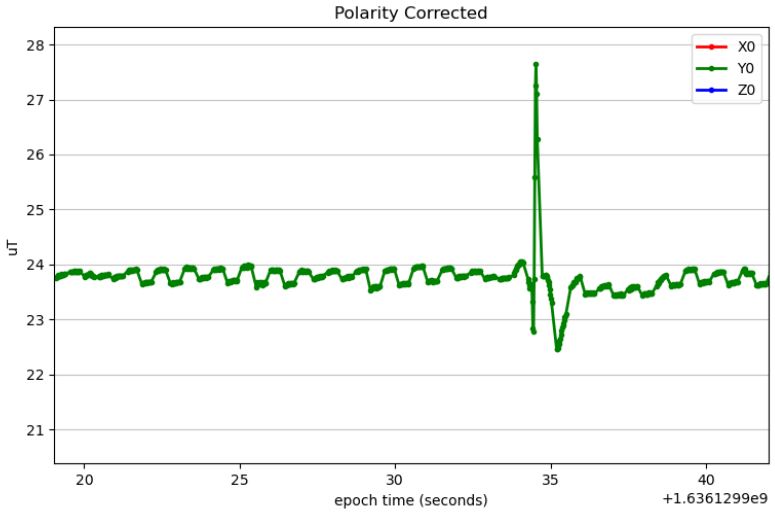

Figure 7-7: 1 Hz artifacts from poor estimation of offset in the presence of magnetic noise signals.

instead of sampling the offset with all of each set/reset state, we are only sampling on the boundaries of the polarity switching events.

We implement this waveform in a MATLAB simulation as shown in Figure 7-9. With this implementation, we can compute the spectral power density of the sampling (estimated with the MATLAB periodogram function[5]) as in Figure 7-10. The boundary sampling method captures less low-frequency content, and therefore the offset estimation will be less affected by magnetic signal change which is more powerful at low frequencies.

[5]see `https://www.mathworks.com/help/signal/ref/periodogram.html#d123e121332`

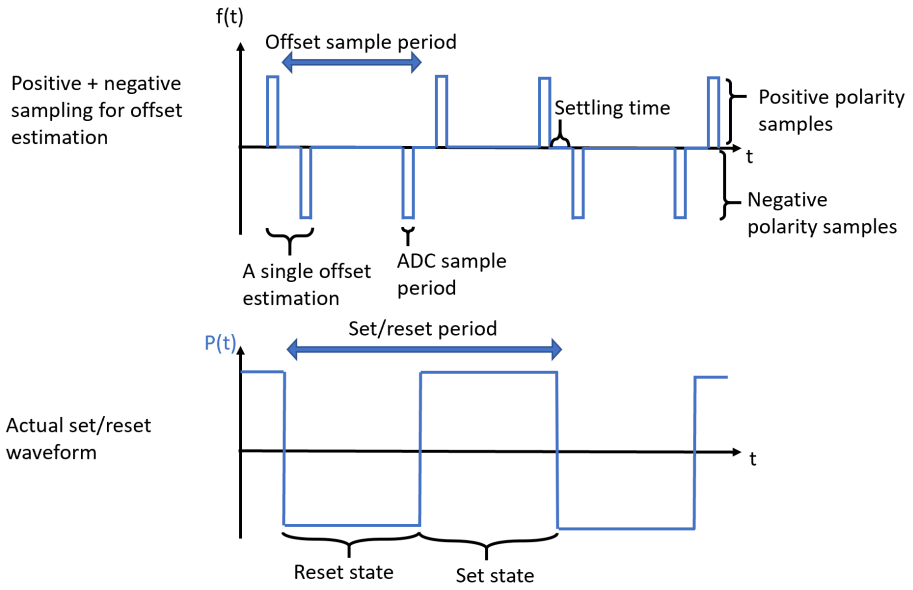

Figure 7-8: Cartoon of the boundary sampling method with major features indicated. The closely spaced positive and negative samples reduce the amount of low frequency magnetic signal included in the offset estimation.

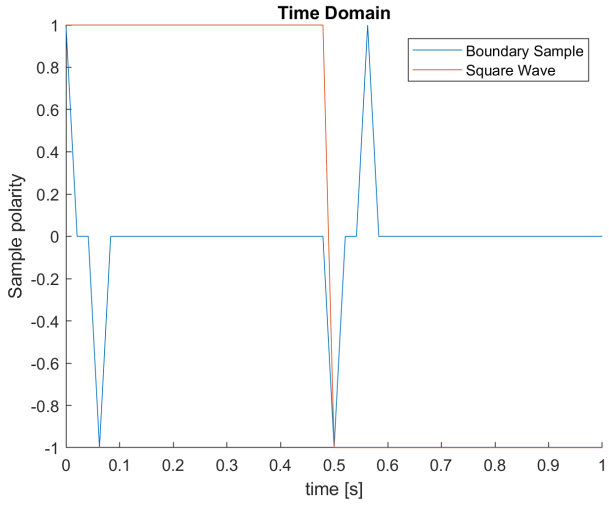

Figure 7-9: Implementation of the boundary square wave sampling waveforms in MATLAB. The periodogram of these waveforms are shown in Figure 7-10.

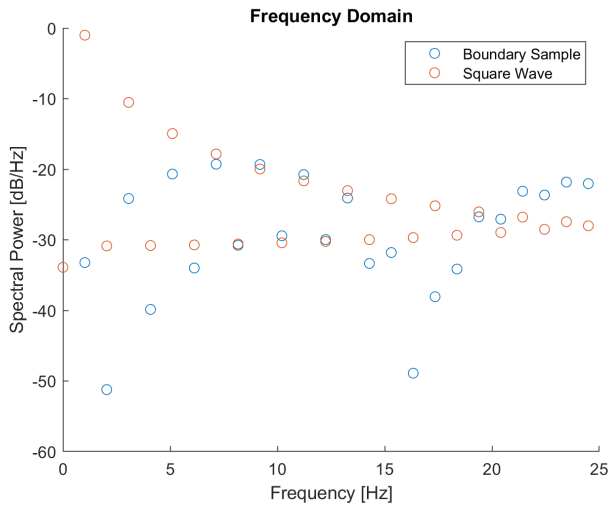

Figure 7-10: Power spectrum of the boundary sampling and square wave sampling methods computed by periodogram of the signals in Figure 7-9. The boundary sampling method captures less power than the square wave at low frequencies.

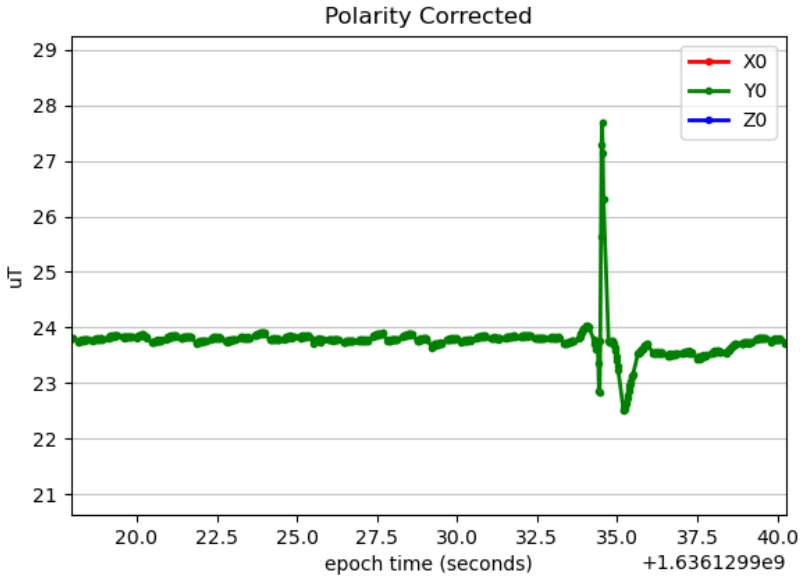

Figure 7-11: Minimum period estimation of offset has removed the 1 Hz artifacts seen with 1 Hz square wave offset sampling in Figure 7-7.

7.7 Engineering Model Measurement Results

The magnetic measurement circuit described in this chapter is implemented in a stand-alone payload (the ASP) described in Chapter 8. We evaluate the as-built noise floor performance in a mu-metal shielded room, similar to the test described in Section 4.4.2.

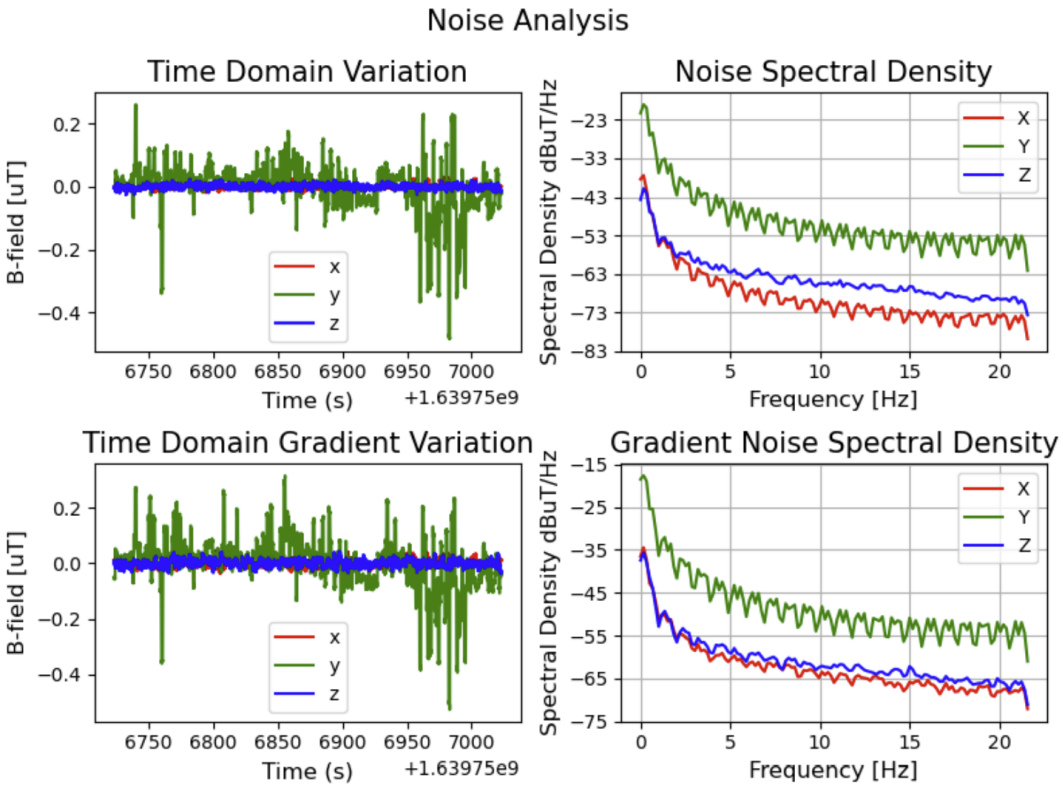

Figure 7-12: Measured noise of the engineering model. Left figures show the time domain magnetic field measurements and the right figures show the frequency domain. The top figures plot the magnetic field of magnetometer A, and the bottom plots the difference between magnetometers A and B. The Y-axis noise is significantly higher but still meets 100 nTrms measurement requirements. The effect of the 1 Hz set/reset switching is seen with its harmonics in the spectral density plots.

From 0.1 to 10 Hz, the expected noise by analysis was about 10 nTrms. The measured noise in nTrms for the 3-axes was [9.3, 87., 7.1]. The X- and Z-axes seem to verify our analysis in the noise budget. The larger Y-axis noise is likely due to self-interference from the Raspberry Pi computer (Y-axis is normal to the plane of

the Raspberry Pi PCB), though may be due to other switching electronics in the ASP PCB. The Y-axis noise is higher in both magnetometers, though is slightly lower at 45 nTrms in magnetometer B. Despite the worse performance in the Y-axis, we are meeting the 100 nT requirement in all axes.

7.8 Summary

This chapter has covered the electronics design around the HMC1053 magnetometer. This device produces a small differential output proportional to the incident field. This small signal is amplified by an op-amp pre-amplifier, and then digitized by a simultaneously sampling analog to digital converter. We discussed the implementation of the analog signal chain including schematic capture and PCB layout. The PCB was designed to minimize the magnetic interference from other components on the magnetometers. This design's total analog signal noise was estimated for all sources and combined to produce Figure 7-5. The noise estimate was combined with other error sources to create a complete error budget in Table 7.5.

Offset effects create very large error, but the static and slow-varying offsets can be estimated by flipping the sensitive polarity of the AMR magnetometer. By sampling the output with both a positive and negative sensitivity we can estimate which part of the signal was caused by the magnetic field and which was caused by the instrument offset. This sampling will always partially combine the magnetic field and offset signals, but by acknowledging that the offset changes very slowly, we are able to separate the two effects in the frequency domain. We identified an improved offset sampling method which minimizes the amount of magnetic signal contribution to the offset estimate.

The design described in this chapter has been shown to meet AERO-VISTA's measurement requirement of 100 nT precision with repeatability over spacecraft operating conditions. Chapter 5 reports performance of the implemented magnetometer when combined with our calibration method. In Chapter 8 we describe how this magnetic

sensing circuitry and PCB layout has been implemented on a stand-alone payload, the Auxiliary Sensor Package (ASP).

This page is intentionally left blank.

Chapter 8

The AERO-VISTA Auxiliary Sensor Package Design

8.1 ASP Introduction

The AERO-VISTA magnetometers are implemented on a payload called the Auxiliary Sensor Package (ASP). This payload is independent from the main Vector Sensor payload which performs RF processing and storage (see Section 1.1.3). The ASP provides data which contextualizes the data captured by the main science instrument. This includes observations to localize radio emissions observed by the vector sensor with respect to Red and Green line auroral arcs [78]. The ASP can also observe the shape and deployment status of the vector sensor antenna elements. Finally, the ASP measures the local magnetic field to determine the direction of RF-wave propagation with respect to the local magnetic environment. The magnetometer data can also be used to observe the presence of field aligned currents which perturb the local magnetic field away from what would be predicted by a global magnetic model.

To meet these requirements, the ASP incorporates two types of instruments: a RGB camera and magnetometers. The camera is used to observe auroral emissions and to image the deployed antenna. The magnetometer on the ASP meets the magnetic science sensing requirements for aligning the RF waves with the local magnetic field.

The main components of the ASP are:

- **Computer**: A Raspberry Pi Zero is a small and low power single board computer with significant community support and software packages readily available [74]. All software on the ASP is implemented on the Raspberry Pi Zero.
- **Magnetometers**: Two Honeywell HMC1053 magnetometers provide a spatially diverse measurement of the in-situ magnetic field amplitude and vector direction measurements. A custom analog system is built around these magnetometers and described in detail in Chapter 7.
- **Engineering Camera**: A Raspberry Pi Camera (V2.1) [79] provides optical measurement of auroral events and confirmation of antenna deployment. This camera is designed for use with the Raspberry Pi computer and no custom electronics are required for connection.
- **Custom PCB**: A custom PCB integrates the analog electronics for the magnetometers, power distribution electronics, and digital interface electronics for the ASP. The design of this PCB is described in detail in Section 8.3.
- **Custom Aluminum Enclosure**: The aluminum enclosure provides mechanical support to the other elements of the ASP, and also serves as an EMI shield between the ASP components and the vector sensor. The enclosure is described in detail in Section 8.4
- **Cables and GSE**: The cables connect the ASP to the spacecraft bus and vector sensor to provide necessary power, clock, and data connections. Ground support equipment (GSE) is used for ground testing of the ASP.

The ASP functional diagram in Figure 8.1 describes the interfaces internal and external to a single ASP module. There are two ASP modules per spacecraft, and then two spacecrafts (AERO and VISTA) for a total of four in-flight ASPs. The Raspberry Pi plugs into the PCB such that the PCB can be considered an unusual form factor and very customized "hat" for the Raspberry Pi [80]. The ECam is separate from the PCB, but is still internal to the ASP module. The ASP receives power and a data

connection from the spacecraft bus (called the M6P bus), and receives a synchronized clock signal from the vector sensor payload.

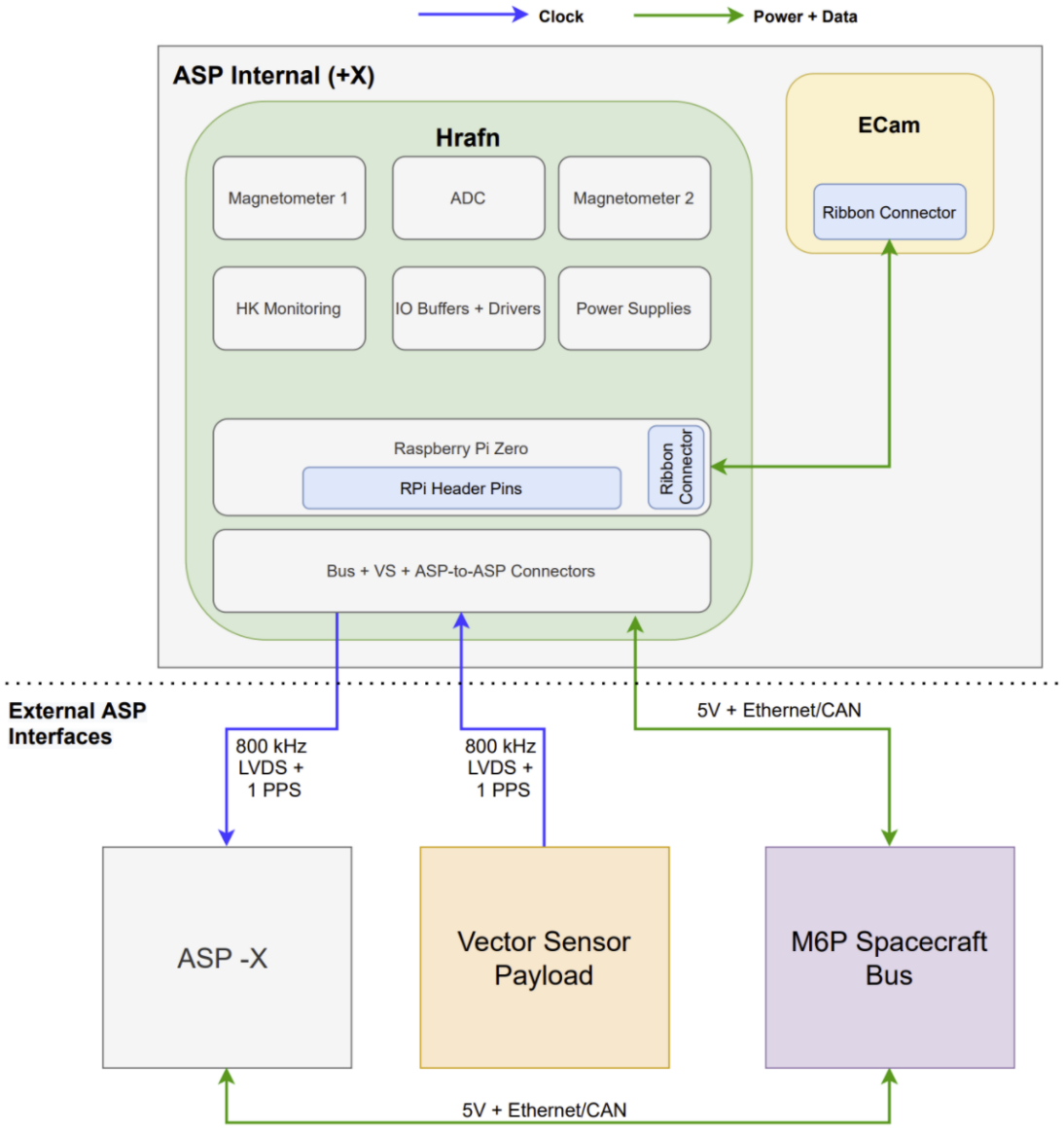

Figure 8-1: ASP Functional Diagram. Functionality that resides on the custom PCB is shown in the green box. Connections from the PCB to other devices show interactions with other ASP system components.

8.2 Imaging System

The ASP can take pictures or videos with a Raspberry Pi Camera V2.1. Software configuration of the camera over command allows us to set the integration time of each image to between 0.1 and 10 seconds. A 195 degree field of view fisheye lens is used with the Pi camera to image one hemisphere of the vector sensor antennas. With two ASP modules on each spacecraft, the two cameras together can image the entire vector sensor. See the thesis by Cadence Payne for more details on optical sensing with the ASP modules [78].

8.3 Electronics Design

The ASP electronics are implemented on a custom PCB. This PCB is formally known as the "ASP PCB", but has been given the additional informal name "Hrafn" which shows up in project documents.[1] The electronics are designed to support the hardware which meets mission requirements, primarily the Raspberry Pi, the magnetometers, and the Pi Camera. Key functions include providing power to the sensors and the computer, creating a data connection between the ASP computer and the spacecraft bus, providing overcurrent fault protection for tolerance to radiation effects like latchup, and monitoring the general health and status of the instruments. Additionally, the electronics have been designed to produce low EMI, particularly any EMI which might not be phase locked to the vector sensors ADCs, and has been designed for quick and inexpensive development.

The major functionality of the Hrafn PCB is diagrammed in Figure 8-2, including the part number selection for major components. The digital interfaces were tested with evaluation modules in a breadboard format and stand alone Raspberry Pi (using

[1]The name Hrafn follows a spacecraft-wide theme of naming PCBs in various Scandinavian languages. This theme was adopted since the spacecraft will be observing Earth's Aurora which are famously visible from high latitudes. The name Hrafn is the Old Norse word for raven, a reference to the two ravens Huginn and Muninn who roosted on Odin's shoulder. The two would fly all over the world to report their observations back to Odin [81]. With two ASPs in the "shoulder" of each spacecraft, each taking pictures, the ASPs are the Huginn and Muninn to the Odin of the rest of the spacecraft.

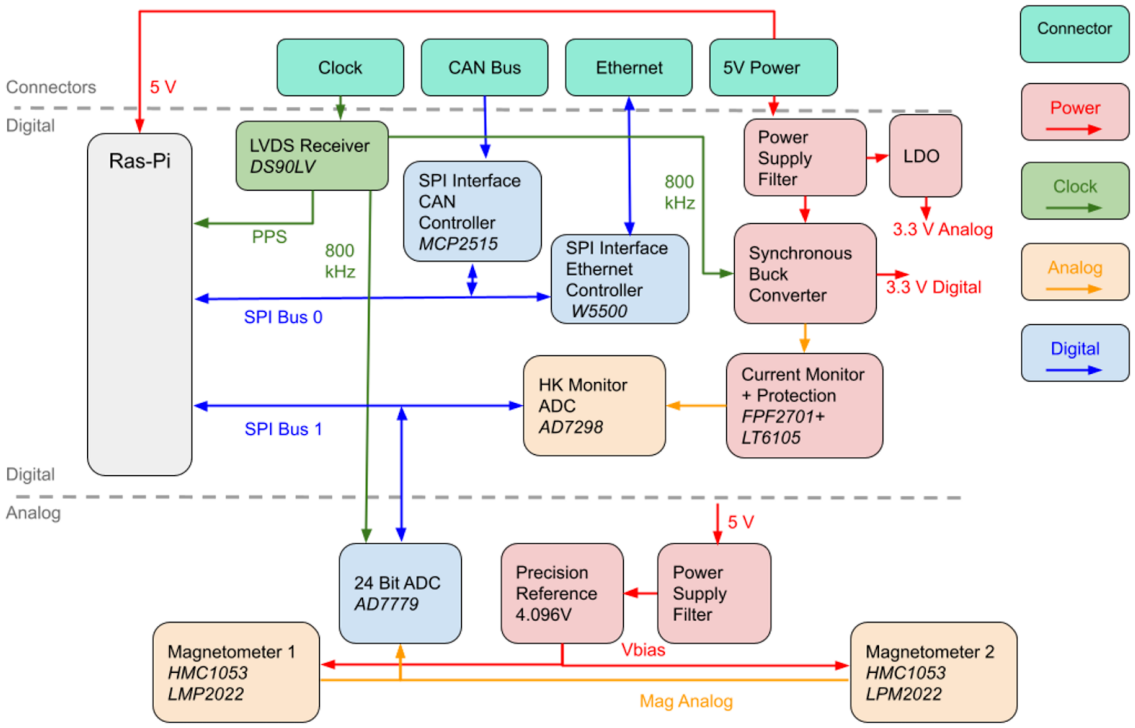

Figure 8-2: ASP PCB functionality block diagram with part numbers for major components indicated in *italics*.

a prototype called the ASPIT, see Section A.2.3). The magnetometer design was tested with the magEval implementation of the HMC1053 magnetometers (see Section A.2.1). The ADC interface was tested with a custom AD777x evaluation board (see Section A.2.2). These devices together allowed us to incrementally write software, debug, and refine our design before committing to the final version with the Hrafn PCB.

8.3.1 Schematic Capture

Following block diagram creation and testing with prototypes and evaluation modules, a detailed schematic was captured with Altium designer. We organized the schematic design with a hierarchical format as summarized in Figure 8-3. A top level schematic implements the connections between the different sub elements and an annotated screen capture of the top level schematic is shown in Figure 8-4.

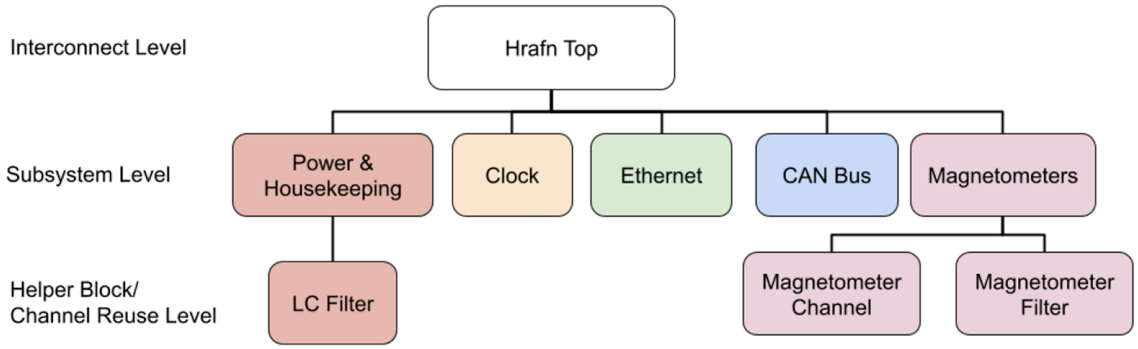

Figure 8-3: ASP PCB hierarchical design for schematic capture.

Power Supplies and Housekeeping

The power supply and housekeeping section provides power to the devices on Hrafn including the Raspberry Pi. Ultimately all power in the ASP comes from a 5V supply from the spacecraft bus electrical power system (EPS).

Clock

The clock section of the PCB includes the ability to receive, resend and detect LVDS clock signals. We have included the ability to switch from the external clock to an internal clock generated by the Raspberry Pi to allow the magnetometer ADC to operate even when the ASP is disconnected from the spacecraft (such as during bring-up testing) or when the ASP is operating but the vector sensor is turned off (such as during the acquisition of magnetometer calibration data).

The 800 kHz clock signal from the Vector Sensor is phase synchronized with the 50 MHz reference clock used to discipline the RF ADCs. The ASP uses the 800 kHz clock to discipline the switch mode power supplies (SMPS) to keep EMI emission phase locked to the ADC sampling, making it easier to filter. Additionally, the 800 kHz clock is used to discipline the magnetometer ADC so those samples are also phase locked to both the EMI emission of the spacecraft and to the RF sampling of the main vector sensor payload.

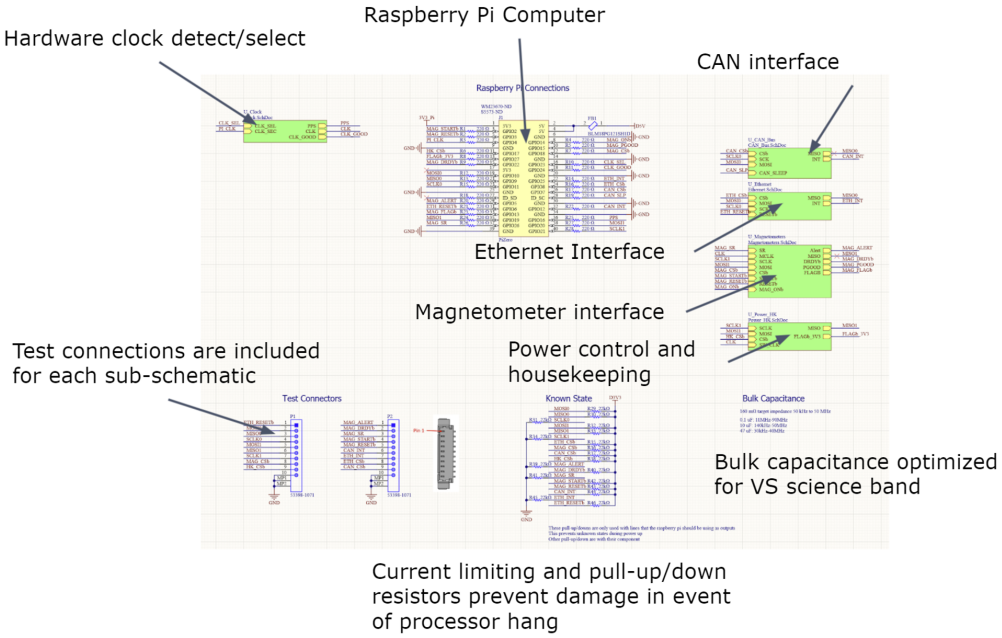

Figure 8-4: ASP PCB annotated top-level schematic. Filename: Hrafn_Top.SchDoc Version: 1.4.

Ethernet and CAN Interfaces

The Ethernet and CAN capabilities are provided by SPI interfaced network controllers, the MCP2515 for CAN capability, and the Wiznet W5500 for Ethernet. Both of these devices have device tree overlays already built into Raspbian as discussed in Section 8.5.3.

8.3.2 Layout and PCB Design

Placement

Layout of the Hrafn PCB first required the creation of a floor plan with rough placement goals for each major subsystem. It was at this point that EMI and magnetic interference considerations were used to keep switching or other magnetic components as far away from the magnetometers as possible. The floor plan was then used to create an initial placement of all components as shown in Figure 8-8.

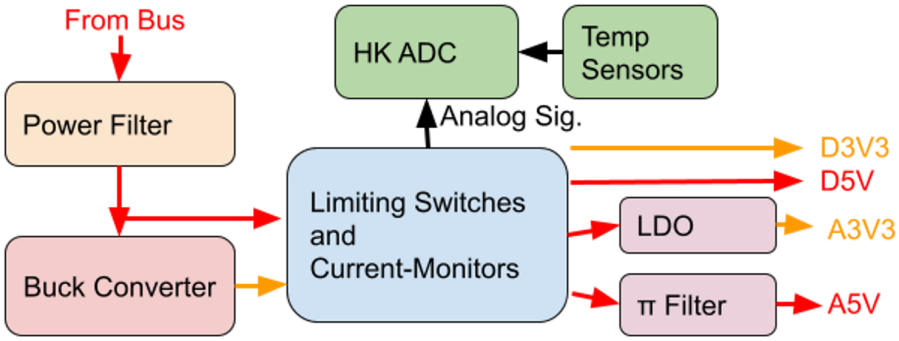

Figure 8-5: ASP PCB Power Supply and Housekeeping Section Block Diagram

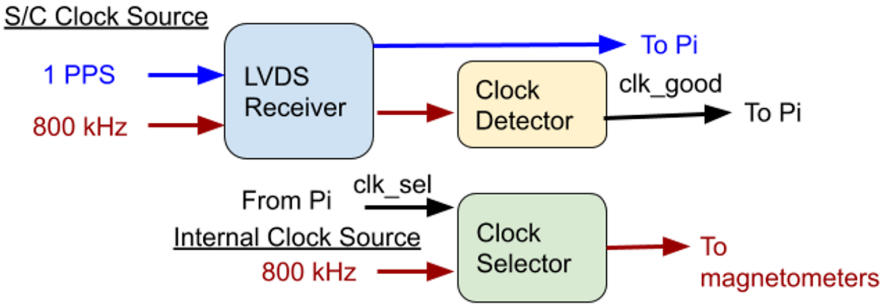

Figure 8-6: ASP PCB clock section block diagram.

Primary drivers during floor plan design include:

- Proximity of highly interconnected subsystems to keep total routing lengths short.
- Distance between the Ethernet magnetics to the magnetometers.
- Distance between the Raspberry Pi and the magnetometers.
- Distance between the switch mode power supply and the magnetometers.
- Distance between the two magnetometers (for spatial diversity of measurement).
- Placement of the magnetometer temperature sensors as close to the magnetometers as possible.
- Minimization of total current path lengths for the power supplies.

Stackup

The Hrafn PCB is designed with eight copper layers. EMI shielding is provided by two unbroken ground planes (except at digital/analog interface) on layers 2 and 7,

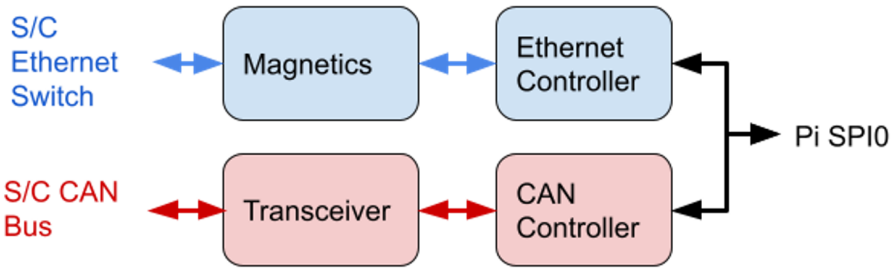

Figure 8-7: ASP PCB data interface section block diagram.

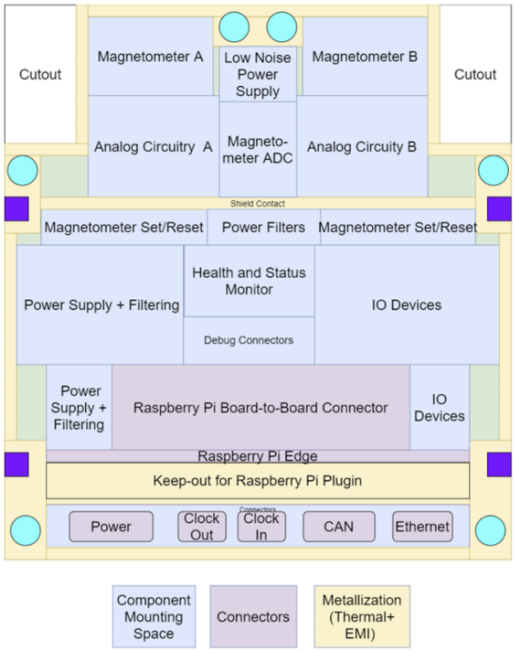

Figure 8-8: Hrafn initial floorplan.

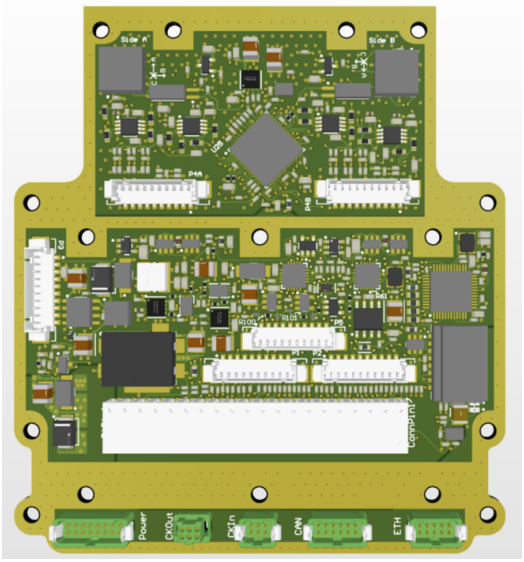

Figure 8-9: Hrafn layout in 3D rendering.

one layer into each side of the board. The outermost layers are used for components and low speed routing only as the short traces associated with component teardrops or low switching speed will keep EMI down. This is important as these layers do not have PCB shielding for EMI reduction. The innermost layers are used for the power planes, where generally one plane is used for 3.3V and the other for 5V. The two layers between a ground plane and a power plane are used for the long and/or high-speed routes. The placement of these signals between the two reference planes provides a relatively constant impedance (except for at plane boundaries) and the presence of both top and bottom ground planes in the stackup will minimize EMI

leakage from these signals.

Analog and Digital Domains

The analog and digital domains on the Hrafn PCB are separated for reduced coupling of digital noise onto the analog electronics. Both the ground and power planes are split and a single connection is made across the divide. Details of the power supply connection of the ground and power planes between the analog and digital sections are shown in Figure 8-10.

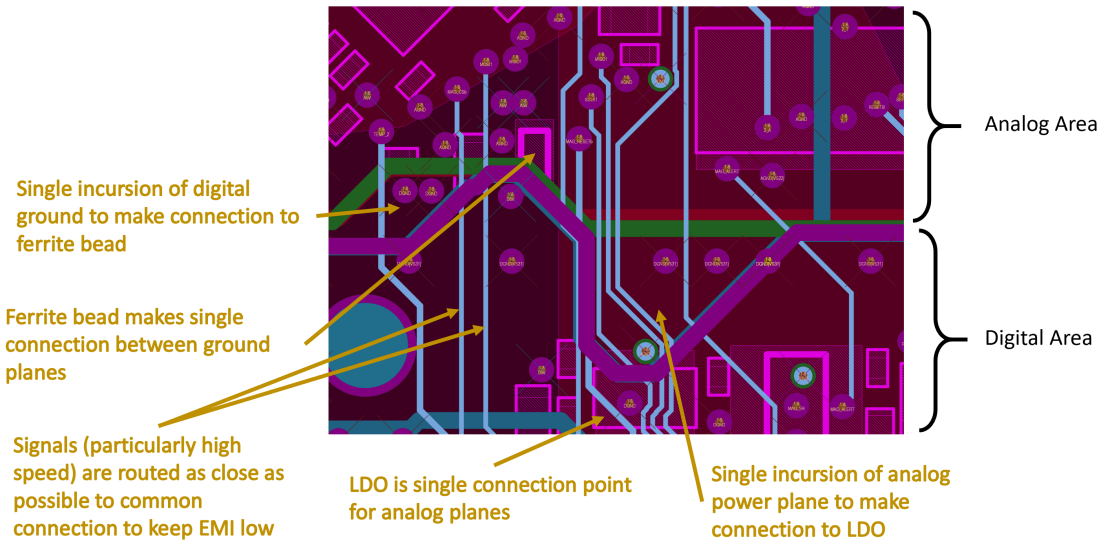

Figure 8-10: Connecting the digital Section to the analog section.

Magnetometer Area Layout

It is particularly important that layout around the magnetometer keep time-varying magnetic fields to a minimum. Magnetic fields fall quickly with distance (see Chapter 2), so the area immediately around the magnetometer is of critical importance. To achieve this, no traces are routed underneath the magnetometer, except the differential outputs whose currents are proportional to the magnetic signal. The current flowing through these traces is on the order of microamps and any perturbation caused

by these currents will be linear with magnetic field and therefore can be calibrated out together with the instrument sensitivity matrix (see Chapter 5).

The largest current which flows near the magnetometers is the bias current for the magnetometer itself. This current is static as long as the bias voltage and magnetometer sensor bridge resistances are static. The bias voltage comes from a precision shunt regulator with a 50 ppm/°C drift with temperature. Any change in resistance of the coils will also correspond to a temperature or ambient field effect and therefore should be calibrated out with the temperature dependence of the offset vector. To minimize the uncertainty of any non-linearity in the change in current used to bias the magnetometer, the ground and power planes are continuous underneath the magnetometer. While current may flow underneath the magnetometer, the distance invariance of magnetic fields created by large sheets of current causes the supply and return current paths to cancel. In contrast, if the planes are removed underneath the magnetometer, any imbalance in resistance on either side of the break will cause an effective current loop generating a relatively large magnetic field. Additionally, vias which bring the bias current into and out of the magnetometer are kept close to the magnetometer chip and are outside the footprint of the magnetometer (not under it) to keep distances from any possible magnetic source at a maximum. The power supply plane is split near the magnetometers so that the magnetometer bias voltage current can occupy an entire plane and so any power supply noise on the larger analog power supply plane is isolated from the magnetometers.

Other components are kept as far away from the magnetometer as possible. The closest other component is the temperature sensor which has microamp level current which is definitionally proportional to temperature. The next closest components are the small signal pre-amplifiers whose bias currents are on the order of microamps.

8.4 Mechanical Design[2]

The ASP is a standalone payload in its own aluminum enclosure. The enclosure provides mechanical support for the electronic components including the Hrafn and camera, and it also creates EMI shielding between the ASP electronics and the vector sensor payload.[3] The enclosure also provides for thermal dissipation from components within the ASP and secondarily creates an EMI shield between the digital and analog sections of Hrafn.

The external interfaces to the ASP enclosure are driven by the bus interface requirements. A CAD rendering with bus interface locations marked is provided in Figure 8-11.

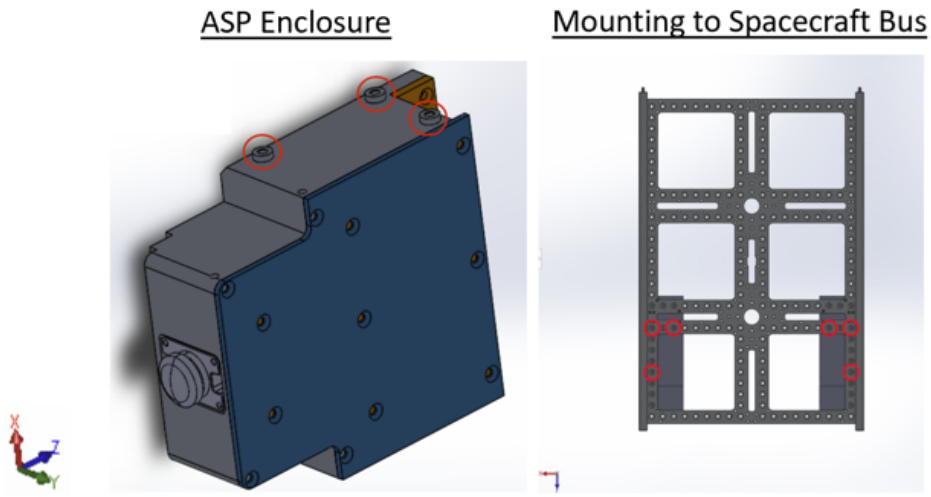

Figure 8-11: ASP enclosure mounting. Interfaces between the ASP enclosure and the mechanical bus are indicated with red circles in both pictures.

The main box of the enclosure is referred to as the "tub" and contains ledges which contact the Hrafn PCB metallization areas for mechanical support, thermal contact, and EMI sealing. An annotated CAD rendering of the ASP tub is provided in Figure

[2]The mechanical design was not primarily performed by the author of this thesis and is only briefly included here for completeness. I thank Cadence Payne for leading the design of the aluminum enclosure, and Dylan Goff and Cici Mao for valuable contributions as undergraduate researchers.

[3]This shielding is particularly important because the switch mode power supply on the Raspberry Pi is the only SMPS in the spacecraft *not* synchronized to the 800 kHz signal which is phased locked to the RF ADCs.

8-12.

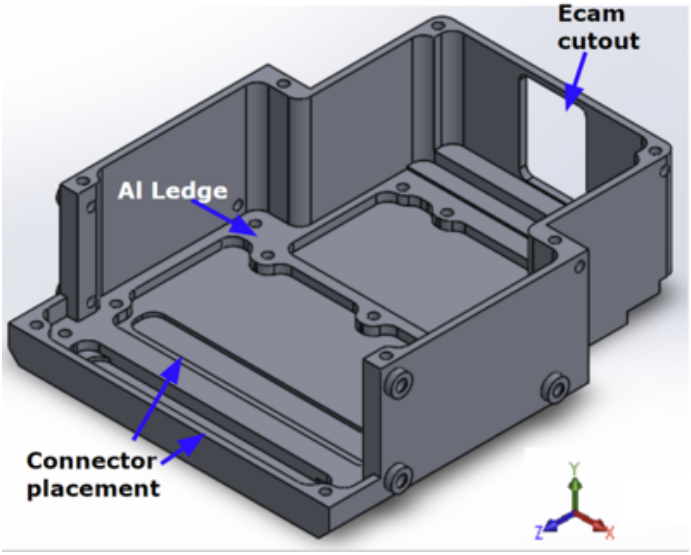

Figure 8-12: ASP enclosure tub. The aluminum ledge provides EMI sealing and thermal connection by contacting the metallization areas of the Hrafn PCB. The deeper cutouts in the tub provide spacing for the through-hole connector pins.

The tub also includes mounting points for aluminum shields which ensure that no EMI can leak out of the ASP enclosure and that minimal EMI can leak from the digital section of the Hrafn to the analog section. An annotated side view of the ASP enclosure to show placement of shields is provided in Figure 8-13.

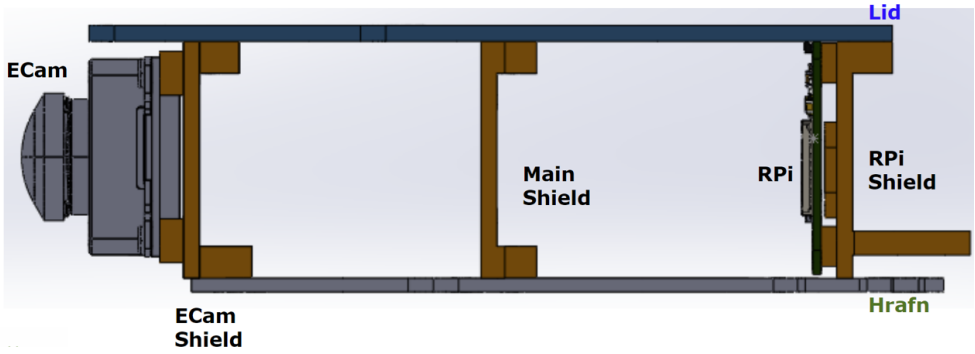

Figure 8-13: ASP enclosure shields.

8.5 Software Design[4]

8.5.1 Command and Telemetry Dictionary

The software system bridges the gap between functional hardware and satellite operations. With the Hrafn PCB manufactured and tested, we have hardware which is proven to be able to meet the requirements (such as described for magnetic sensing in Section 4.2). However, there is an additional level of abstraction needed before we can begin to operate the ASP payload as a "user".

We have formalized this abstraction by writing a command and telemetry dictionary which defines every activity which we might request the ASP to perform and defines every bit of data we can bring back from the ASP. After hardware bring-up testing, we already have drivers or application programming interfaces (APIs) for the major components on the Hrafn. Therefore, the remaining software design connects each command and telemetry value to the correct hardware subsystem and associated API.

8.5.2 Software Block Diagram

The desired software functionality is broken up into major functions which interact with each other through limited interfaces. The abstraction represented in Figure 8-14 is used to identify separate modules, which became separate files (or a set of separate files). In the language of Python development, many of the modules are a Python class implementing an abstraction of their underlying hardware. Every activity in the command dictionary maps to one of the functions in the module class. Therefore, the main software loop only needs to parse the incoming command, and call the appropriate class function in the correct module. Many of the activities which might be called from the main loop take several minutes to complete (such as a 500

[4]The author wrote much of the low-level drivers for hardware like the ADCs. The author recognizes undergraduate researcher Luc Cot for writing file management and command processing software and the author thanks Dr. Alvar Saenz-Otero for assistance with the CubeSat Space Protocol and general software development mentoring. The software discussion here will be kept short and is intended only to provide context for the rest of the ASP payload design.

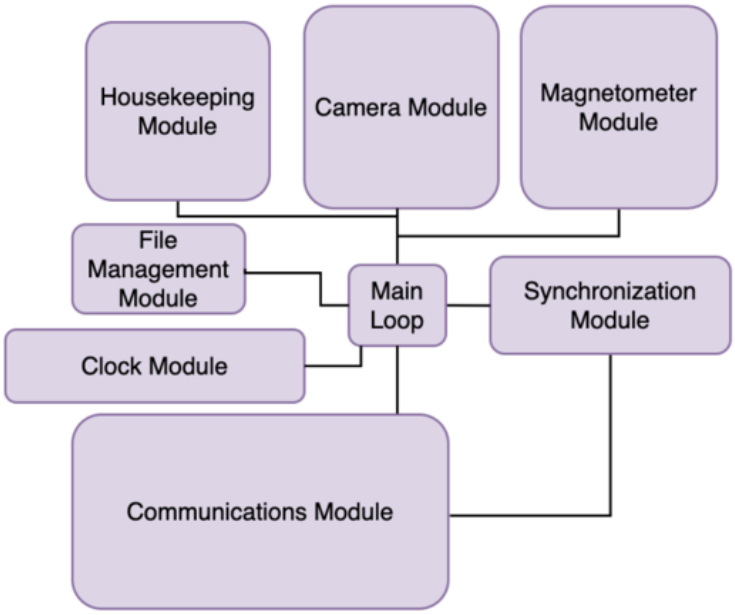

Figure 8-14: Software block diagram.

second collection sequence of magnetometer data), so the module function spins off a separate thread to complete the task, allowing the main software loop to process other commands and perform other activities.

8.5.3 Linux Configuration

The software is developed on the Raspberry Pi Zero in the Raspbian operating system.[5] Device trees which come with Raspbian are available for the W5500 Ethernet controller and the MCP2515 CAN controller. The devices are enabled by editing the `/boot/config.txt` file to include the overlays.[6] We have also enabled the second SPI bus with two chip select lines for use with the magnetometer ADC and the housekeeping ADC.

[5]We have frozen development with Raspbian Buster with Linux kernel V4.19. At the time of writing, this is available at: `https://downloads.raspberrypi.org/raspbian/images/raspbian-2019-07-12/`.

[6]A helpful list of Raspbian overlays with definitions of optional parameters is provided at the following link: `https://raw.githubusercontent.com/raspberrypi/firmware/master/boot/overlays/README`.

8.6 Summary

This chapter covered the payload design surrounding the magnetic sensing system. The Auxiliary Sensor Package (ASP) is a standalone payload inside the spacecraft bus which can be operated independently from the main Vector Sensor payload. The ASP provides contextual data to aid in the analysis of the science data from the Vector Sensor. A custom PCB (Hrafn) was designed and fabricated; this PCB includes both the implementation of the magnetic sensing system described in Chapter 7 and supporting electronics including a Raspberry Pi Zero as the payload computer. All ASP components are housed in an aluminum enclosure approximately 1/3 U in volume. The software residing on the Raspberry Pi implements a command and telemetry dictionary to abstract hardware complexity away into a simple interface for payload operation.

Chapter 9

Conclusion

We conclude this thesis by summarizing the key findings and reviewing the content from each chapter. We end by discussing avenues for future work in the three categories: a general AMR sensor design for future satellite missions, the future plans for the Auxiliary Sensor Package, and the application of our calibration implementation.

9.1 Summary

This thesis covers an array of topics related to the design, implementation, and integration of a magnetic sensor with 100 nT precision and repeatability for the AERO-VISTA CubeSat mission.

In **Chapter 2** we use analysis from first principles to derive a suite of interference estimation techniques. These estimates covered both material and current path interference effects and focused on quick "good enough" metrics over precision. These can be used by any future mission to conduct initial magnetic screening by analysis. We used these together with ground testing measurements in Chapter 6 to make a best-effort magnetic cleanliness campaign with limited time and resources.

Chapter 3 describes the magnetic cleanliness campaigns reported in the literature for other missions. We extract key lessons learned and identify how to tailor and apply their approach to a mission like AERO-VISTA. This chapter should be useful to anyone interested in reviewing magnetic cleanliness efforts with an emphasis on

creating their own "good enough" strategy.

In **Chapter 4** we discuss how the parameterization of magnetic performance in requirements is not always the same as on datasheets, and describe how we reconcile these two parameterizations for our selected magnetometer. We then measure the error contributions from each of the magnetometer non-ideal effects to show that with some calibration we will meet the mission requirements of 100 nT precision and repeatability.

Chapter 5 combines the non-ideal effects from Chapter 4 to create a single measurement equation which includes the contributions from identified sources of significant error. We show that interference from either magnetically hard or soft materials does not create any new unknown terms in the measurement equation. We then describe how current path interference can be added to the calibration regression if housekeeping telemetry is available. We end by describing how we have implemented this calibration method in Python.

Chapter 6 describes how we conduct magnetometer verification and magnetic screening on the ground without access to a dedicated magnetic test facility. These methods can be used by any CubeSat builder to estimate magnetic parameters with only a smart phone as a magnetometer.

Chapter 7 documents our magnetometer design in detail. We start with a block diagram and selection of major components. We create a detailed error budget with noise contributions from all major components. Next, we describe the design details of the schematic and PCB layout. We end with measured data including an analysis of the AMR sensor's set/reset polarity switching functionality.

In **Chapter 8** we describe how the magnetometer design of Chapter 7 is implemented in the Auxiliary Sensor Package (ASP). We describe the interfaces with the spacecraft bus, provide a detailed electronic design, describe the mechanical design, and discuss software development.

9.2 Thesis Contribution

The design approach and implementation presented in this thesis meets the magnetic sensing requirements for the AERO-VISTA mission. The magnetometer prototype (MagEval) meets our measurement requirement with our proposed calibration method (see Section 5.1). In ground testing we find that the spacecraft bus does not create magnetic fields that will impact our measurement ability (see Section 6.3). Components which might create magnetic uncertainty are screened. This includes completely analytical triaging as described in Chapter 2, and measurements as described in Chapter 6. We expect our methods will meet mission requirements.

We developed a flight form-factor implementation of the magnetometer system (and imager) and packaged the design with an aluminum enclosure as described in Chapter 8.

9.3 Future Work

9.3.1 AMR Sensor Package Design

The AMR sensor package implementation is capable of repeatable measurements to better than 100 nT in the presence of the environmental variation expected on orbit. This design can be implemented on future missions that need greater performance than what can be found in other COTS technologies, but do not want the cost or complexity of fluxgate or search coil magnetometers.

One possible application is in mapping the crustal remnant fields on the Moon or Mars. In particular, the small size, weight, and power together with high effective bandwidth could make a magnetometer of this design useful for magnetic mapping with flight vehicles such as a follow up to the Ingenuity Mars Helicopter [82].

Planetary exploration applications may benefit from increased precision, even if it comes at the expense of more power. This could be achieved with only a small change to the design presented in this thesis, by increasing the bias voltage to the AMR magnetometer. This will increase the signal for a given incident field, increasing the

signal to noise ratio. This design can also be implemented on a less-integrated PCB than was developed for the AERO-VISTA ASP. Other mission application designs could be significantly smaller and less power-hungry the our Hrafn design if they do not need to support the Raspberry Pi computer and complex digital interfaces.

9.3.2 AERO-VISTA ASP

In this thesis we conduct magnetic calibration tests with the engineering test unit (MagEval) and perform initial noise analysis with the engineering model. In the future, we expect to perform magnetic testing with the integrated ASP unit. If the integration schedule allows, we will also perform limited magnetic measurement performance testing with the ASP modules integrated into the spacecraft.

9.3.3 Calibration

Chapter 5 describes our Python implementation of the magnetic calibration measurement equation. This software will be used for AERO-VISTA magnetometer verification and flight instrument data processing, but we believe that the same magnetic calibration procedure and software can be useful for instruments on other programs as well. We plan to open source this software and continue to make it more user friendly and generally applicable. This will include integration into a ground data processing pipeline for the evaluation of the scientific data from the AERO-VISTA mission. In the near future, we hope to combine the demonstrated instrument calibration with the fitting of interfering sources as described in Section 5.2. At a minimum, we plan to try fitting some of the housekeeping current data to magnetometer measurements with the AERO-VISTA spacecraft while they are in orbit.

Appendix A

Magnetometer Test Hardware

This appendix describes in more detail some of the prototype and test hardware that was developed along the way to the final EM design described in Chapters 7 and 8. This hardware is grouped into two categories. The first is hardware which was primarily designed to provide measurements of magnetic fields for screening and noise characterization purposes; these are discussed in Section A.1. The second group is hardware which prototyped a part of the Hrafn PCB (see Section 8.3) to increase the chance that the final EM design worked with minimal errors; these are discussed in Section A.2.

A.1 Measurement and Characterization Hardware

The primary hardware used for magnetic characterization (besides cell phone magnetometers described in Section 6.4) are based on the PNI RM3100. This magnetometer provides comparable performance to the HMC1053 magnetometer used for the AERO-VISTA project, but the interface is considerably simpler, needing only a digital SPI or I2C readout with no careful custom analog and mixed signal design. Additionally, the price of $50 is also comparable to the AMR sensors we have designed with for AERO-VISTA.[1] While some early screening was performed with a simple Arduino-

[1]See Appendix D for EMI measurement of the RM3100 and why we ultimately chose a different magnetometer for AERO-VISTA.

like microcontroller (a Teensy 3.2 [83]) as pictured in D-1, ultimately a custom PCB implementation of the microcontroller and RM3100 magnetometer was developed as discussed in Section A.1.1.

A.1.1 Helmholtz Cage Electronics

An implementation of analog control electronics for interfacing to MIT's Space Systems Lab (SSL) Helmholtz Cage [68] was developed to aid in magnetic testing, and these electronics proved useful for other magnetic screening and testing.

The implementation of the Helmholtz cage electronics uses a modular architecture with large numbers of coil driver circuits and RM3100 sensor implementations available by stacking up multiple identical boards [84]. This implementation is configurable for many Helmholtz cages which use analog amplifiers which work down to DC, but even beyond Helmholtz cage control, the abstraction of multiple RM3100 magnetometers into a system which can simply be plugged into a PC by USB and operated over a Serial communications port was useful in multiple ground measurement and screening efforts. For example, the Helmholtz cage electronics were used for all magnetic noise characterization measurements reported in Appendix C.

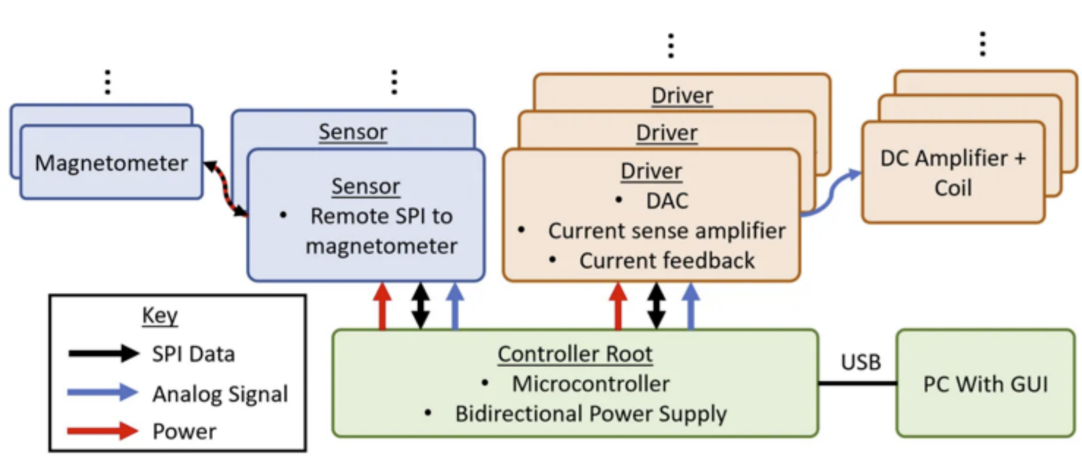

Figure A-1: Helmholtz cage electronics block diagram.

The implementation of the magnetic sensing for the Helmholtz cage electronics is particularly convenient because the RM3100 sensors themselves are on small low-

power sensor boards and connected to the main microcontroller over an Ethernet cable of arbitrary length. Additionally, the data from each of the magnetometers connected to this system is collected synchronously by the microcontroller so the host computer program does not need to worry about collating and synchronizing data from multiple sensors, reducing the amount of data wrangling needed before a useful plot can be generated.

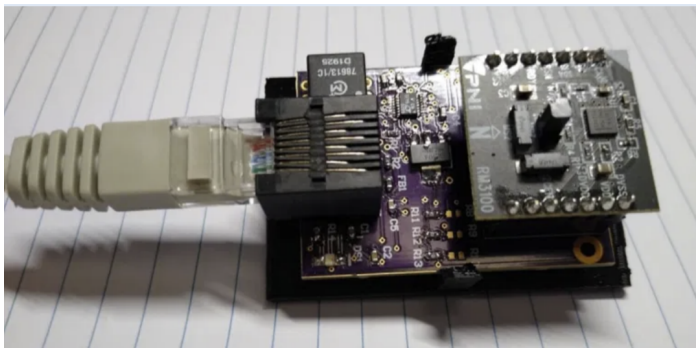

Figure A-2: Helmholtz cage electronics sensor implementation.

A.2 Prototyping Hardware

The hardware described in this section increased our chances of designing a working engineering model of the Hrafn the first time. This was desirable because the fabrication and population of the custom PCBs was a significant project expense.

A.2.1 MagEval

The "MagEval" board is an implementation of the analog processing electronics surrounding the HMC1053 which was used also for measurement requirements verification testing as described in Section 4.4.2. Measurements made on this platform led to the development of the calibration method described in Chapter 5.

MagEval uses two RM3100 magnetometers as built-in reference options, and implements analog processing electronics around a single HMC1053 magnetometer (the

"test" magnetometer). We designed a 3D printed mount for the MagEval PCB which included a slot for the sensor probe of a FVM400 reference magnetometer (see Figure A-4). This reference magnetometer was used to determine the "true" local magnetic field against which measurements by MagEval's test magnetometer were compared. These two data sources were used for all testing described in Section 4.4.2 which led to the results shown in Section 5.1. In MagEval, the analog pre-amplifiers are built with MAX9618 op-amps. Formal analysis of spectral noise contributions led us to ultimately select the LMP2022 op-amp for the EM design (see Section 7.4 for noise calculations), but even without this improvement, we were able to meet our measurement requirements, and the same pseudo-differential amplifier topology was used for both MagEval and the EM.[2]

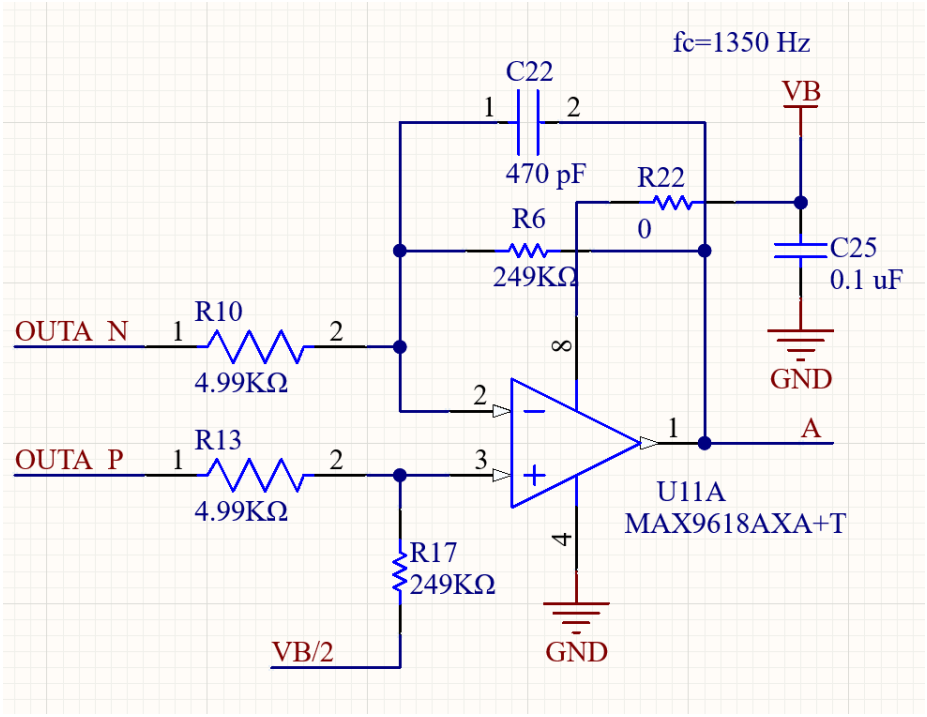

Figure A-3: MagEval implementation of a pseudo-differential amplifier with op-amps.

MagEval used the AD1248 8-channel ADC. Working one channel at a time, this ADC met our performance goals, but this ADC chip is only a single ADC circuit

[2]We also considered more highly-integrated instrumentation amplifiers but found that these were optimized for higher frequency performance and that better low frequency (0.1 to 10 Hz) performance was achieved with this pseudo-differential topology which could make use of the very low flicker frequency of chopper-stabilized op-amps.

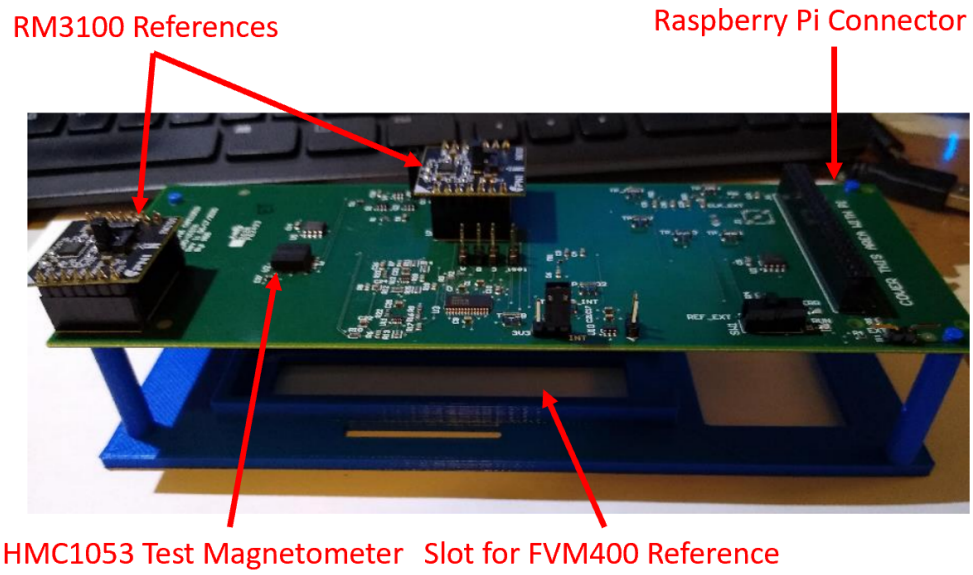

Figure A-4: Annotated picture of MagEval on its 3D-printed carrier.

with an 8-to-1 multiplexer to sample multiple channels. This required that we set a relatively large sampling rate of 80 SPS while only effectively sampling each channel of data 10 times per second. This operating mode allowed us to show that this implementation and magnetometer meet requirements, but we learned from this trade off and selected a true 8-circuit 8-channel ADC for the Engineering Model (the AD7771).

MagEval also served as a valuable prototype for developing low-latency SPI and GPIO interfaces to ADCs and other PCB-specific hardware, and the general architecture of first abstracting the ADC into an ADC driver Python class and then abstracting the driver Python class into a desired-functionality Python class is the same abstraction technique we used for low level software development for the EM as described in Section 8.5.

A.2.2 AD777x_test

The AD777x_test[3] provides an implementation of the AD7771 ADC to find any hardware bugs before implementation on the Hrafn. As discussed in A.2.1, we needed

[3]The x in the name represents a last minute change from the AD7779 to the AD7771 due to component availability issues. Fortunately, these components are pin and register identical with only minor differences in mixed signal performance parameters differentiating the two.

to change ADCs between MagEval and the Hrafn EM, and the design around the ADC is fairly complex with dozens of supporting discrete components. We tried some prototyping with the manufacturer's evaluation board[4] but found that connecting the ADC to an external signal processing device like the Raspberry Pi was not the primary use case for the evaluation board, and that both hardware and documentation did not natively support our application. Instead, we designed and fabricated a simple evaluation module of our own. The AD777x_test has all the electrical interfaces of the AD7771 implementation on the Hrafn EM, but none of the careful routing.[5] As a last minute addition, we also added on a single HMC1053 magnetometer and analog channel to test this connection as well.

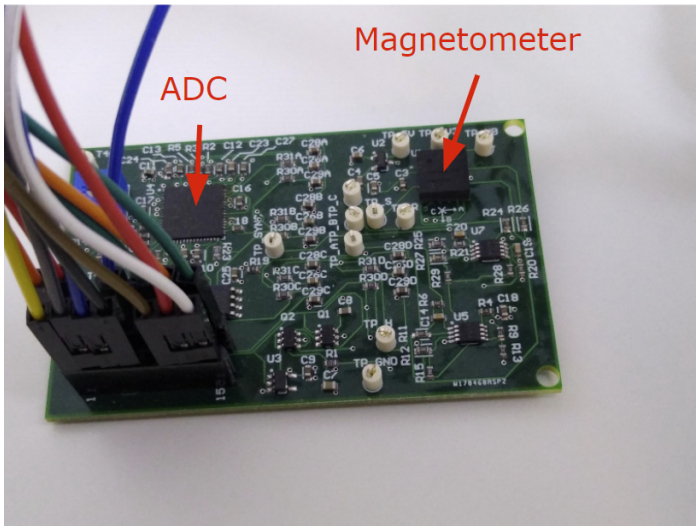

Figure A-5: Annotated picture of AD777x_test.

In testing with the AD777x_test PCB, for several weeks we were not able to get the ADC to read sensible results. While the SPI interface appeared to work fine, the ADC conversion values were nearly always saturated. We discovered that the AD7771 internal reference "output" buffer needs to be powered on to use the internal buffer internally (even if you aren't actually trying to use the buffer output pin). This is fixed by *setting* bit 4 of the register GENERAL_USER_CONFIG_1.

[4]The EVAL-7770-7771-7779 with details available here: https://www.analog.com/en/design-center/evaluation-hardware-and-software/evaluation-boards-kits/eval-ad7770-ad7779.html

[5]In fact, this is the only PCB discussed in this thesis which was primarily routed by the Altium auto-router.

Making matters even more confusing, this bit is a power-*down* function, but one which operates with *negative* logic.[6] This did not necessitate a change of the Hrafn PCB, but it was good to know about this configuration complexity before attempting bring-up testing of the full Hrafn PCB.

A.2.3 ASPIT

The ASPIT is the Auxiliary Sensor Package Interface Tester, and is a partial "flat-sat." The idea behind a flat-sat is to create all the electronics and interfaces of the actual flight hardware, but to spread it out into an easy-to-debug and modular form factor. The ASPIT is not truly a flat-sat as it lacks some of the housekeeping sensors and interface electronics (e.g. LVDS timing signals) that are on the true ASP. It also used a ENC28J60 Ethernet interface module, but the ASP had to switch to the W5500 at the last minute due to supply chain problems.

The primary goal of the ASPIT is to reduce risk of major issues with the ASP Engineering Model. All ASPIT components together cost less than a few hundred dollars, while a full spin of the ASP engineering models costs several thousand, so with even a small chance of finding one problem, the extra step of the ASPIT is a good investment. Secondarily, the ASPIT provided a platform for early software development and test while the ASP units were undergoing final design and fabrication.

We did not make significant design changes to the EM as a result of ASPIT testing. However, we did discover that due to the configuration of the Ethernet and CAN controller device trees in Raspbian, it is easier to leave both these devices on SPI bus 0. Therefore the housekeeping and magnetometer ADCs are connected to SPI bus 1. Finding this preference with the ASPIT likely saved some Linux configuration effort for EM software development.

[6]The author thanks the Analog Devices technical support staff for patiently working with us despite our very low sales volume.

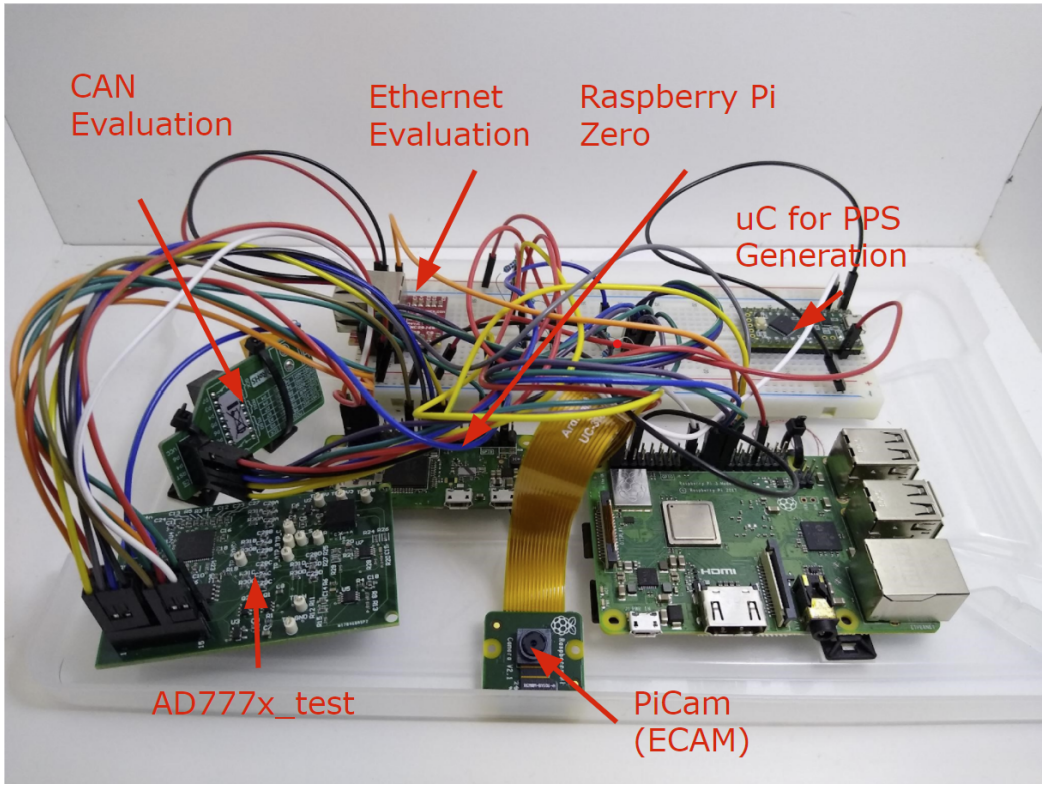

Figure A-6: Annotated picture of the ASPIT.

Appendix B

Numerical Simulation of Magnetic Fields

This appendix describes how we simulated the expected magnetic field numerically for geometries which are complicated enough that the Biot-Savart integral becomes intractable. See Chapter 2 for the application of these simulations to evaluate simpler approximation equations.

B.1 Current Path Simulation

The magnetic field from complicated current paths is computed numerically by splitting up the current path into small finite elements. In this work the small finite elements are defined manually in a custom MATLAB script, although there are existing tools to perform this for more complex shapes, such as those which might be imported from CAD designs.[1]

In our implementation, each small element is defined by the 3-space position of the start of the current element, the end of the current element, and the current flowing through the segment. By defining many small segments which connect tail-to-tip, we can approximate a complex and arbitrary shape. The magnetic field at a measurement location is calculated as in Eq. (B.1), which comes from Eq. (2.5).

[1]See for example: https://www.femm.info/wiki/HomePage

$$d\vec{B} = \frac{\mu_0}{4\pi}(d\vec{l} \times \vec{r})/(|r|)^3 \tag{B.1}$$

The computed magnetic field is a differential contribution for the differential path length dl. By simply summing over all small path contributions, the total magnetic field at the measurement location is determined. The entire process is repeated to determine the magnetic field at multiple measurement locations as is done in generating plots such as those found in Chapter 2.

B.2 Material Shape Simulation

When simulating the magnetic contribution from an arbitrary shape, the shape is broken into finite elements each with a magnetic dipole moment. Each element is defined by the location of its center in 3-space, and its 3-dimensional vector magnetic moment. The magnetic field at a measurement location created by one element is given by Eq. (2.1), repeated here as Eq. (B.2).

$$d\vec{B} = \frac{\mu_0}{4\pi}\left[\frac{3\hat{r}(d\vec{m}\cdot\hat{r}) - d\vec{m}}{r^3}\right] \tag{B.2}$$

In our material simulation, Eq. (B.2) is solved for each differential moment contribution at a measurement location, and the contributions from each element are summed to determine the total magnetic field. The entire process is repeated to determine the magnetic field at multiple measurement locations as is done in generating plots such as those found in Chapter 2.

Appendix C

Environmental Noise Characterization Testing

This appendix describes how we have measured the environmental noise at some characteristic measurement locations. The noise at each location does appear to change with time of day so the single measurement here may not be completely representative. However, we argue that even the single screening measurement presented here will allow us to make broad comparisons about where magnetic measurements need to be conducted to achieve a given noise floor. Additionally, the reader can duplicate our measurement methods to perform their own screening at whatever location and time is appropriate for their testing needs.

C.1 Magnetic Noise Determination Method

C.1.1 Magnetic Measurement Devices

We used two RM3100 magnetometers and the open source Helmholtz Cage electronics developed by the author and discussed in more detail in Section A.1.1. These magnetometers are read with an approximately 3 ms period and have a noise floor uncertainty of about 20 nT.

The magnetometers are held firmly in place by a 3D printed mount designed to

slot into standard 8020 aluminum extrusion (see Figure C-1). The magnetometers are held in fixed orientation at 0.5 meters apart on this aluminum extrusion. This distance is chosen as it is a typical distance from which one might measure small satellite subsystems when using the dipole approximation. The aluminum extrusion is held away from the floor or table on small PVC pipe legs. This prevents extremely local perturbations from devices embedded in the floor or wall from interfering with the measurement. If a given magnetic measurement is to be made directly on a given table this step should be skipped to gather a representative magnetic characterization.

C.1.2 Data Collection Software

The microcontroller program uses the Helmholtz cage electronics to forward the measurement from each magnetometer to the host computer over the host computer's serial port. Due to the finite refresh rate of the magnetometer, the microcontroller is programmed to pause for 3 ms between each measurement. This results in a fixed sample period of slightly over 3 ms. Each measurement batch collects 10,000 data points (approximately 30 seconds of collection) and is triggered with any sent character from the host computer.

The software on the host computer provides a user interface for the microcontroller. The program prompts the user to reorient the measurement device to measure the magnetic gradient of three orthogonal directions, provokes the microcontroller into beginning a magnetic measurement, and saves the data to series of `.csv` files for later processing. These could be viewed in a program like Excel, but in this report, these data files are automatically processed by another plotting script described in Section C.1.4.

C.1.3 Magnetic Measurement Procedure

The measurement is made in three parts, one measure each along three orthogonal axes at the measurement location. Each measurement is prompted for by the Python program running on the host computer. This data is saved to a newly created folder,

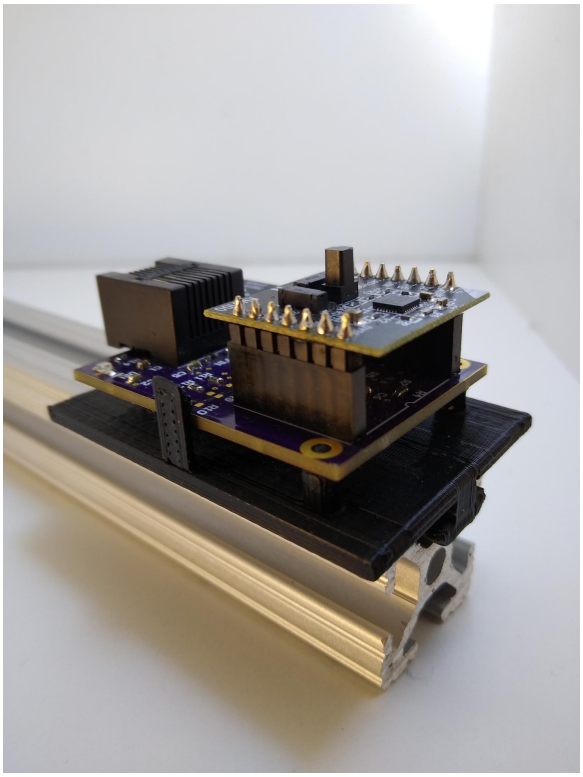

Figure C-1: 3D Printed structure holds the Helmholtz cage implementation of the RM3100 in fixed orientation on extruded 8020 aluminum.

which is named based on user input. The program also prompts for a brief description of the measurement location which is saved in the data folder in a separate text file for documentation.

C.1.4 Processing and Viewing the Magnetic Data

The first way to visualize this data is a simple time-domain plot of the magnetic field over time of the measurements from one of the magnetometers in all three axes. This shows which axis might be particularly noisy and is easy to parse visually into an approximate noise floor. Another way to visualize the data from a single magnetometer is to take the power spectral density of the signal from each axis, showing where in frequency space the noise is located. This can show how magnetic measurements of different bandwidths can have different noise floors in the same magnetic environment.

Beyond the measurements from the single magnetometer, it is desirable to know

Figure C-2: Capturing "X"-gradient data.

Figure C-3: Capturing "Y"-gradient data.

Figure C-4: Capturing "Z"-gradient data.

how the magnetic measurement at one location might predict the magnetic measurement at another nearby location. This describes the uncertainty of the magnetic gradient due to environmental variation or other noise. In our procedure, we measure the variation of three orthogonal magnetic field components along three different orthogonal orientations as represented in matrix form in Eq. (C.1).

$$\begin{bmatrix} \frac{\partial B_x}{\partial x} & \frac{\partial B_y}{\partial x} & \frac{\partial B_z}{\partial x} \\ \frac{\partial B_x}{\partial y} & \frac{\partial B_y}{\partial y} & \frac{\partial B_z}{\partial y} \\ \frac{\partial B_x}{\partial z} & \frac{\partial B_y}{\partial z} & \frac{\partial B_z}{\partial z} \end{bmatrix} \tag{C.1}$$

With each orientation of the measurement apparatus, we are measuring a two-point estimate of the gradient in a particular direction. Each orientation provides one of the rows in Eq. (C.1). We could plot in time and frequency domain every value of the matrix at every location, but to reduce visual clutter we have decided to instead plot the entire vector gradient only along one axis (notionally the X-axis) and to also summarize the gradients along each other axes through a vector sum (norm) of the three vector components.

The uncertainty of any magnetic measurement depends on the bandwidth of that measurement. Noise at higher frequencies such as 60 Hz power-line noise may be important for fast sample rates, but can be safely ignored for much slower measure-

ments. For the sake of making a single point comparison between the noise in different magnetic environments, each measurement described has also been low-pass filtered with a 5th order Butterworth digital filter with a cutoff frequency of 10 Hz before the rms noise is computed and reported in Table 4.1. This frequency was selected as it is the required measurement rate for the AERO-VISTA mission.

C.1.5 Noise Measurements in Characteristic Locations

To understand where magnetic measurement noise may be "quiet enough" for a given measurement, we have made magnetic noise measurements in some locations that might be a available to an low cost CubeSat mission. These locations were selected to search for an optimal mix of low magnetic noise, with ease of access. The locations we measured are described in Table C.1.

Table C.1: Magnetic noise measurement locations.

Location Name	Detailed Description	Possible interferers
Urban Campus Office Space	MIT building 37 3rd floor office	Subway system, elevator
Urban Campus Lab Space	MIT Space Systems Lab (SSL), 3rd floor of building 37	Subway system, elevator, lab equipment
Urban Residence	Kitchen in Somerville, MA near Davis Square	Subway system, appliances
Residential Outdoors	Outdoor patio in Somerville, MA near Davis Square	Subway system
Suburban Office Indoors	Office space in Danvers, MA near Massachusetts Route 128	Highway, office electronics
Suburban Office Outdoors	Outside office space in Danvers, MA near Massachusetts Route 128	Highway, office electronics
Rural Lab	Inside MIT Haystack Observatory facilities	Observatory equipment and associated power lines
Rural Lab Outdoors	About 10 meters from the MIT Haystack Observatory buildings	Observatory equipment and associated power lines
Rural parking lot	Small town parking lot, about 30 meters from any building. GPS coordinates: [41.932667, -70.811333]	Cars driving by, power lines

C.2 Results

In this section we provide detailed plots of magnetic noise for each location and tabularize a summary of these findings in a 10 Hz measurement bandwidth in Table C.2.

Table C.2: Magnetic noise results table.

	Noise in nTrms[1] for [X, Y, Z]-axes			
Location	One Magnetometer	Two magnetometer gradient vector	Two magnetometer gradient magnitude over orientation	Figures
Urban Campus Office Space	[14, 7, 107]	[8, 10, 10]	[17, 47, 19]	C-5, C-6
Urban Campus Lab Space	[26, 19, 63]	[8, 13, 12]	[20, 74, 16]	C-7, C-8
Urban Residence	[17, 127, 360]	[10, 19, 17]	[28, 22, 23]	C-9, C-10
Residential Outdoors	[93, 336, 1027]	[12, 41, 17]	[46, 22, 16]	C-11, C-12
Suburban Office Indoors	[5, 7, 5]	[8, 9, 9]	[15, 15, 17]	C-13, C-14
Suburban Office Outdoors	[6, 12, 8]	[9, 11, 8]	[17, 16, 18]	C-15, C-16
Rural Lab	[10, 14, 18]	[11, 20, 22]	[32, 122, 16]	C-17, C-18
Rural Lab Outdoors	[61, 20, 25]	[16, 16, 12]	[26, 23, 17]	C-19, C-20
Rural parking lot	[16, 18, 13]	[10, 9, 8]	[16, 15, 18]	C-21, C-22

[1] The static value for every measurement is subtracted and the signal is low pass filtered to 10 Hz. This table reports the rms value after these steps.

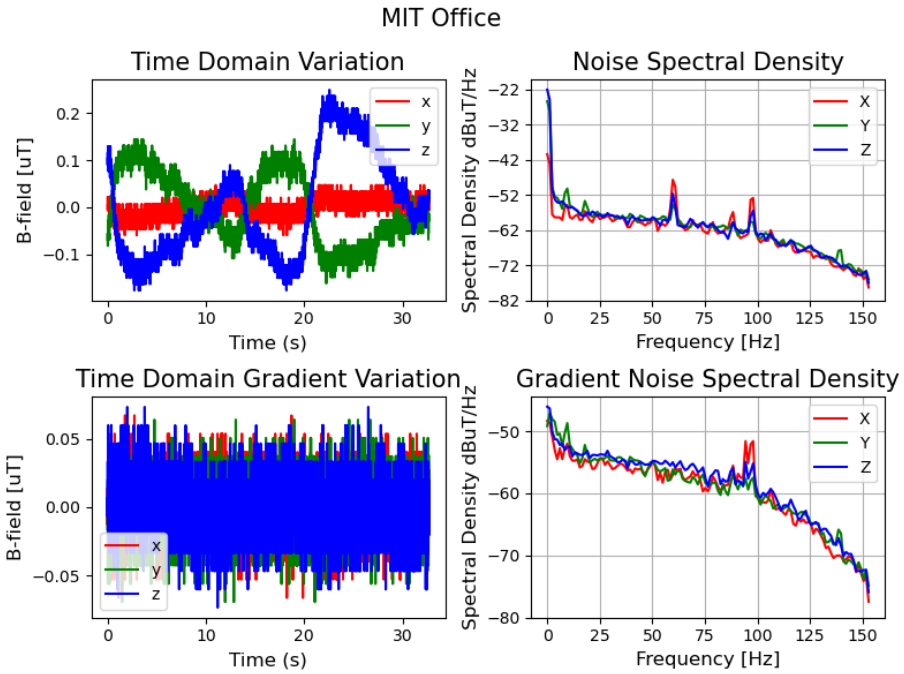

Figure C-5: Location: Urban campus office space. Time and frequency domain plotting of a single magnetometer measurement and the gradient along the X-direction.

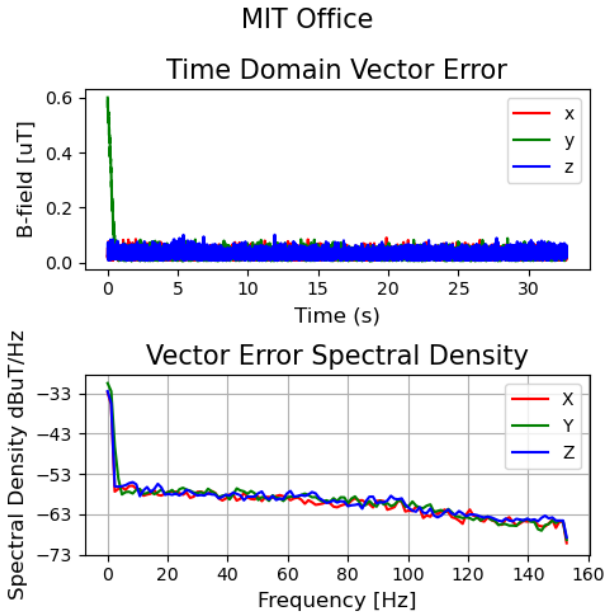

Figure C-6: Location: Urban campus office space. Magnitude of the gradient noise along three orthogonal directions.

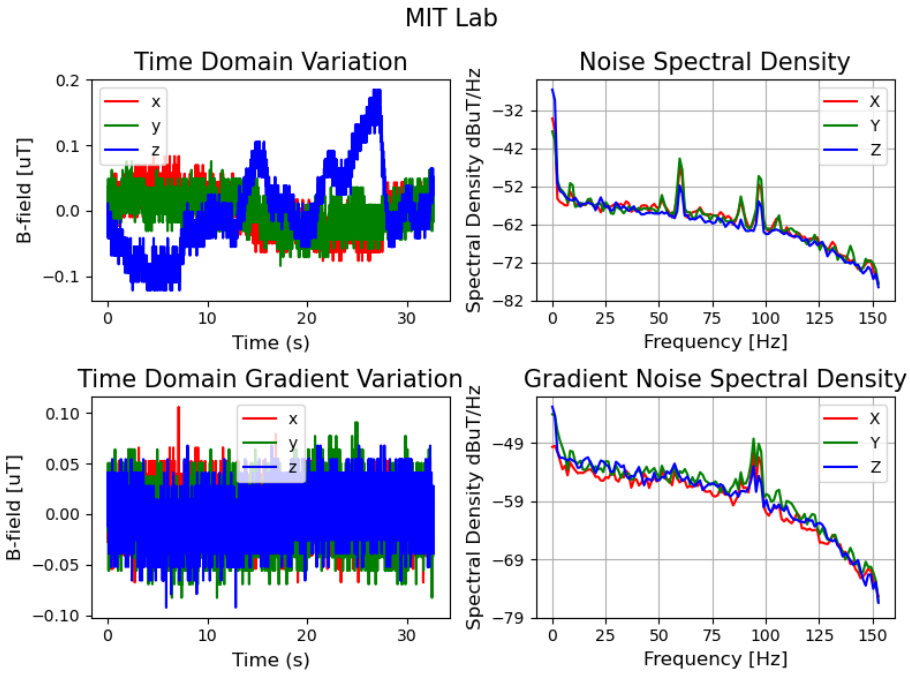

Figure C-7: Location: Urban campus lab space. Time and frequency domain plotting of a single magnetometer measurement and the gradient along the X-direction.

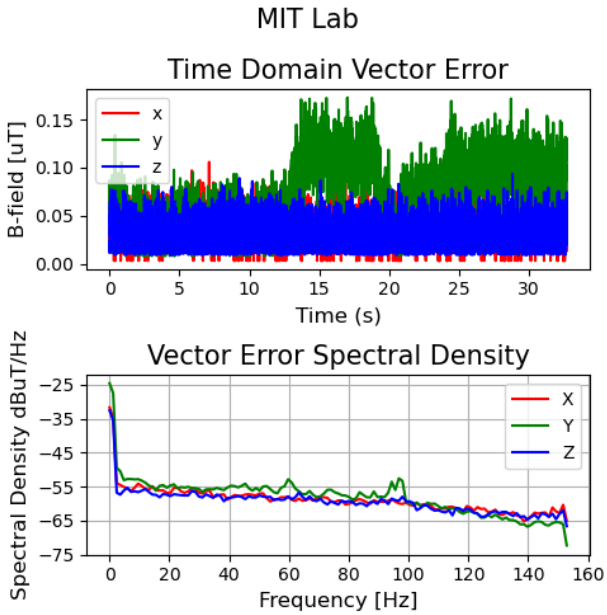

Figure C-8: Location: Urban campus lab space. Magnitude of the gradient noise along three orthogonal directions.

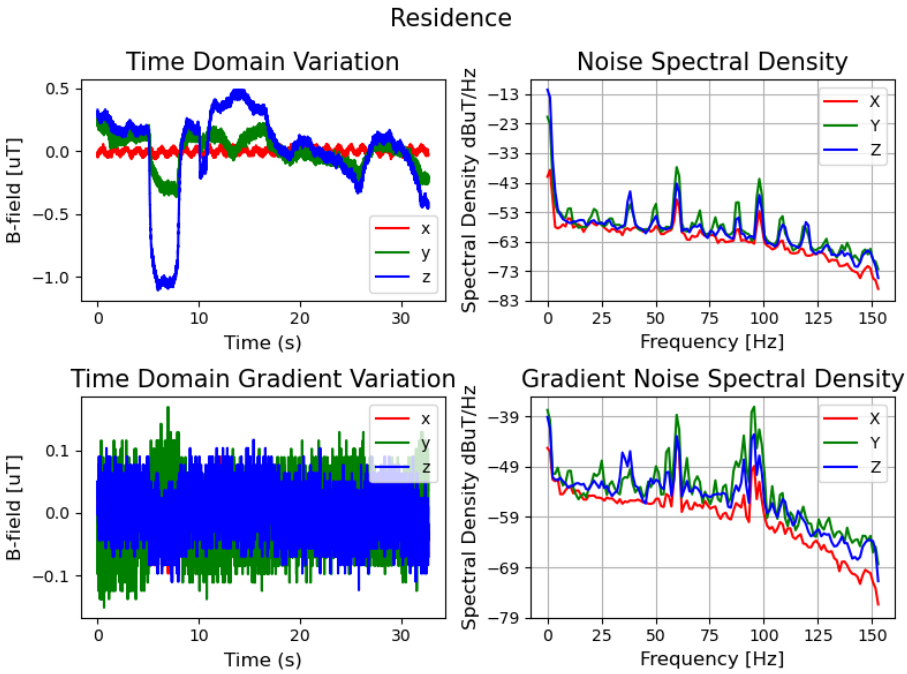

Figure C-9: Location: Urban residence. Time and frequency domain plotting of a single magnetometer measurement and the gradient along the X-direction.

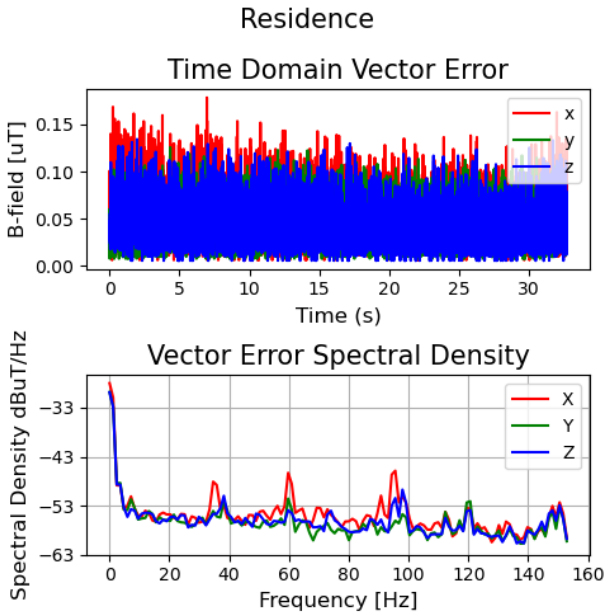

Figure C-10: Location: Urban residence. Magnitude of the gradient noise along three orthogonal directions.

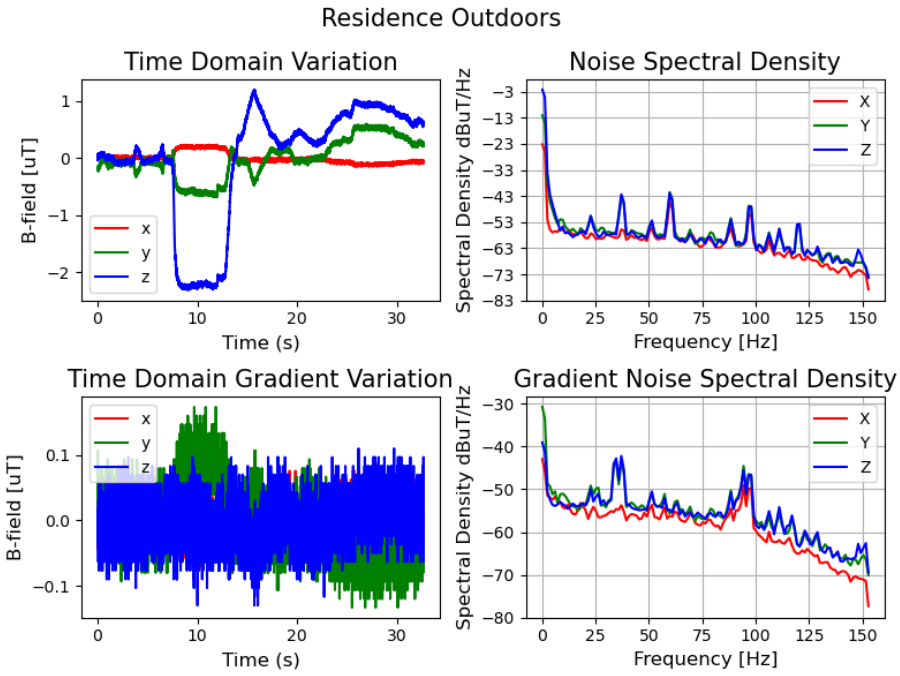

Figure C-11: Location: Urban residence outdoors. Time and frequency domain plotting of a single magnetometer measurement and the gradient along the X-direction.

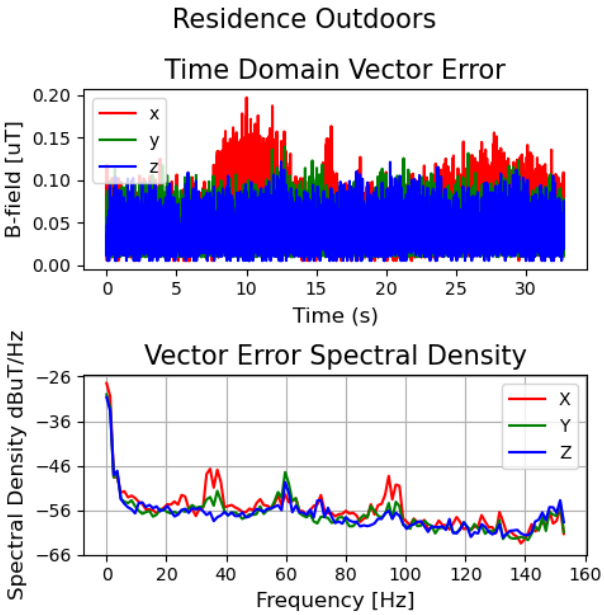

Figure C-12: Location: Urban residence outdoors. Magnitude of the gradient noise along three orthogonal directions.

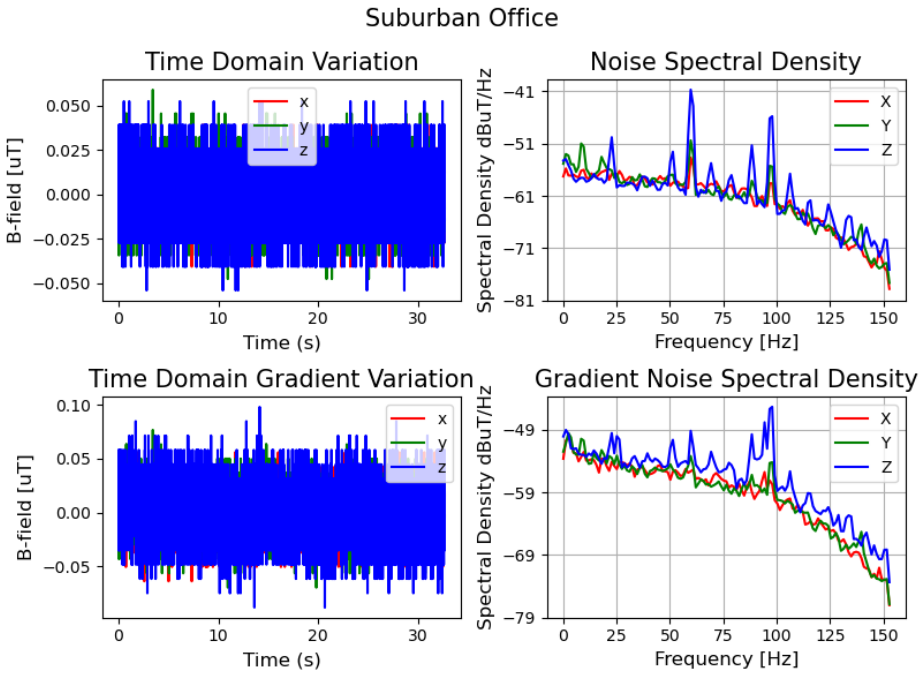

Figure C-13: Location: Suburban office indoors. Time and frequency domain plotting of a single magnetometer measurement and the gradient along the X-direction.

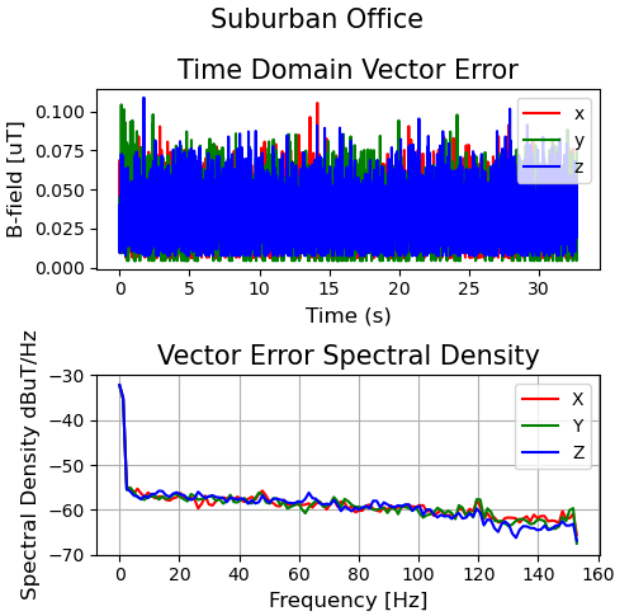

Figure C-14: Location: Suburban office indoors. Magnitude of the gradient noise along three orthogonal directions.

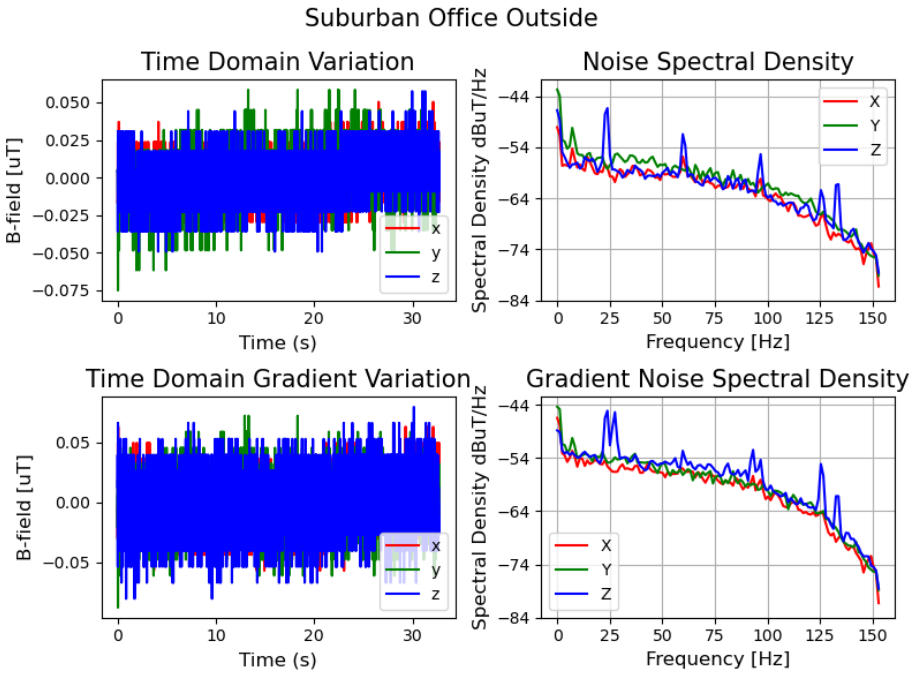

Figure C-15: Location: Suburban office outdoors. Time and frequency domain plotting of a single magnetometer measurement and the gradient along the X-direction.

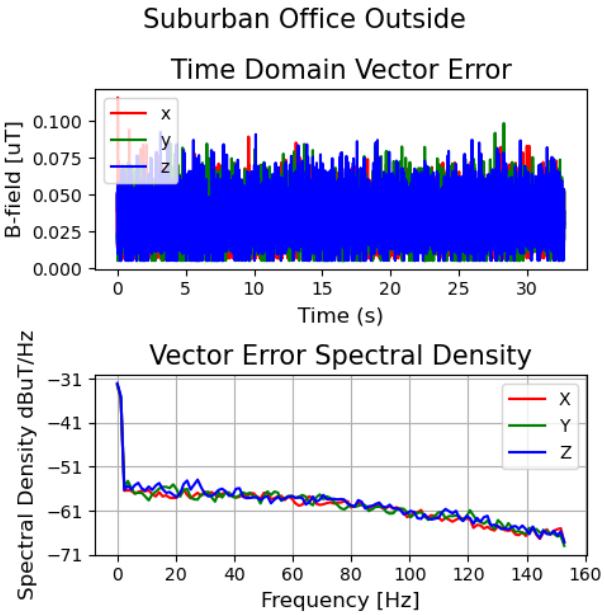

Figure C-16: Location: Suburban office outdoors. Magnitude of the gradient noise along three orthogonal directions.

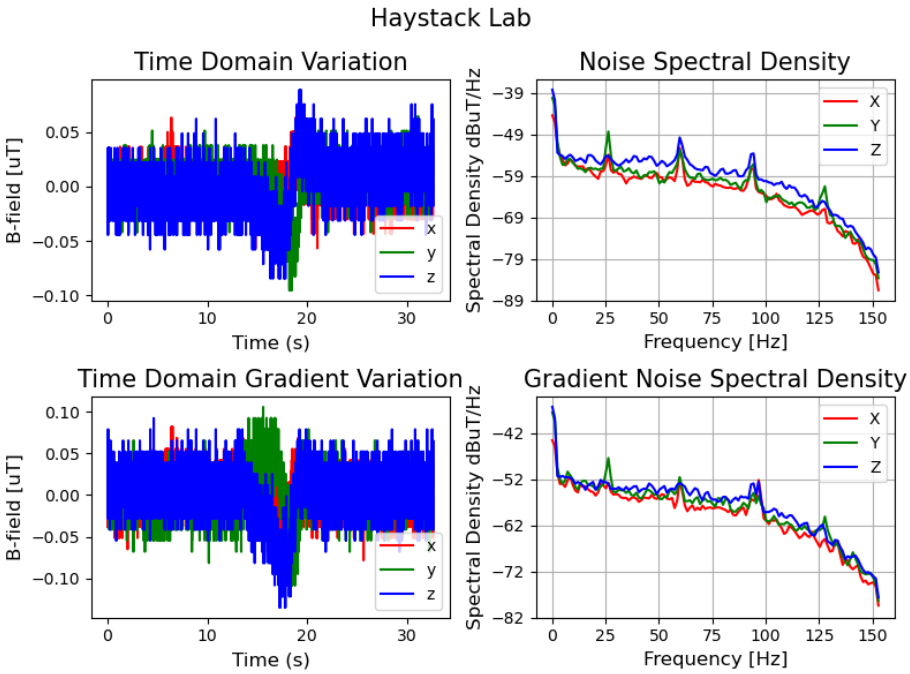

Figure C-17: Location: Rural lab. Time and frequency domain plotting of a single magnetometer measurement and the gradient along the X-direction.

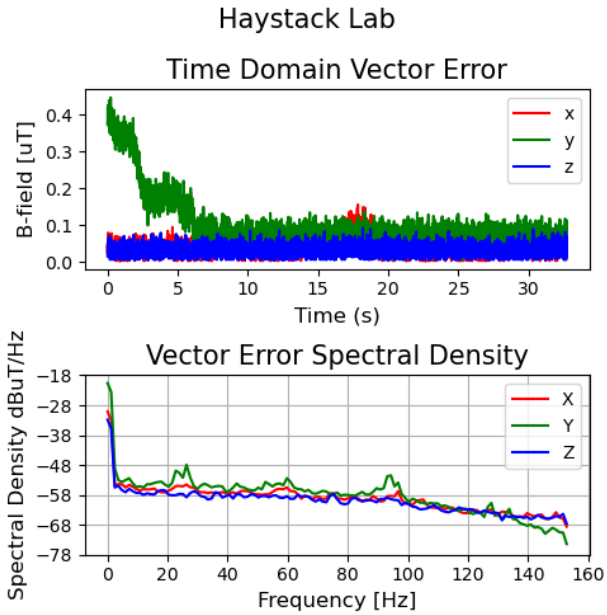

Figure C-18: Location: Rural lab. Magnitude of the gradient noise along three orthogonal directions.

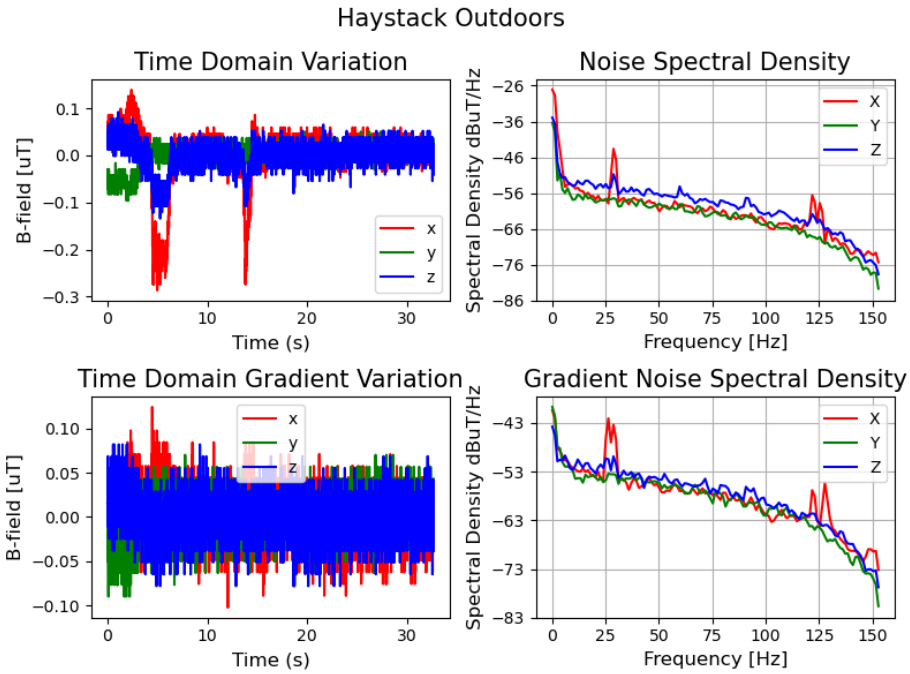

Figure C-19: Location: Rural lab outdoors. Time and frequency domain plotting of a single magnetometer measurement and the gradient along the X-direction.

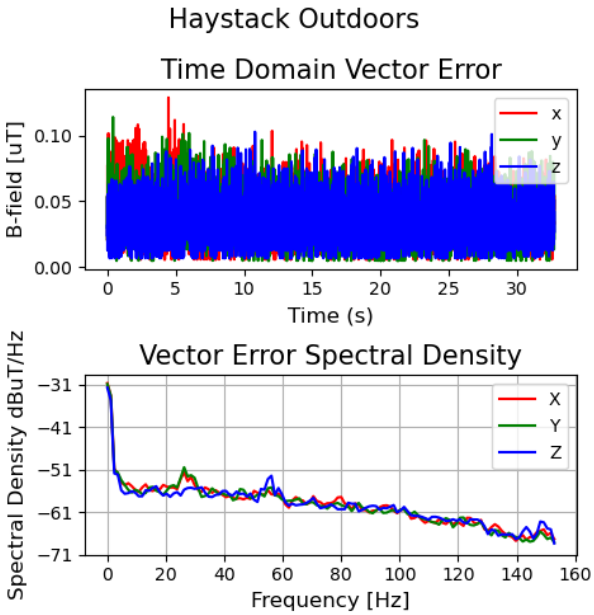

Figure C-20: Location: Rural lab outdoors. Magnitude of the gradient noise along three orthogonal directions.

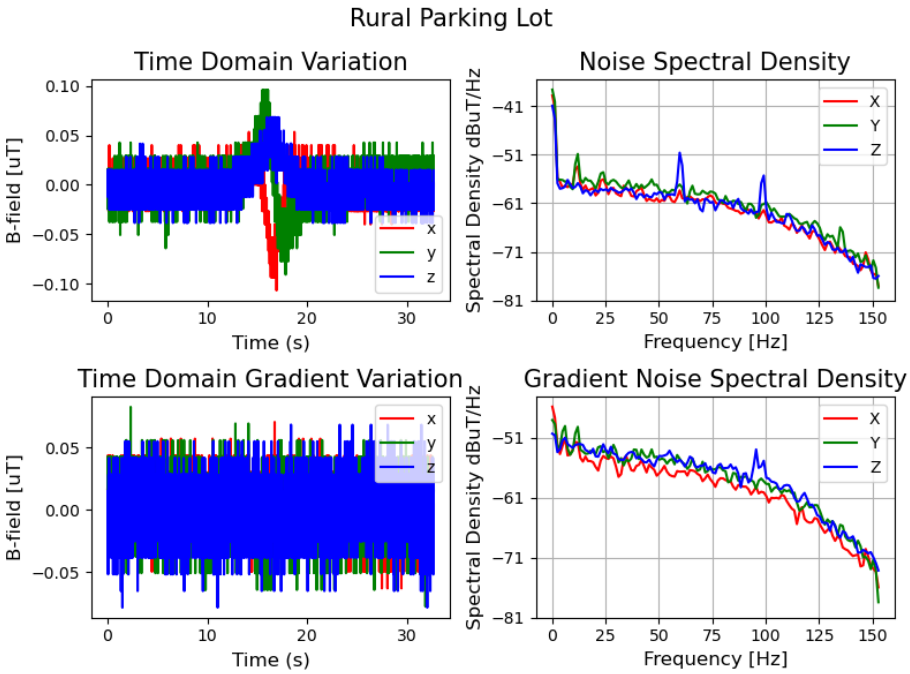

Figure C-21: Location: Rural parking lot. Time and frequency domain plotting of a single magnetometer measurement and the gradient along the X-direction. The deviation at about 15 seconds corresponds to a car driving by at about 10 meters distance.

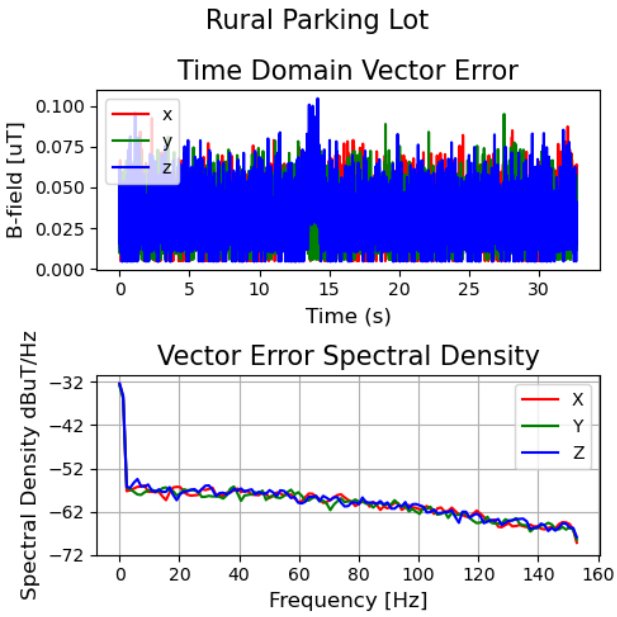

Figure C-22: Location: Rural parking lot. Magnitude of the gradient noise along three orthogonal directions.

C.2.1 Interpretation and Discussion

The dominant source of error in all measurements made in the Boston area are perturbations of a few seconds duration, primarily in the Z-axis. These are believed to be caused by the Boston subway system. These effects are larger in the Z-axis than the other axes since the current paths in the subway system circulate in the plane of the surface of the Earth. Additionally, the effects are strongest at the urban residence location, which is very close to the Davis Square subway stop.

All locations exhibit a noise spike at 60 Hz (often at 30 Hz or 120 Hz as well) consistent with power line noise. These effects are most notable in the more urban locations. However, the gradient often shows much less 60 Hz noise (e.g. Figure C-17) indicating that the noise must be generated relatively far away so is relatively constant in space when sampled with 0.5 meter spacing. This can be used for improved accuracy by keeping a reference magnetometer nearby as we did in Section 6.3. The measurements in residential locations show the most noise in the gradient, indicating the interference is created by something nearby, likely residential appliances.

The best locations we have measured include both indoors and outdoors of the suburban office and the rural parking lot. Locations like this should be relatively easy to access with CubeSat hardware so should be considered for more accurate measurements on future missions. The single most important takeaway is to avoid measurements within a few kilometers the subway system.

This page is intentionally left blank.

Appendix D

RM3100 EMI Considerations

Early in ASP development, the PNI RM3100 magnetometer [62] was selected for its sensitivity, ease of interface and low power. The PNI RM3100 magnetometer drives a LR oscillator circuit with input and output waveforms at about 180 kHz. These waveforms occur across an inductor of inductance about 500 uH, and therefore can couple 180 kHz varying magnetic fields into the measurements by the vector sensor. These interfering signals would be in the primary measurement band of the vector sensor and would not be locked to a coherent reference for easy filtering. Therefore, further investigation of the magnetic interference produced by these devices was undertaken. The EMI measurements clearly show the high interference from the magnetometer (see Section D.5), and this ultimately motivated the selection of a different magnetometer for use on AERO-VISTA.

D.1 EMI Characterisation Equipment

- RF Shielded room
- Keysight FieldFox N9917A
- Low Noise Amplifier: Mini-Circuit ZX60-73-S+
- Loop mode antenna: Beehive 100C Large Loop Probe
- PNI RM3100 magnetometer on evaluation board
- Teensy3.2 microcontroller [83] programmed as serial interface with the RM3100

- Laptop PC to serve as USB power source for the microcontroller and magnetometer

D.2 RM3100 State and Interface

The RM3100 was connected over SPI to a Teensy3.2 microcontroller. Both the microcontroller and RM3100 evaluation board were socketed into a standard 0.1" pitch prototyping breadboard. 22 AWG solid core wires were cut to length and used to make power and signal connections between the magnetometer and the microcontroller. The ground and power wires from the microcontroller to the magnetometer were routed together to minimize power supply magnetic interference but were not a twisted pair. The microcontroller was powered over an approximately 3' long micro USB cable by a PC laptop which was operating on battery in airplane mode. The microcontroller continuously read the magnetometer measurement SPI registers, but these measurements were not routed to the host computer to minimize the potential magnetic interference by the laptop.

D.3 RF Measurement Environment

The measurement was conducted in a RF-shielded room on a wooden table at least 6" away from the screen room walls. There were other unknown experiments and equipment in the room running and the nearby antenna was presumed to be occasionally transmitting. Additionally, power was provided by a consumer laptop located a few feet away from the measurement location. These factors conspire to create poor conditions for high precision EMI measurements, but at the frequencies observed, the data clearly indicate a binary difference between the magnetometer operating and the magnetometer not operating regardless of the state of other equipment in the area.

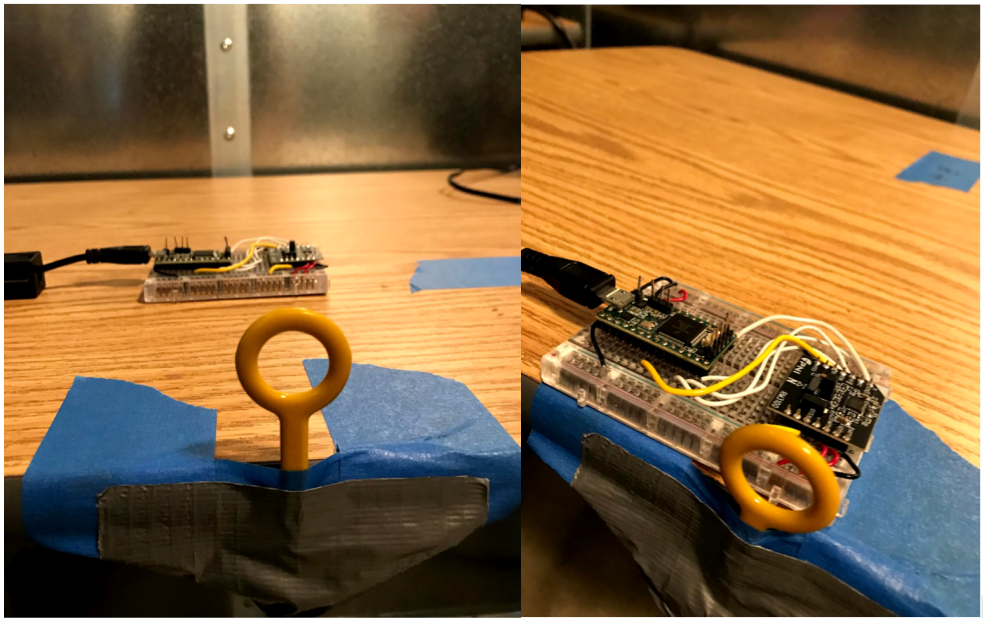

Figure D-1: Test setup with EMI antenna, microcontroller, and magnetometer shown.

D.4 Test Procedure Summary

1. Measure S12 of spectrum analyzer, cable, and LNA.
2. Affix 50 Ohm load to the end of the coax cable and make measurement to verify experimental setup.
3. Affix loop antenna to coax to and measure ambient EMI of the room with the magnetometer turned off.
4. Place the magnetometer 10 cm away from the center of the loop antenna and measure EMI in frequency of interest.
5. Repeat step 4 with the magnetometer in multiple orientations and operating at different measurement frequencies.
6. Repeat steps 4 and 5 with the magnetometer 3 cm away from the loop antenna.
7. Measure the EMI of the room with the magnetometer off to verify that the ambient EMI environment has not changed.

D.5 Measurement Results[1]

First, we start with a sample of the room and experimental setup without the magnetometer running to show the noise floor of the environment and measurement equipment. These results are shown in Figure D-2. Next we measure EMI with the antenna 10 cm away from the magnetometer and with the magnetometer running at a high sample rate. These results are shown in Figure D-3. In Figure D-4 we show a measurement taken with the antenna 3 cm from the magnetometer while running at the relatively slow speed of 10 Hz. To determine the effect of sample rate we made a similar measurement at 3 cm but with the magnetometer running at the fastest sample rate possible; these results are shown in Figure D-5. Finally, we present a zoomed in picture of the particularly broadband harmonic at about 850 kHz in Figure D-6.

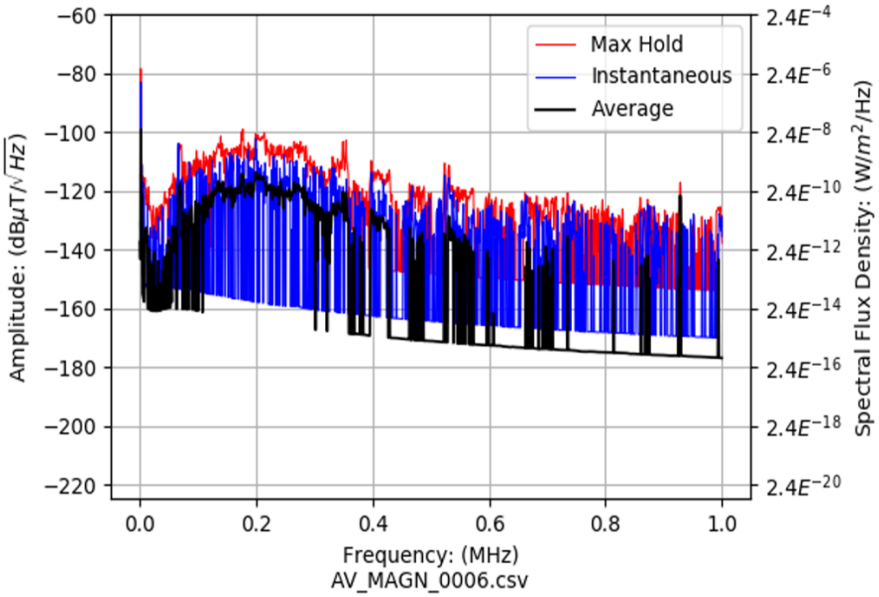

Figure D-2: EMI measurement noise floor.

[1]The author thanks Tobias Gedenk for assisting with EMI measurement and for generating the plots presented in this section.

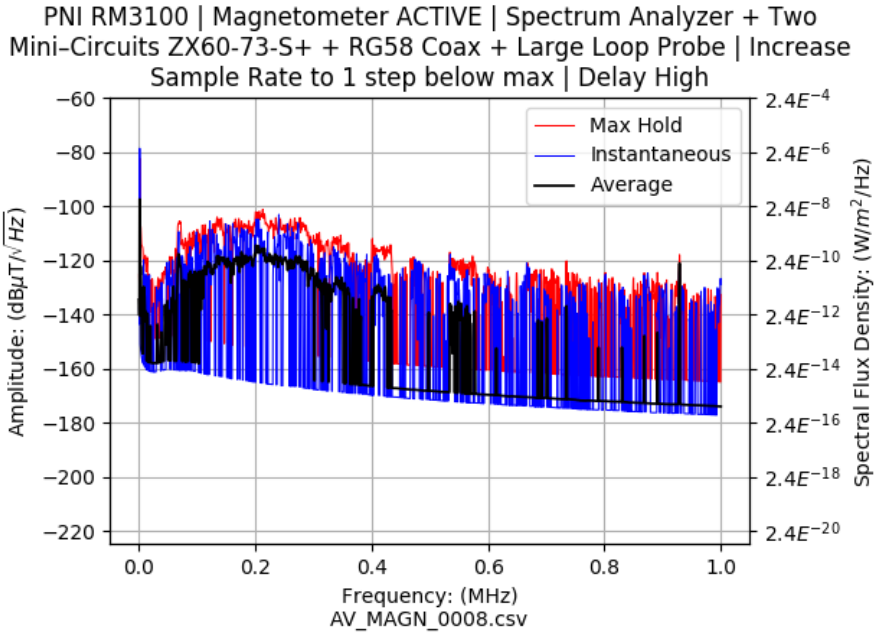

Figure D-3: RM3100 EMI measurement at 10 cm distance with magnetometer running at high sample rate.

D.6 Test Conclusion

The measured EMI of the RM3100 exhibits a sharp spike at about 180 kHz with many harmonics. Each axis of the magnetometer contributes a slightly different frequency to the EMI that depends on the magnetic flux along that axis. Therefore, this EMI cannot be filtered from the measurement in the same manner as the power supply switching frequency. The exact mapping of flux energy captured by the small loop probe to the sensitivity impact on the entire vector sensor antenna relies on near-field propagation effects and is difficult to determine, but as a very rough (and likely conservative) approximation, we can say that all of the flux and only the flux picked up by the small loop probe would also be picked up by one of the vector sensor elements (in reality much more flux would likely be captured by the large loop antenna). In this case, emissions above roughly $4 \times 10^{-16}\,\mathrm{W/m^2/Hz}$ would begin to effect sensitivity requirements. Shielding around the ASP module would help, but even in this conservative analysis, we would require more than 45 dB of shielding. The EMI level observed in this testing is larger than the EMI seen with similar

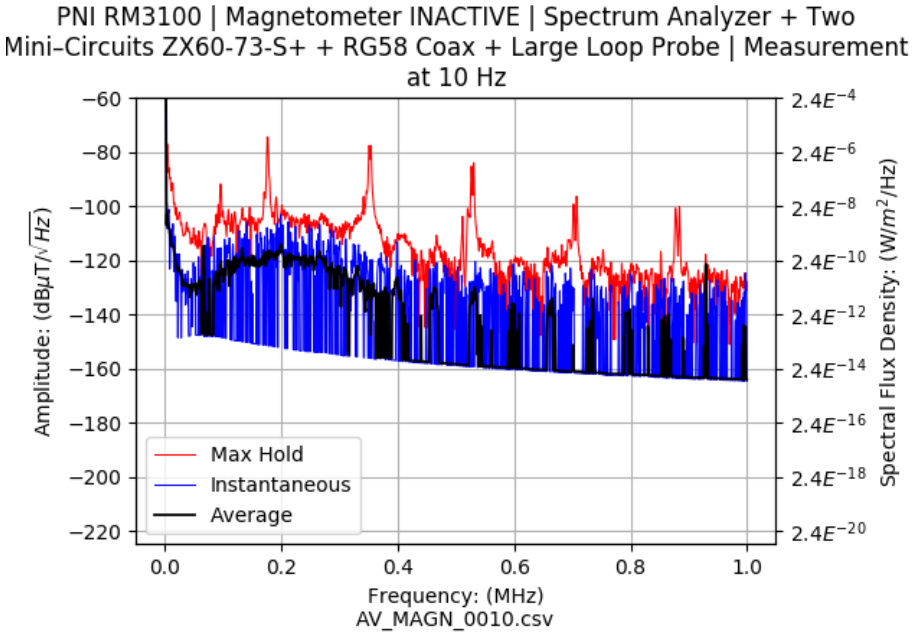

Figure D-4: RM3100 EMI measurement at 3 cm distance with magnetometer running at low sample rate.

measurements on the spacecraft bus and therefore would be a dominant interferer if used. Accordingly, the RM3100 has been replaced in the ASP design by the HMC1053 magnetoresisitive magnetometer, as this device operates on a different principal that is not expected to produce interference.

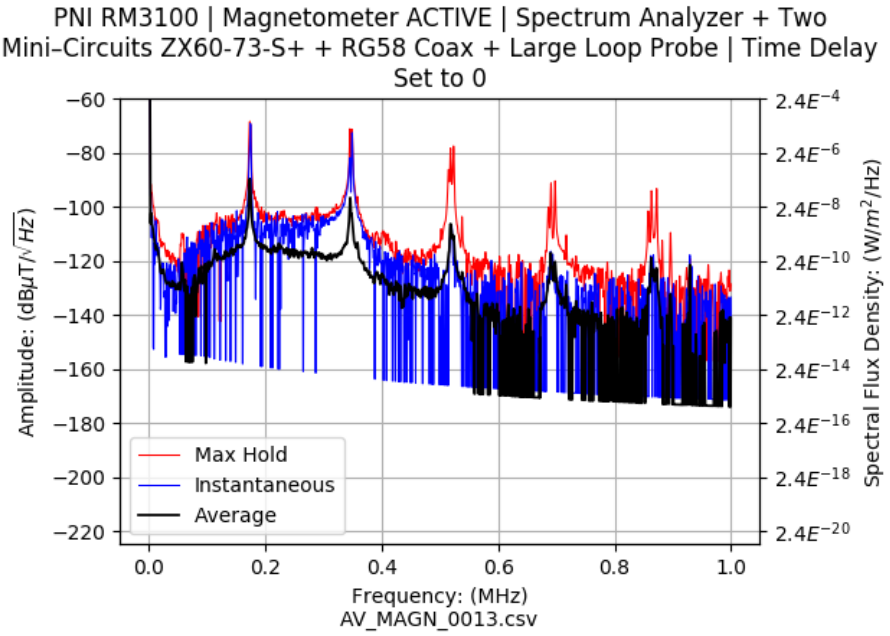

Figure D-5: RM3100 EMI measurement at 3 cm at fast sample rate.

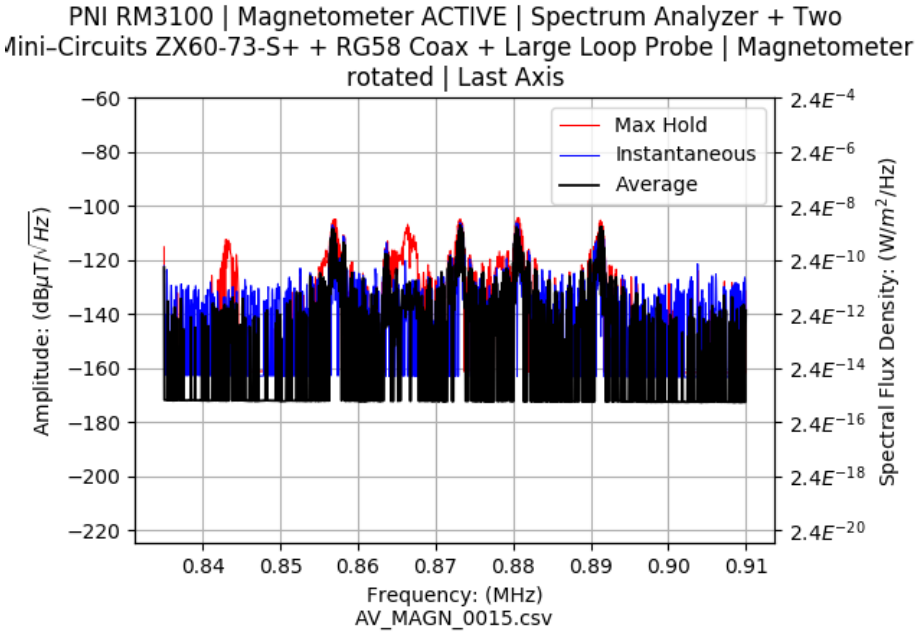

Figure D-6: RM3100 EMI Measurement at 3 cm at fast sample rate, zoomed in to show multiple peaks around 870 kHz.

This page is intentionally left blank.

Appendix E

Estimating Spectral Noise Dependence from Datasheets

In analog low-noise design, it is critical to find the dominant noise source and focus on minimizing that noise contribution first. Additionally, the dominant contribution to total noise may vary with frequency. Therefore, it is important to understand the relative contribution of each noise source over the entire frequency range of interest. Some datasheets provide this data directly in the form of a plot of noise amplitude (or power) over frequency. Such as provided for the THS4031 op-amp [85].

Other datasheets may only supply parameters that serve as a piece-wise linear fit to the data provided in the spectrum measurement. In this method, the THS4031 might be described as $3\,\mathrm{nV}/\sqrt{\mathrm{Hz}}$ at 10 kHz, with a 1 kHz flicker frequency corner. The flicker frequency corner describes the point at which the noise spectrum begins to be flat with frequency, rather than decreasing as $1/\sqrt{f}$. With this description, we could calculate an estimate for the noise density at 10 Hz of $30\,\mathrm{nV}/\sqrt{\mathrm{Hz}}$, and get within at least a factor of a few of the actual value seen in the spectrum plot.

Finally, some datasheets may provide the high frequency spectral noise density together with a value for the integrated noise from 0.1 Hz to 10 Hz, such as is done for the AD7771 ADC [77]. This datasheet reports a spectral noise density of $173.5\,\mathrm{nV}/\sqrt{\mathrm{Hz}}$ at 1 kHz, and a "voltage noise" of 6.8 uVrms.[1] This voltage noise in the 0.1 to 10 Hz

[1]The datasheet cues this parameter with the name "$e_{n_{p-p}}$" seemingly indicating that this value is

band is useful if this is the same as our measurement band, but if we are more interested in the noise at frequencies like 50 or 100 Hz, neither datasheet spot parameter is of much use. Fortunately, if we assume that the noise spectrum is piece-wise (logarithmically) linear with a single power-law change at a corner frequency of interest, we can convert from one representation to another and estimate the power spectrum just from the datasheet parameters provided. While this estimate may not be perfect, it does turn the provided datasheet parameters into a metric more suitable to our application with minimal assumptions.

E.1 Calculating Noise from a Frequency Spectrum

The integrated noise can be calculated from a spectral density representation using Eq. (E.1) [86].

$$V_n = \sqrt{\int_{f_{low}}^{f_{high}} (S(f)^2 df)} \tag{E.1}$$

If we have multiple frequency noise density measurements, we can estimate the integrated noise density by assuming a distribution shape between the two measurement points. One mathematically simple option is to assume that the square of the spectral amplitude (proportional to spectral power density) varies linearly with frequency. Then the total noise contributed in the frequency range is given in Eq. (E.2). This simple formula can be implemented in spreadsheet programs, and we use this method to piece-wise integrate the total noise.

$$V_n = \sqrt{\frac{S(f_{low})^2 + S(f_{high})^2}{2}(f_{high} - f_{low})} \tag{E.2}$$

the peak-to-peak voltage noise and not the rms voltage noise as indicated by the units in the same column. We have assumed that the value provided is an rms value as the noise would be scaled *down* by about a factor of 6 if the noise provided was actually a peak to peak value [86]. This is the conservative assumption.

E.2 Estimating Spectrum from Integrated Noise

Now we consider the opposite question, we want to estimate spectral noise density from a few spot datasheet noise parameters. For this analysis we will assume we are provided with a high frequency noise density and an integrated noise density from 0.1 Hz to 10 Hz as is commonly reported in datasheets, though similar analysis could be used for other available parameters.

From Eq. (E.2), it is apparent that the formula for integrated noise will have different forms depending on if the corner frequency is above or below 10 Hz. To perform a piecewise fit, We define α to be a constant equal to the spectral noise density for the flicker frequency noise at intercept with f=1 Hz.

Fc>10Hz If the corner frequency is above the integration range we can write:

$$V_{rms} = \sqrt{\int_{0.1}^{10} (\alpha^2 * f^{-1} df)} = \alpha \sqrt{ln(\frac{10}{0.1})} \approx 2.15 * \alpha. \tag{E.3}$$

When provided a Vrms from 0.1 to 10 Hz, we can solve for α and write a frequency dependent estimate for the frequency noise density:

$$S(f) = \alpha * f^{-1/2} \tag{E.4}$$

$$\alpha * f_c^{-1/2} = S_{hf} \tag{E.5}$$

$$f_c = \big(\frac{\alpha}{S_{hf}}\big)^2. \tag{E.6}$$

Here f_c is the flicker noise corner frequency. S_{hf} is the high frequency (frequency independent) spectral noise density.

Fc<10 Hz If the corner frequency is below 10 Hz, we write the integral over frequency piecewise as:

$$V_{rms} = \sqrt{\int_{0.1}^{fc} (\alpha^2 * f^{-1} df) + \int_{f_c}^{10} S_{hf}^2 df} = \sqrt{\alpha^2 * ln(\frac{f_c}{0.1}) + (10 - f_c) * S_{hf}^2}. \quad \text{(E.7)}$$

We have another equation in the definition of the corner frequency intersection point:

$$\alpha = S_{hf} * \sqrt{f_c} \quad \text{(E.8)}$$

$$V_{rms} = \sqrt{S_{hf}^2 * f_c * ln(\frac{f_c}{0.1}) + (10 - f_c) * S_{hf}^2}. \quad \text{(E.9)}$$

Now we have an equation relating only Vrms to only fc, which then can be used to find α and then the total estimated spectral noise density.

E.3 Example: AD7771 ADC

The AD7771 ADC used in Chapter 7 has a high frequency noise density of $174\,\text{nV}/\sqrt{\text{Hz}}$ at 1 kHz and an integrated voltage noise of 6.8 uVrms from 0.1 to 10 Hz [77]. We will start by assuming that fc>10 Hz since this is a relatively large low frequency integrated noise. We will revisit this assumption at the end and correct if necessary. First we find α from Eq. (E.5):

$$\alpha = \frac{6.8\,\mu\text{V}}{2.15} = 3.16\,\mu\text{V}. \quad \text{(E.10)}$$

Then we can find fc from Eq. (E.6):

$$f_c = \left(\frac{3.16\,\mu\text{V}}{0.174\,\text{nV}/\sqrt{\text{Hz}}}\right)^2 = 18.2\,\text{Hz}. \quad \text{(E.11)}$$

We can confirm that the approximated corner frequency is above 10 Hz as we had

previously assumed. Finally, we can write the approximated noise spectrum:

$$S(f) \approx \begin{cases} 3.16\,\mu\text{V} * f^{-1/2} & f \leq 18.2\,\text{Hz} \\ 0.174\,\mu\text{V} & f \geq 18.2\,\text{Hz} \end{cases}. \tag{E.12}$$

This analysis is used in Chapter 7 to estimate the spectral distribution of the noise contribution of the AD7771 to the analog magnetic measurement.

This page is intentionally left blank.

Bibliography

[1] R. Hadley, "Magnetic Fundamentals, Hysteresis." [Online]. Available: https://www.coolmagnetman.com/magfund07.htm

[2] "Concept of Magnetization or Saturation Curve: B-H Curve," Dec. 2016, electrical Baba. [Online]. Available: https://electricalbaba.com/concept-of-magnetization-or-saturation-curve-b-h-curve/

[3] "ISIS CubeSat solar panels." [Online]. Available: https://www.isispace.nl/product/isis-cubesat-solar-panels/

[4] M. Knapp, "AERO-VISTA L0/L1 Requirements," Aug. 2019.

[5] "1, 2 and 3 Axis Magnetic Sensors HMC1051/HMC1052/HMC1053." [Online]. Available: https://media.digikey.com/pdf/Data%20Sheets/Honeywell%20PDFs/HMC1051,52,53.pdf

[6] J. Moreland, "Units for Magnetic Properties." [Online]. Available: https://www.nist.gov/system/files/documents/pml/electromagnetics/magnetics/magnetic_units.pdf

[7] "CubeSat Solar panels DHV-CS-10 - CubeSatShop.com." [Online]. Available: https://www.cubesatshop.com/product/cubesat-solar-panels-dhv/

[8] "World Magnetic Model - Maps of Magnetic Elements." [Online]. Available: https://www.ngdc.noaa.gov/geomag/WMM/image.shtml

[9] "World Magnetic Model - Model Limitations." [Online]. Available: https://www.ngdc.noaa.gov/geomag/WMM/limit.shtml

[10] P. Alken, E. Thébault, C. D. Beggan, H. Amit, J. Aubert, J. Baerenzung, T. N. Bondar, W. J. Brown, S. Califf, A. Chambodut, A. Chulliat, G. A. Cox, C. C. Finlay, A. Fournier, N. Gillet, A. Grayver, M. D. Hammer, M. Holschneider, L. Huder, G. Hulot, T. Jager, C. Kloss, M. Korte, W. Kuang, A. Kuvshinov, B. Langlais, J.-M. Léger, V. Lesur, P. W. Livermore, F. J. Lowes, S. Macmillan, W. Magnes, M. Mandea, S. Marsal, J. Matzka, M. C. Metman, T. Minami, A. Morschhauser, J. E. Mound, M. Nair, S. Nakano, N. Olsen, F. J. Pavón-Carrasco, V. G. Petrov, G. Ropp, M. Rother, T. J. Sabaka, S. Sanchez, D. Saturnino, N. R. Schnepf, X. Shen, C. Stolle, A. Tangborn, L. Tøffner-Clausen, H. Toh, J. M. Torta, J. Varner, F. Vervelidou,

P. Vigneron, I. Wardinski, J. Wicht, A. Woods, Y. Yang, Z. Zeren, and B. Zhou, "International Geomagnetic Reference Field: the thirteenth generation," *Earth, Planets and Space*, vol. 73, no. 1, p. 49, Dec. 2021. [Online]. Available: https://earth-planets-space.springeropen.com/articles/10.1186/s40623-020-01288-x

[11] P. Pereira, M. Garcia, M. Schroeder, H. Caldelas, C. Lindsay, A. Choi, K. Pfrang, A. Gagnon, A. Meredith, P. McKeen, J. Clark, T. Murphy, S. Baber, S. Khan, A. Miller, G. Velez, M. Campbell, J. Coray, J. Koldada, T. Tran, S. Austin, A. Louthain, T. Wells, M. Kabir, E. Sit, C. Haughwout, and K. Cahoy, "BeaverCube: Coastal Imaging with VIS/LWIR CubeSats," *Small Satellite Conference*, Aug. 2020. [Online]. Available: https://digitalcommons.usu.edu/smallsat/2020/all2020/126

[12] Y. Liu, K.-P. Liu, Y.-L. Li, Q. Pan, and J. Zhang, "A ground testing system for magnetic-only ADCS of nano-satellites," in *2016 IEEE Chinese Guidance, Navigation and Control Conference (CGNCC)*, Aug. 2016, pp. 1644–1647.

[13] B. J. Anderson, M. H. Acuna, H. Korth, J. A. Slavin, H. Uno, C. L. Johnson, M. E. Purucker, S. C. Solomon, J. M. Raines, T. H. Zurbuchen, G. Gloeckler, and R. L. McNutt, "The Magnetic Field of Mercury," *Space Science Reviews*, vol. 152, no. 1, pp. 307–339, May 2010. [Online]. Available: https://doi.org/10.1007/s11214-009-9544-3

[14] C. T. Russell, R. C. Elphic, and J. A. Slavin, "Initial Pioneer Venus Magnetic Field Results: Dayside Observations," *Science*, Feb. 1979, publisher: American Association for the Advancement of Science. [Online]. Available: https://www.science.org/doi/abs/10.1126/science.203.4382.745

[15] R. A. Langel and W. J. Hinze, *The Magnetic Field of the Earth's Lithosphere: The Satellite Perspective*. Cambridge University Press, Jul. 1998, google-Books-ID: S3SCwnO707oC.

[16] M. H. Acuña, J. E. P. Connerney, P. Wasilewski, R. P. Lin, K. A. Anderson, C. W. Carlson, J. McFadden, D. W. Curtis, D. Mitchell, H. Reme, C. Mazelle, J. A. Sauvaud, C. d'Uston, A. Cros, J. L. Medale, S. J. Bauer, P. Cloutier, M. Mayhew, D. Winterhalter, and N. F. Ness, "Magnetic Field and Plasma Observations at Mars: Initial Results of the Mars Global Surveyor Mission," *Science*, vol. 279, no. 5357, pp. 1676–1680, 1998, publisher: American Association for the Advancement of Science. [Online]. Available: https://www.jstor.org/stable/2894341

[17] J. E. P. Connerney, S. Kotsiaros, R. J. Oliversen, J. R. Espley, J. L. Joergensen, P. S. Joergensen, J. M. G. Merayo, M. Herceg, J. Bloxham, K. M. Moore, S. J. Bolton, and S. M. Levin, "A New Model of Jupiter's Magnetic Field From Juno's First Nine Orbits," *Geophysical Research Letters*, vol. 45, no. 6, pp. 2590–2596, 2018. [Online]. Available: https://onlinelibrary.wiley.com/doi/abs/10.1002/2018GL077312

[18] E. J. Smith, J. L. Davis, D. E. Jones, J. P. J. Coleman, D. S. Colburn, P. Dyal, and C. P. Sonett, "Saturn's Magnetic Field and Magnetosphere," *Science*, Jan. 1980, publisher: American Association for the Advancement of Science. [Online]. Available: https://www.science.org/doi/abs/10.1126/science.207.4429.407

[19] J. E. P. Connerney, M. H. Acuña, and N. F. Ness, "The magnetic field of Uranus," *Journal of Geophysical Research: Space Physics*, vol. 92, no. A13, pp. 15 329–15 336, 1987. [Online]. Available: https://onlinelibrary.wiley.com/doi/abs/10.1029/JA092iA13p15329

[20] J. E. P. Connerney, M. H. Acuna, and N. F. Ness, "The magnetic field of Neptune," *Journal of Geophysical Research: Space Physics*, vol. 96, no. S01, pp. 19 023–19 042, 1991. [Online]. Available: https://onlinelibrary.wiley.com/doi/abs/10.1029/91JA01165

[21] C. P. Sonett, D. S. Colburn, and R. G. Currie, "The intrinsic magnetic field of the Moon," *Journal of Geophysical Research (1896-1977)*, vol. 72, no. 21, pp. 5503–5507, 1967. [Online]. Available: https://onlinelibrary.wiley.com/doi/abs/10.1029/JZ072i021p05503

[22] H. U. Auster, I. Richter, K. H. Glassmeier, G. Berghofer, C. M. Carr, and U. Motschmann, "Magnetic field investigations during ROSETTA's 2867 Šteins flyby," *Planetary and Space Science*, vol. 58, no. 9, pp. 1124–1128, Jul. 2010. [Online]. Available: https://www.sciencedirect.com/science/article/pii/S0032063310000188

[23] I. Richter, H. U. Auster, K. H. Glassmeier, C. Koenders, C. M. Carr, U. Motschmann, J. Müller, and S. McKenna-Lawlor, "Magnetic field measurements during the ROSETTA flyby at asteroid (21)Lutetia," *Planetary and Space Science*, vol. 66, no. 1, pp. 155–164, Jun. 2012. [Online]. Available: https://www.sciencedirect.com/science/article/pii/S0032063311002698

[24] X. Zhao and J. T. Hoeksema, "Prediction of the interplanetary magnetic field strength," *Journal of Geophysical Research: Space Physics*, vol. 100, no. A1, pp. 19–33, 1995. [Online]. Available: https://onlinelibrary.wiley.com/doi/abs/10.1029/94JA02266

[25] C. Nicollier and R.-M. Bonnet, Eds., *Our Space Environment, Opportunities, Stakes and Dangers*, 1st ed. Lausanne (Suisse) Boca Raton (Fla.): EPFL Press, Dec. 2015.

[26] V. D. Albertson and J. A. Van Baelen, "Electric and Magnetic Fields at the Earth's Surface Due to Auroral Currents," *IEEE Transactions on Power Apparatus and Systems*, vol. PAS-89, no. 4, pp. 578–584, Apr. 1970, conference Name: IEEE Transactions on Power Apparatus and Systems.

[27] D. A. Gurnett, S. D. Shawhan, and R. R. Shaw, "Auroral hiss, Z mode radiation, and auroral kilometric radiation in the polar magnetosphere: DE 1

observations," *Journal of Geophysical Research: Space Physics*, vol. 88, no. A1, pp. 329–340, 1983. [Online]. Available: https://onlinelibrary.wiley.com/doi/abs/10.1029/JA088iA01p00329

[28] W. S. Kurth, M. M. Baumback, and D. A. Gurnett, "Direction-finding measurements of auroral kilometric radiation," *Journal of Geophysical Research (1896-1977)*, vol. 80, no. 19, pp. 2764–2770, 1975. [Online]. Available: https://onlinelibrary.wiley.com/doi/abs/10.1029/JA080i019p02764

[29] P. J. Erickson, C. Geoffrey, M. Hecht, M. Knapp, F. Lind, R. Volz, J. LaBelle, F. Robey, K. Cahoy, B. Malphrus, J. Vierinen, and A. Weatherwax, "AERO: Auroral Emissions Radio Observer," MIT Lincoln Laboratory Lexington United States, Tech. Rep., Aug. 2018, section: Technical Reports. [Online]. Available: https://apps.dtic.mil/sti/citations/AD1088037

[30] M. Knapp, F. Robey, R. Volz, F. Lind, A. Fenn, A. Morris, M. Silver, S. Klein, and S. Seager, "Vector antenna and maximum likelihood imaging for radio astronomy," in *2016 IEEE Aerospace Conference*, Mar. 2016, pp. 1–17.

[31] F. Lind, P. Erickson, M. Hecht, M. Knapp, G. Crew, R. Volz, J. Swoboda, F. Robey, M. Silver, A. Fenn, B. Malphrus, and K. Cahoy, "AERO & VISTA: Demonstrating HF Radio Interferometry with Vector Sensors," *Small Satellite Conference*, Aug. 2019. [Online]. Available: https://digitalcommons.usu.edu/smallsat/2019/all2019/96

[32] N. Belsten, C. Payne, P. Serra, K. Cahoy, F. Lind, M. Knapp, P. Erickson, and F. Robey, "Design and Verification of a Clock System for Orbital Radio Interferometry," *Small Satellite Conference*, Aug. 2020. [Online]. Available: https://digitalcommons.usu.edu/smallsat/2020/all2020/166

[33] A. R. Thompson, J. M. Moran, and G. W. Swenson, "Introductory Theory of Interferometry and Synthesis Imaging," in *Interferometry and Synthesis in Radio Astronomy*, ser. Astronomy and Astrophysics Library, A. R. Thompson, J. M. Moran, and G. W. Swenson Jr., Eds. Cham: Springer International Publishing, 2017, pp. 59–88. [Online]. Available: https://doi.org/10.1007/978-3-319-44431-4_2

[34] M. O. Archer, T. S. Horbury, P. Brown, J. P. Eastwood, T. M. Oddy, B. J. Whiteside, and J. G. Sample, "The MAGIC of CINEMA: first in-flight science results from a miniaturised anisotropic magnetoresistive magnetometer," *Annales Geophysicae*, vol. 33, no. 6, pp. 725–735, Jun. 2015. [Online]. Available: https://angeo.copernicus.org/articles/33/725/2015/

[35] J. D. Jackson, *Classical Electrodynamics Third Edition*, 3rd ed. New York: Wiley, Aug. 1998.

[36] H. D. Young, R. A. Freedman, T. Sandin, and A. L. Ford, *University Physics With Modern Physics*, 12th ed. San Francisco: Benjamin-Cummings Pub Co, Mar. 2007.

[37] D. J. Griffiths, *Introduction to Electrodynamics*, 4th ed. Cambridge, United Kingdom ; New York, NY: Cambridge University Press, Jul. 2017.

[38] W. M. Haynes, Ed., *CRC Handbook of Chemistry and Physics, 92nd Edition*, 92nd ed. Boca Raton, Fla.: CRC Press, Jun. 2011.

[39] J. R. Wertz, D. F. Everett, and J. J. Puschell, Eds., *Space Mission Engineering: The New SMAD*, first edition ed. Hawthorne, CA: Microcosm Press, Jul. 2011.

[40] "FAQ 3: Magnetic Effects of Stainless Steels." [Online]. Available: https://www.assda.asn.au/technical-info/technical-faqs/magnetic-effects-of-stainless-steels

[41] "Are 304 and 316 Stainless Steels Magnetic?" [Online]. Available: https://www.mtm-inc.com/how-nonmagnetic-are-304-and-316-stainless-steels.html

[42] "Magnetic Properties of Stainless Steels." [Online]. Available: https://www.carpentertechnology.com/blog/magnetic-properties-of-stainless-steels

[43] J. M. D. Coey, *Magnetism and Magnetic Materials*. Cambridge: Cambridge University Press, 2010. [Online]. Available: https://www.cambridge.org/core/books/magnetism-and-magnetic-materials/AD3557E2D4538CAA8488A8C1057313BC

[44] C. Xu, X. Liu, F. Xue, Y. Li, W. Qian, and M. Yu, "Characterization of magnetic properties in a 316 stainless steel after deformation and irradiation," *Fusion Engineering and Design*, vol. 133, pp. 125–129, Aug. 2018. [Online]. Available: https://www.sciencedirect.com/science/article/pii/S0920379618305131

[45] R. Moskowitz and R. Lynch, "Magnetostatic Measurement of Spacecraft Magnetic Dipole Moment," *IEEE Transactions on Aerospace*, vol. 2, no. 2, pp. 412–419, Apr. 1964, conference Name: IEEE Transactions on Aerospace.

[46] K. Mehlem, "Multiple magnetic dipole modeling and field prediction of satellites," *IEEE Transactions on Magnetics*, vol. 14, no. 5, pp. 1064–1071, Sep. 1978, conference Name: IEEE Transactions on Magnetics.

[47] N. F. Ness, K. W. Behannon, R. P. Lepping, and K. H. Schatten, "Use of two magnetometers for magnetic field measurements on a spacecraft," *Journal of Geophysical Research (1896-1977)*, vol. 76, no. 16, pp. 3564–3573, 1971, _eprint: https://agupubs.onlinelibrary.wiley.com/doi/pdf/10.1029/JA076i016p03564. [Online]. Available: https://agupubs.onlinelibrary.wiley.com/doi/abs/10.1029/JA076i016p03564

[48] "EXA MT01 Compact Magnetorquer." [Online]. Available: https://www.cubesatshop.com/product/mt01-compact-magnetorquer/

[49] O. Baltag, G. Rosu, and M. C. Rau, "Magnetic field of parallel and twisted wire pairs," Jan. 2017, pp. 324–329.

[50] K. Mehlem and A. Wiegand, "Magnetostatic cleanliness of spacecraft," in *2010 Asia-Pacific International Symposium on Electromagnetic Compatibility*, Apr. 2010, pp. 936–944, iSSN: 2162-7673.

[51] P. S. Narvaez, "DC Magnetic Cleanliness Description for Spaceflight Programs," in *Handbook of Aerospace Electromagnetic Compatibility*, R. Perez, Ed. Hoboken, NJ, USA: John Wiley & Sons, Inc., Dec. 2018, pp. 621–672. [Online]. Available: https://onlinelibrary.wiley.com/doi/10.1002/9781119082880.ch12

[52] C. T. Russell, Ed., *The Cassini-Huygens Mission: Orbiter In Situ Investigations Volume 2*. Dordrecht: Springer Netherlands, 2004. [Online]. Available: http://link.springer.com/10.1007/978-1-4020-2774-1

[53] S. Weikert, K. Mehlem, and A. Wiegand, "Spacecraft magnetic cleanliness prediction and control," in *2012 ESA Workshop on Aerospace EMC*, May 2012, pp. 1–5.

[54] C. D. Nikolopoulos, A. T. Baklezos, and C. N. Capsalis, "On Achieving Spacecraft Level Magnetic Cleanliness With Proper Equipment Ordinance of DC and ELF Magnetic Sources," *IEEE Transactions on Electromagnetic Compatibility*, vol. 62, no. 6, pp. 2714–2724, Dec. 2020, conference Name: IEEE Transactions on Electromagnetic Compatibility.

[55] K. Mehlem, A. Wiegand, and S. Weickert, "New developments in magnetostatic cleanliness modeling," in *2012 ESA Workshop on Aerospace EMC*, May 2012, pp. 1–6.

[56] M. de Soria-Santacruz, M. Soriano, O. Quintero, F. Wong, S. Hart, M. Kokorowski, B. Bone, B. Solish, D. Trofimov, E. Bradford, C. Raymond, P. Narvaez, C. Keys, P. Lord, J. Ream, R. Oran, B. P. Weiss, C. Russell, K. Ascrizzi, and L. Elkins-Tanton, "An Approach to Magnetic Cleanliness for the Psyche Mission," in *2020 IEEE Aerospace Conference*, Mar. 2020, pp. 1–15, iSSN: 1095-323X.

[57] C. Smith, J. L'Heureux, N. Ness, M. Acuña, L. Burlaga, and J. Scheifele, "The ACE Magnetic Fields Experiment," *Space Science Reviews*, vol. 86, no. 1, pp. 613–632, Jul. 1998. [Online]. Available: https://doi.org/10.1023/A:1005092216668

[58] C. Pong, "On-Orbit Performance & Operation of the Attitude & Pointing Control Subsystems on ASTERIA," *Small Satellite Conference*, Aug. 2018. [Online]. Available: https://digitalcommons.usu.edu/smallsat/2018/all2018/361

[59] "About NASA's Explorer Missions." [Online]. Available: https://nssdc.gsfc.nasa.gov/multi/explorer.html

[60] "Cassini Mission: Estimated Launch Costs for NASA's Mission to Saturn." [Online]. Available: https://www.govinfo.gov/content/pkg/GAOREPORTS-NSIAD-95-141BR/html/GAOREPORTS-NSIAD-95-141BR.htm

[61] "HMC1053 Honeywell Aerospace | Sensors, Transducers | DigiKey." [Online]. Available: https://www.digikey.com/en/products/detail/honeywell-aerospace/HMC1053/603147

[62] "RM3100 Geomagnetic Sensor." [Online]. Available: https://www.pnicorp.com/rm3100/

[63] "Resolution vs Accuracy vs Sensitivity Cutting Through the Confusion," Dec. 1998. [Online]. Available: https://www.electronicdesign.com/home/article/21200276/resolution-vs-accuracy-vs-sensitivity-cutting-through-the-confusion

[64] "Measurements and Error Analysis." [Online]. Available: https://www.webassign.net/question_assets/unccolphysmechl1/measurements/manual.html

[65] A. Steve, "Noise in Electronics Engineering: Distribution, Noise RMS and Peak-to-Peak Value, and Power Spectral Density - Technical Articles." [Online]. Available: https://www.allaboutcircuits.com/technical-articles/noise-in-electronics-engineering-distribution-noise-rms-peak-to-peak-value-PSD/

[66] "Meda | Products." [Online]. Available: http://www.meda.com/index.php/products?name=FVM400

[67] P. Mahavarkar, J. John, V. Dhapre, V. Dongre, and S. Labde, "Tri-axial square Helmholtz coil system at the Alibag Magnetic Observatory: upgraded to a magnetic sensor calibration facility," *Geoscientific Instrumentation, Methods and Data Systems*, vol. 7, no. 2, pp. 143–149, Apr. 2018, publisher: Copernicus GmbH. [Online]. Available: https://gi.copernicus.org/articles/7/143/2018/

[68] M. Prinkey, D. Miller, P. Bauer, K. Cahoy, E. Wise, C. Pong, R. Kingsbury, A. Marinan, H. W. Lee, and E. Main, "CubeSat attitude control testbed design: Merritt 4-Coil per axis helmholtz cage and spherical air bearing," *AIAA Guidance, Navigation, and Control (GNC) Conference*, Jan. 2013.

[69] "Surface Fields 101." [Online]. Available: https://www.kjmagnetics.com/blog.asp?p=surface-fields-101

[70] "Wheatstone Bridge Circuit and Theory of Operation," Oct. 2013. [Online]. Available: https://www.electronics-tutorials.ws/blog/wheatstone-bridge.html

[71] "Magnetoresistive Sensors," Honeywell, Tech. Rep. 50272. [Online]. Available: https://sensing.honeywell.com/index.php?ci_id=50272

[72] P. Horowitz and H. Winfield, *The Art of Electronics*, 3rd ed. New York, NY: Cambridge University Press, Apr. 2015.

[73] "How and When the Chip Shortage Will End, in 4 Charts," Jun. 2021, section: Semiconductors. [Online]. Available: https://spectrum.ieee.org/chip-shortage

[74] "Buy a Raspberry Pi Zero." [Online]. Available: https://www.raspberrypi.com/products/raspberry-pi-zero/

[75] "LMP202x Zero-Drift, Low-Noise, EMI-Hardened Amplifiers," Sep. 2008. [Online]. Available: https://www.ti.com/lit/ds/symlink/lmp2022.pdf?ts=1641230803266&ref_url=https%253A%252F%252Fwww.ti.com%252Fproduct%252FLMP2022

[76] "Resistor Noise | Resistor Fundamentals | Resistor Guide." [Online]. Available: https://eepower.com/resistor-guide/resistor-fundamentals/resistor-noise/

[77] "AD7771 Datasheet and Product Info | Analog Devices." [Online]. Available: https://www.analog.com/en/products/ad7771.html

[78] C. Payne, "Auroral Arc Detection using a COTS Spectral Photometer for the Auroral Emission Radio Explorer (AERO) CubeSat Mission," Ph.D. dissertation, MASSACHUSETTS INSTITUTE OF TECHNOLOGY, May 2020.

[79] "Buy a Raspberry Pi Camera Module 2." [Online]. Available: https://www.raspberrypi.com/products/camera-module-v2/

[80] J. Adams, "Introducing Raspberry Pi HATs," Jul. 2014. [Online]. Available: https://www.raspberrypi.com/news/introducing-raspberry-pi-hats/

[81] T. Bulfinch, *Bulfinch's Mythology*, Jan. 2004. [Online]. Available: https://www.gutenberg.org/ebooks/4928

[82] S. Withrow, J. Wayne, L. Young, H. Cummings, J. Balaram, and T. Tzanetos, "An Advanced Mars Helicopter Design | ASCEND 2020," Nov. 2020, archive Location: world. [Online]. Available: https://arc.aiaa.org/doi/abs/10.2514/6.2020-4028

[83] "Teensy® 3.2." [Online]. Available: https://www.pjrc.com/store/teensy32.html

[84] N. Belsten and D. K. Cahoy, "We are the MIT Space Telecommunications Astronomy and Radiation Laboratory (STAR Lab). We achieve new scientific results from sensors on distributed space-based platforms. We innovate and use new commercial components to address technological challenges for future science missions, reducing cost and risk." p. 1.

[85] "THS4031 data sheet, product information and support | TI.com." [Online]. Available: https://www.ti.com/product/THS4031

[86] "Spectral Noise Density to RMS Noise | Analog Devices." [Online]. Available: https://www.analog.com/en/education/education-library/videos/756529027001.html